Clarkson University

MODELING OF AN AUTOMOTIVE EXHAUST THERMOELECTRIC GENERATOR

a thesis

by

Madhav A Karri

department of Mechanical and Aeronautical Engineering

June 2005

The undersigned have examined the thesis entitled

Modeling Of An Automotive Exhaust Thermoelectric Generator

presented by Madhav A Karri, a candidate for the degree of Master of Science, and hereby certify that it is worthy of acceptance.

Date

ADVISOR Dr. Brain T. Helenbrook

EXAMINING COMMITTEE

Dr. Eric F. Thacher

Dr. Frederick Carlson

Abstract

A thermoelectric generator (TEG) using the exhaust waste heat from an automobile has the potential to replace the existing alternator system in an automobile, and thus improve fuel economy and reduce emissions. To evaluate the performance and the effects of using a TEG in an automobile, an automotive exhaust thermoelectric generator system (AETEG) model has been developed. The vehicle components modeled include the engine, exhaust, coolant, and TEG. In the current work, the exhaust, coolant, and TEG system models were developed and validated against the results from the experimental testing of a prototype TEG installed in 1999 GMC Sierra pick-up truck. The exhaust system model was adjusted using experimental data and predicts the temperature drop in the exhaust to within 18% of the experimental results. The coolant system model predicts reasonably well, such that the effect of TEG on the performance of the coolant system could be reliably predicted. The TEG model predicts the power generated to within 67%. This large difference is due to the effects of heat losses and non-uniform flow in the TEG that were not included in the model. Thus, the model has already proved useful in indicating possible improvements to the TEG. Studies are currently being performed to further optimize the device.

Nomenclature

Symbol	Units	Description
Upper Case Roman		
A	m^2	Cross sectional area of a system.
A_c	m^2	Cross sectional area.
A_c	m^2	Total heat transfer area on the coolant side.
A_h	m^2	Total heat transfer area on the exhaust side.
A_n	m^2	Cross sectional area of a n-type thermoelectric leg.
A_p	m^2	Cross sectional area of a p-type thermoelectric leg.
D	m	Hydraulic diameter.
D_h	m	Hydraulic diameter.
D_i	m	Inside diameter of a circular tube.
I	A	Current.
J	$-$	Jacobian of a matrix.
K	$\frac{W}{^oK}$	Thermal conductance.
K_M	$\frac{W}{^oK}$	Thermal conductance of a thermoelectric module.
K_c	$\frac{W}{^oK}$	Thermal conductance of a thermoelectric couple.

L	m	Horizontal length of a system.
	m	Total length for a flat plate.
Nu_D	$-$	Nusselt number based on the hydraulic diameter.
$\overline{Nu_D}$	$-$	Average Nusselt number for a pipe in a cross flow.
$\overline{Nu_o}$	$-$	Avergae Nusselt number over the heated length for a flow over a flat plate.
$\overline{Nu_o}\|_{\xi=0}$	$-$	Average Nusselt number without the unheated starting length for a flow over a flat plate.
P	W	Electrical power.
Pr	$-$	Prandtl number.
Q	W	Heat conduction in radial direction.
	W	Heat flow in axial direction.
	$\frac{m^3}{s}$ or gpm	Volumetric flow rate.
Q_1	W	Convective heat transfer at the hot surface.
	W	Energy lost by the exhaust gas.
	W	Heat input into the thermoelectric module.
Q_2	W	Convective heat transfer at the cold surface.
	W	Energy lost to the coolant.
R_L	Ω	Load resistance.
R_i	Ω	Internal resistance.
R_{i_M}	Ω	Internal resistance of a thermoelectric module.
R_{i_c}	Ω	Internal resistance of a thermoelectric couple.

Re	$-$	Reynolds number.
Re_D	$-$	Reynolds number defined based on the hydraulic
Re_L	$-$	Reynolds number defined based on the length of a flat plate.
T_b	^oC	Bulk temperature of the exhaust gas.
	^oC	Bulk temperature of a fluid.
T_c	^oC	Cold junction temperature in a thermoelectric couple or module.
T_{c_i}	^oC	Coolant inlet temperature into the TEG.
T_{c_o}	^oC	Coolant outlet temperature into the TEG.
T_{c_s}	^oC	Coolant side surface temperature of a thermoelectric module.
T_h	^oC	Hot junction temperature in a thermoelectric couple or module.
T_{h_i}	^oC	Exhaust inlet temperature into the TEG.
T_{h_o}	^oC	Exhaust outlet temperature into the TEG.
T_{h_s}	^oC	Exhaust side surface temperature of a thermoelectric module.
T_s	^oC	Wall temperature of a rectangular channel.
T_{si}	^oC	Inside surface temperature of the exhaust pipe.
T_{so}	^oC	Outside surface temperature of the exhaust pipe.
T_∞	^oC	Ambient temperature.
V	V	Voltage.
V_o	V	Electromotive force.
	V	Open circuit voltage.
W_{shaft}	J	External work done on a system.

Z	$-$	Figure of merit of a thermoelectric material.
Z_1	m	Elevation of node 1 above some horizontal reference plane.
Z_2	m	Elevation of node 2 above some horizontal reference plane.

Lower Case Roman

c_p	$\frac{kJ}{kgC}$	Specific heat of the exhaust gas at T_b.
c_{p_c}	$\frac{kJ}{kgC}$	Specific heat of the coolant.
c_{p_h}	$\frac{kJ}{kgC}$	Specific heat of the exhaust gas.
f	$-$	Fanning friction factor.
fr	$-$	Moody friction factor.
g	$\frac{m}{s^2}$	Acceleration due to gravity.
h	m	Height.
	m	Total head available.
	m	Total head losses in a system.
h_c	$\frac{W}{m^{2o}C}$	Heat transfer coefficient on the coolant side.
h_h	$\frac{W}{m^{2o}C}$	Heat transfer coefficient on the exhaust side.
h_i	$\frac{W}{m^{2o}C}$	Internal heat transfer coefficient in an exhaust pipe.
h_o	$\frac{W}{m^{2o}C}$	External heat transfer coefficient for the flow over an exhaust pipe.
j	$-$	Colburn factor.

k	$-$	Iteration counter.
	$\frac{psi}{gpm^2}$	Loss coefficient of a system.
	$\frac{W}{m^oC}$	Thermal conductivity of a fluid.
	$\frac{W}{m^oC}$	Thermal conductivity of the exhaust pipe material.
l	m	Fin length.
l_n	m	Length of n-type thermoelectric leg.
l_p	m	Length of p-type thermoelectric leg.
m	$-$	Ratio of load resistance to internal resistance.
m_c	$\frac{Kg}{s}$	Mass flow rate of the coolant.
m_h	$\frac{Kg}{s}$	Mass flow rate of the exhaust.
$\dot{m}$	$\frac{Kg}{s}$	Mass flow rate of the exhaust.
p_1	$pascal$	pressure at node 1.
p_2	$pascal$	pressure at node 2.
q_h	W	Heat input into the thermoelectric module.
q_μ	$\frac{W}{m^3}$	Rate of heat absorption per unit volume.
q_π	W	Rate of heat absorption or liberation.
r	$-$	Radial direction.
r_i	m	Inner radius of the exhaust pipe.
r_o	m	Outer radius of the exhaust pipe.
s	m	Transverse spacing.
t	m	Thickness.
u	$\frac{m}{s}$	Velocity of a fluid.
u_m	$\frac{m}{s}$	Mean fluid velocity.
u_1	$\frac{m}{s}$	Velocity of the fluid at node 1.
u_2	$\frac{m}{s}$	Velocity of the fluid at node 2.
$\overrightarrow{x}$	$-$	Vector of unknowns.

Upper Case Greek

$\triangle p$	*Pa or psi*	Pressure drop.
$\triangle T$	^oC	Temperature Difference.

Lower Case Greek

α	$\frac{V}{^oK}$	Seebeck coefficient.
α_M	$\frac{V}{^oK}$	Seebeck coefficient of a thermoelectric module.
α_c	$\frac{V}{^oK}$	Seebeck coefficient of a thermoelectric couple.
α_n	$\frac{\mu V}{^oK}$	Seebeck coefficient of a n-type thermoelectric material or leg.
α_p	$\frac{\mu V}{^oK}$	Seebeck coefficient of a p-type thermoelectric material or leg.
$\overline{\alpha}$	$\frac{\mu V}{^oK}$	Seebeck coefficient of a thermoelectric material averaged over T_h and T_c.
η_t	$-$	Thermal efficiency of a thermoelectric couple or module.
η_c	$-$	Carnot efficiency.
λ_n	$\frac{mW}{cm^oK}$	Thermal conductivity of a n-type thermoelectric leg.
λ_p	$\frac{mW}{cm^oK}$	Thermal conductivity of a p-type thermoelectric leg.
$\overline{\lambda}$	$\frac{mW}{cm^oK}$	Thermal conductivity of a thermoelectric material averaged over T_h and T_c.
μ	$\frac{V}{^oK}$	Thomson coefficient.
	$\frac{Kg}{ms}$	Dynamic viscosity of a fluid.
ν	$\frac{m^2}{s}$	Kinematic viscosity of a fluid.
π	V	Peltier coefficient.

ρ	$\frac{Kg}{m^3}$	Density of a fluid.
	$m\Omega cm$	Electrical resistivity of a thermoelectric material.
$\overline{\rho}$	$m\Omega cm$	Electrical resistivity of a thermoelectric material averaged over T_h and T_c.
ρ_n	$m\Omega cm$	Electrical resistivity of a n-type thermoelectric material or leg.
ρ_p	$m\Omega cm$	Electrical resistivity of a p-type thermoelectric material or leg.

Subscripts

bpC	By-pass circuit.
$engC$	Engine circuit.
$htrC$	Heater circuit.
$radC$	Radiator circuit.
tot	Total.

Contents

List of Figures

List of Tables

Chapter 1

Introduction

Fuels based on petroleum have assumed a position of undisputed leadership in the transportation sector throughout the world. However, due to factors such as the United States growing dependence on depleting oil reserves, environmental issues, CAFE (corporate average fuel economy) regulations etc., alternative fuels and propulsion systems are being sought that can provide an increase in efficiency and reduction in emissions. Many commercial, environmental and socio-economic benefits can be attributed to improvement in fuel economy. A few of these are as follows:

- "Despite an increasingly energy efficient economy the U.S remains dependent on foreign oil. Of the 19.5 million barrels of oil Americans consume everyday, about 11.5 million are imported. Roughly half the oil consumed in the U.S goes for cars and trucks [1]."

- The United States has the highest rate of carbon emissions in the world. One-third of these are transportation related [2]. Failure to increase the fuel economy of the vehicles is a predominant contributing factor towards the increase of carbon emissions. With the carbon dioxide being the dominant green house gas, vehicle emissions are a significant cause of global warming.

- Future automobiles must generate more power to support features such as collision avoidance systems, vehicle stability control, navigation etc, while reducing fuel consumption and emissions.

- Corporate average fuel economy (CAFE) is the sales weighted average fuel economy, expressed in miles per gallon (mpg), of a manufacturer's fleet of passenger cars or light trucks with a gross vehicle weight rating (GVWR) of 8,500 lbs. or less, manufactured for sale in the United States, for any given model year. The purpose of regulating CAFE is to reduce energy consumption by increasing the fuel economy of cars and light trucks. Truck CAFE has been increased for the period 2005 to 2007, from 21 mpg today to 22.2 mpg in 2007 [3]. Car CAFE has not been changed for many years. But Congress has charged National Highway Transportation Safety Authority (NHTSA) to produce a study and recommendation for car CAFE increases. Therefore any technology that might improve the fuel economy may be very important to the automotive companies to enable them to meet the increased CAFE requirements.

- Currently the Federal Test Procedure (FTP) for establishing the fuel economy for CAFE and "window sticker" on vehicles, includes a very low electrical load (250 watts), because no accessories or lights are on during the test. In actual operation many electrical loads, lights, fans for AC or heat, radio, electrical power steering, etc, that could total 700 to 1500 watts might be on. Therefore any update of electrical load for the FTP will be a challenge for the automotive companies to meet these requirements.

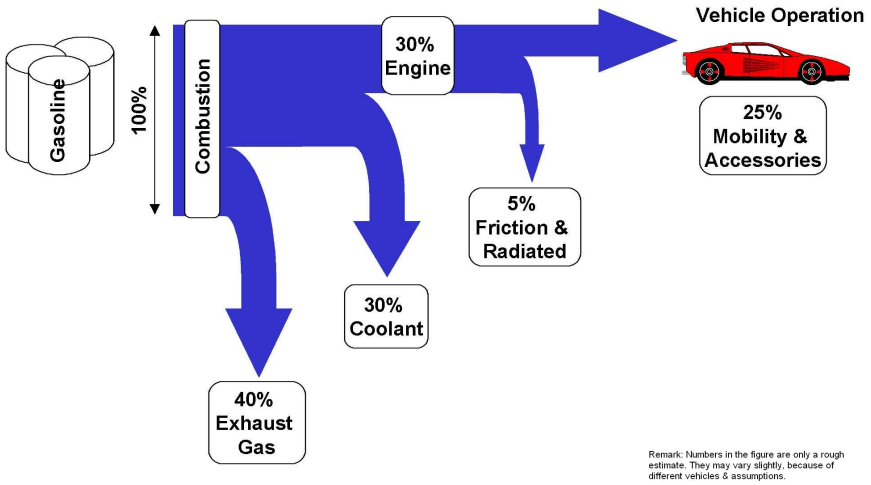

Figure 1.1: Typical energy path in gasoline fueled internal combustion engine vehicle [4].

1.1 Means for Improving Fuel Economy

Engines that burn gasoline or diesel fuel propel almost all passenger cars and light duty trucks. A schematic of the energy budget for a gasoline-fueled internal combustion engine vehicle is shown in figure (1.1). About 70% of the available energy in the fuel is rejected as heat in the exhaust and coolant. The remainder is transformed into mechanical energy or work. Some of the work is used to overcome frictional losses in the transmission and other parts of the drive train and to operate the vehicle accessories (alternator, coolant pump, fuel pump etc.). As a result only about 20 to 25% of the original energy contained in the fuel is actually used to propel the vehicle. This propulsion energy overcomes (1) the inertia when accelerating or climbing hills, (2) the aerodynamic drag, and (3) the rolling resistance of the tires on the road. Consequently there are two general ways to reduce vehicle fuel consumption: (1) increase the overall efficiency of the powertrain (engine, transmission, final drive) in order to deliver more work from the fuel consumed and (2) reduce the required work (weight, aerodynamics, rolling resistance and accessory load) to propel the vehicle.

1.2 Exhaust Energy Recovery

Waste heat from the exhaust gas from the vehicle accounts for a considerable portion of the fuel energy that is not utilized, about 40% from figure (1.1). Therefore a means to improve the fuel economy is to increase the overall efficiency of the powertrain by recovering waste heat from the exhaust gas of the vehicle. According to "1999 Bosch Automotive electrics and electronics Handbook" the average electrical power consumption of an automobile is about 600 watts [5]. This load is carried by an inefficient engine/alternator system. The objective is to reduce the load on the alternator and consequently on the engine by converting the waste heat from the exhaust gas of the vehicle into electrical energy. Clarkson University has formed a team to design, build, test and simulate a prototype automotive exhaust thermoelectric generator (AETEG), that offsets the engine shaft power by converting the waste heat into electrical energy.

The AETEG works on the principle of thermoelectricity: when the junctions formed by joining two dissimilar current carrying conductors are maintained at different temperatures, an electro motive force (emf) is generated in the circuit. The current carrying conductors are known as thermoelectric elements and the couple formed out of the two current carrying conductors is known as thermoelectric couple. In a typical generator heat exchangers are used to transfer heat from the heat source and the sink to junctions of the thermocouple. The heat exchangers and the thermoelectric couple unit is known as a thermoelectric generator (TEG). The AETEG has the vehicle exhaust gas as its heat source and the engine coolant as its heat sink. Thermoelectric conversion is a solid-state technology with no moving parts, which is simple and reliable.

From the above discussion the complete AETEG system can be categorized into (1) Exhaust system, (2) Coolant system, and (3) TEG system. The definition and significance of each of these subsystems are discussed in later chapters.

1.3 Previous TEG Modeling and Experiments

One of the early studies on a TEG was performed by Richard H. Bauer of Clarkson University during (1961-1963) [6]. Bauer investigated the feasibility of designing a TEG which could provide auxiliary electrical energy for an automobile. The engine cooling water was used as the heat source while the cold junction heat exchanger using ambient air as the working fluid was used as the heat sink. Lead telluride was the only thermoelectric material considered for this study. The investigation showed that a TEG using the engine cooling water as a heat source would not be feasible, due to the large volume and cross-sectional area of thermoelectric material necessary to yield the required electrical power output. The large volumes and cross-sectional areas required are attributed to the combined effects of the low Carnot and low thermocouple efficiencies encountered by operating with the relatively low-grade heat source. It was also concluded that utilizing a thermoelectric generator on an automotive engine was worthy of further investigation if the heat source could be kept close to 600 ^oK.

Parallel to Bauer's work, Anthony Joseph Tomarchio of Clarkson University conducted a feasibility study of increasing an automobile engine efficiency by replacing the alternator with a TEG by converting waste energy in the exhaust gases to electrical power [7]. Air was used as the heat sink fluid and lead telluride as the thermoelectric material. The principal conclusions from this study were as follows: (1) the maximum power requirements of 514 *watts* at 14.7 *volts* was met at approximately

50 mph, (2) the combined power output of the battery and the generator below 50 mph down to 20 mph would provide the minimum power requirements, and (3) unless improved semiconductors materials become available, the minimum power requirements cannot be satisfied at speeds below 20 mph.

Birkholz et al. designed a TEG that uses $FeSi_2$-thermoelements [8]. They tested their generator on a Porsche 944 engine and reported a maximum electrical power of 58 $Watts$ at full engine power. A total of 90 thermoelements were used in the generator.

A predominant work in the design, construction and testing of a TEG for mobile applications was performed by Hi-Z Inc. Bass et al. at Hi-Z studied novel methods of recovering waste heat from Diesel engines [9]. The study consisted of evaluating various heat sources: energy lost through the radiator, the intercooler, the lubricating oil system, and the exhaust in diesel engines. They concluded that the exhaust system offered the most potential for thermoelectric based heat recovery due to the high available temperature difference between the heat source and the heat sink. In the same study Hi-Z also investigated various thermoelectric materials compatible with these heat sources to determine the materials and generator configuration required to achieve the most economic and direct conversion of heat to electricity. The thermoelectric materials that were studied consisted of bismuth-telluride (Bi_2Te_3), lead-telluride, and silicon-germanium family of alloys. Their study concluded that the bismuth-telluride offered the best performance and operability in spite of its lower maximum operating temperature. Use of Bi_2Te_3 system minimizes the amount of heat transfer area required to conduct the heat into the thermoelectric elements. This decreases the pressure drop across the exhaust heat exchanger resulting in a lower back pressure on the engine. Based on these studies, using exhaust gas and Bi_2Te_3 as the heat source and the thermoelectric material, Hi-Z designed and tested a 1 kW

prototype TEG [10]. The prototype thermoelectric generator consisted of seventy two 13 $Watt$ Bi_2Te_3 thermoelectric modules. The prototype TEG was tested on a $14L$ 350 hp Cummins NTC engine. A maximum power output of 1068 $Watts$ was obtained at 300 hp and 1700 rpm.

Ikoma et al. at Nissan Research Center, designed a TEG using silicon germanium ($SiGe$) thermoelectric modules [11]. The module consisted of eight couples of p-type and n-type $SiGe$ elements. The maximum electrical power output from the module is approximately 1.2 $Watts$. A total of 72 such modules were used in the generator. The modules were arranged between an exhaust pipe with a rectangular cross section and water jackets around the exhaust pipe. The generator was installed in a 3000 $c.c$ engine vehicle. A maximum electrical power output of 35.6 $Watts$ was produced by the generator at 60 $\frac{km}{h}$ during an uphill climb.

Crane et al. did a theoretical study to evaluate the integration of thermoelectric modules into the radiator system of an automobile [12]. The study was performed under the assumption that 30 to 50% of the total fuel energy may be expelled through the radiator. The objective of their study was to design a thermoelectric radiator system, that can displace the alternator system. Bi_2Te_3 thermoelectric material was used in their studies. The modeling was performed based on the dimensions of typical stock radiator used in GM Chevrolet Suburban. After validating the baseline radiator model (without the thermoelectric modules) against actual radiator performance data, the study focussed on what should be the optimal modifications to the radiator dimensions that would achieve high thermoelectric power output with minimal additional system weight and parasitic losses. The study concluded that: (1) with current (Bi_2Te_3) thermoelectric technology it might be feasible to displace current day alternator system with such a thermoelectric radiator and (2) penalties such as increased radiator size or increased accessory power are minimal.

Vazequez et al. [13] reviewed "the main characteristics and evolution of the different investigations performed over the last three decades concerning the use of thermoelectric power generation using the heat from the exhaust gases produced in the combustion process of an automobile." Their study concluded that the maximum electrical power generated in TEGs for cars has varied between (43 to 193) $watts$. This power was achieved normally in a car running at 65 $\frac{km}{h}$ uphill. However, the same TEGs have been inefficient for other working conditions, such as during idling, because the temperature range of the exhaust gas did not match with the optimal working temperatures of the thermoelectric modules.

1.4 Current Thesis Work

From the literature reviewed in the previous section, it can be noticed that these studies have been focused on either theoretical work or experimental testing. Also, none of the studies conducted in the past reported any precise estimates for the percent fuel savings, which is the final objective of a TEG being installed in an automobile. There has not been any work reported that has a complete AETEG system model based on both the theory and experiments, where the model developed from the theory is validated against the experimental testing. Such an AETEG system model will be an useful tool for performing various parametric and system optimization studies under a wide range of operating conditions of the vehicle. Also, with such a model the change in performance of various subsystems of the vehicle due to the addition of the TEG can be evaluated reliably.

A complete AETEG system model should include a vehicle system model, an exhaust system model, a coolant system model, an electrical system model, and a TEG system model. The exhaust system model and the coolant system model are important with respect to the TEG, as the performance of the TEG is a function of inlet temperature and mass flow rate of the exhaust and the coolant into the TEG. Therefore the subsystems for the exhaust, the coolant, and the TEG should be detailed and extensive. All of these systems are integrated into the overall vehicle system model. The current thesis consists of modeling the exhaust, coolant, and the TEG subsystems and validating these models against the results from the experimental testing. Also in the conclusions, we discuss how these models will be used in developing an overall AETEG system model for future studies.

Chapter 2

Hi-Z HZ20 Thermoelectric Module Modeling

HZ20 modules built by Hi-Z Technology, Inc.[1] (Hi-Z) are the power generating units in our AETEG. Therefore the design of the generator is governed by the performance characteristics of the HZ20 module. The following chapter discusses thermoelectric principles and gives an overview of the electrical properties of HZ20 module as a function of temperature. It also provides a model of the HZ20 module and the validation of the estimated thermoelectric properties against the data available in the literature.

2.1 Thermoelectricity

Thermoelectricity deals with the direct conversion of heat into electricity, or vice-versa, in solid or liquid conductors by means of three interrelated phenomena - the Seebeck effect [14], the Peltier effect [14], and the Thomson effect [14].

[1]Hi-Z Technology, Inc. 7606 Miramar Road, San Diego, CA 92126-4210, USA.

In 1821 Thomas Johann Seebeck discovered that when two different current carrying conductors are joined into a loop, with a temperature difference maintained between the two junctions formed by the loop, an electromotive force (emf) is generated. Such a loop is called a thermocouple, the emf generated is known as a thermoelectric emf or Seebeck voltage, and the phenomenon is known as the Seebeck effect. The Seebeck effect is defines as:

$$V_o \;=\; \alpha \triangle T \tag{2.1}$$

where V_o is the emf generated, $\triangle T$ is the temperature difference between the junctions, and α is the seebeck coefficient defined as the ratio of the electric field to the temperature gradient along the conductor. He also concluded that the magnitude of the emf generated was proportional to the temperature difference, depended on the type of conducting material, and is not a function of temperature distribution along the conductors.

Later in 1834 Peltier discovered that when an electric current passes through two different conductors connected in a loop, one of the junctions between the conductors absorbs heat while the other releases heat. This effect is known as Peltier effect. However he failed to understand the complete implications of his findings and it was not until four years later that Lenz concluded that there is a heat absorption or liberation at the junctions depending on the direction of the current flow. As shown in figure (2.1), consider a current I flowing through a junction formed between two different materials A and B held at constant temperature T. This electrical current I generates a thermal current, the magnitude and direction of which depends on the Seebeck coefficients of the conductors A and B. If the Seebeck coefficients of the two conductors are different, the thermal energy will leave the junction at a different rate

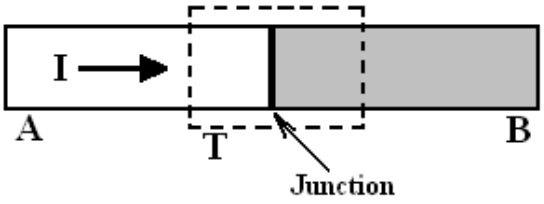

Figure 2.1: Current I flowing through a junction formed between two different materials A and B held at constant temperature T

than it is entering. Thus heat is absorbed or liberated at the junction. The Peltier effect can be defined as:

$$q_\pi = \pi I \tag{2.2}$$

where q_π is the rate of heat absorption or liberation, I is the current, and π is the Peltier coefficient.

William Thomson in 1851, trying to explain discrepancies between experimental results and a relationship between α and π, postulated the existence of an additional reversible generation of heat when a temperature gradient is applied to a current carrying conductor. This is known as Thomson heat and is proportional to the product of the current and the temperature gradient. Thomson heat is reversible, i.e, heat is either generated or liberated when the direction of either the current or temperature gradient is reversed, but not concurrently. The Thomson heat can be defined as:

$$q_\mu = \mu I \triangle T \tag{2.3}$$

where q_μ is the rate of heat absorption per unit volume, I is the current, $\triangle T$ is the temperature gradient, and μ is the Thomson coefficient defined as the ratio of rate of heat absorption per unit volume to the applied current and temperature gradient.

Using equilibrium thermodynamics, Thomson established a relationship between the above three effects, equations (2.1), (2.2), and (2.3), called the Kelvin (or Kelvin-Onsager) relations. The Kelvin-Onsager relations are defined by the equations (2.4) and (2.5).

$$\frac{\pi}{T} = \alpha \tag{2.4}$$

$$\frac{\mu}{T} = \frac{d\alpha}{dT} \tag{2.5}$$

2.1.1 Thermal Efficiency and Thermoelectric Figure of Merit

Figure (2.2) illustrates a thermoelectric circuit (or couple) consisting of two dissimilar homogeneous materials A and B, their junctions maintained at hot junction temperature T_h and cold junction temperature T_c ($T_h > T_c$), and the terminals 1 and 2 of the circuit are connected to an external load R_L.

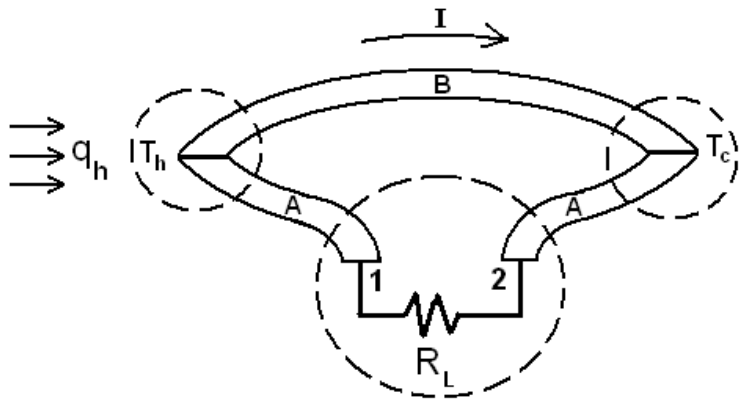

Figure 2.2: Thermoelectric circuit

The thermal efficiency, η_t of the circuit shown in figure (2.2) can be defined as [15]:

$$\eta_t = \frac{P}{q_h} \tag{2.6}$$

where P is the electrical power delivered to the external load R_L and q_h is the heat input required to maintain the hot junction temperature at T_h. The electrical power P is defined by the equation (2.7) [15]:

$$P \;=\; I^2 R_L \tag{2.7}$$

where I is the current flowing through the circuit and is a ratio of emf generated across the circuit to the total resistance of the circuit, defined by the equation (2.8) [15].

$$I \;=\; \frac{\alpha \triangle T}{R_i + R_L} \tag{2.8}$$

where R_i is the internal resistance of the materials A and B. The heat input to the hot junction is defined by the equation (2.9) [15],

$$q_h \;=\; K \triangle T + \alpha T_h I - \frac{1}{2} I^2 R_i \tag{2.9}$$

where K, α, and R_i are the thermal conductance, Seebeck coefficient, and total electrical resistance of the materials A and B. The terms $(K \triangle T)$ and $(-\frac{1}{2} I^2 R_i)$ in equation (2.9) are resulting from the two irreversible effects of heat transfer due to thermal conduction and Joule heating. While the term $(\alpha T_h I)$ is due to the reversible Peltier effect.

Using equations (2.7), (2.8), (2.9), and $(m = \frac{R_L}{R_i})$ the thermal efficiency defined in equation (2.6) can be redefined as:

$$\eta_t \;=\; \frac{m \left(\frac{\triangle T}{T_h} \right)}{\left(\frac{1+m^2}{T_h} \right) \left(\frac{R_i K}{\alpha^2} \right) + (m+1) - \frac{1}{2} \frac{\triangle T}{T_h}} \tag{2.10}$$

For a fixed temperatures (T_h and T_c) and load resistance (R_L), the thermal

efficiency can be maximized when the term $(\frac{R_i K}{\alpha^2})$ in the denominator of equation (2.10) is minimized. Also, α, R_i, and K are the thermoelectric properties. Therefore we redefine the grouping of properties called the thermoelectric figure of merit (Z) defined as:

$$Z = \frac{\alpha^2}{R_i K} \tag{2.11}$$

The higher the thermoelectric figure of merit (F.O.M), greater the thermal efficiency of the circuit. The F.O.M depends on both the thermoelectric materials and the geometry of the couple.

2.2 Thermoelectric Modules

Thermoelectric modules are the basic building blocks within thermoelectric power generators or coolers. Modules consists of two or more elements of semiconductor materials that are connected electrically in series and thermally in parallel. The thermoelectric elements and their electrical interconnects are sandwiched between two ceramic substrates.

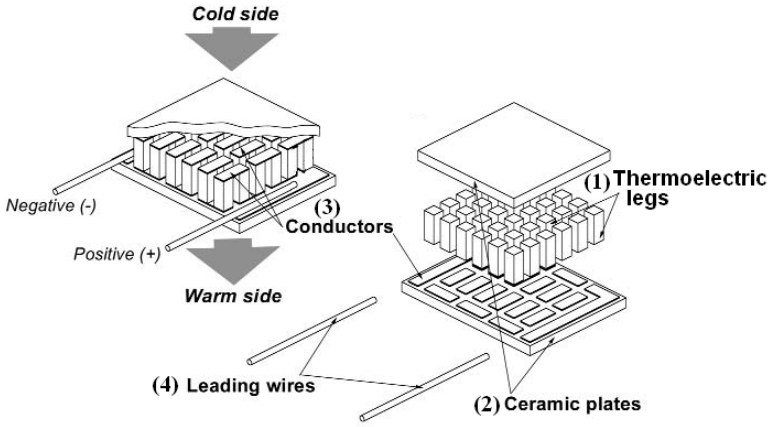

Figure 2.3: Constituents of a thermoelectric module.

Figure (2.3) shows the arrangement of the different constituents of a thermoelectric module. The main constituents of a thermoelectric module are (1) thermoelectric elements (or legs), (2) ceramic substrates, (3) electrical conductors, and (4) lead wires.

The thermoelectric elements (or legs) are the couples used for generating electricity in thermoelectric modules. They are formed out of materials such as bismuth-telluride, lead-telluride, antimony telluride, silicon-germanium semiconductor alloys. The selection of material depends on the field of application and operating temperature range. Pellets are arranged in a regular matrix with in the module, as shown in figure (2.3).

Ceramic substrates are used to insulate the thermoelectric module electrically from external mounting surfaces. The substrates must also have good thermal conductance to provide heat transfer with minimal thermal resistance. The most widely used ceramic is aluminium oxide (Al_2O_3).

Electrical conductors serves as electrical contacts between pellets. The contacts are arranged in such a way that all the pellets are connected electrically in series. For most of the low-power modules, the conductors are made as thin films (multi layer structure containing copper (Cu) as a conductor) deposited on to ceramic substrates. For high-power modules, they are made from Cu-tabs to reduce resistance.

Lead wires are used to connect the module to an electrical load in case of power generation or to an electrical source in case of the module being used for thermoelectric cooling.

2.3 Hi-Z HZ20 Thermoelectric Module

The HZ-20 module consists of 71 thermocouples arranged electrically in series and thermally in parallel. The thermocouples consist of "Hot Pressed ans Sintered", Bismuth-Telluride based semiconductors to give the highest efficiency at most waste heat temperatures as well as high strength capable of enduring rugged applications. Bonded metal conductors enable the HZ20 module to operate continuously at temperatures as high as 250^oC and intermittently as high as 400^oC without degrading the module. The HZ20 is well suited for waste heat recovery while its reversible properties make it ideal as a thermoelectric cooler, especially for high temperature applications where sensitive electronic equipment must be cooled to below the ambient temperature. Table (2.1) lists various physical and electrical properties of the Hi-Z HZ20 thermoelectric module properties [16]. The most important of these are the maximum continuous temperature and maximum intermittent temperature. These properties limit the application of HZ20 modules to locations to those in which the temperature limits are not exceeded.

2.3.1 Electrical Properties

The electrical properties of the HZ20 are dependent upon the load to which it is connected. The current-voltage curve in figure (2.4) shows the dependence of these properties as a function of current when the hot junctions of the module are at 230^oC and the cold junctions of the module are at 30^oC [16].

Property	Value	Tolerance
Physical properties		
Width and length	7.5 cm	± 0.25 cm
Thickness	0.508 cm	± 0.25 cm
Weight	115 grams	± 3 grams
Compressive yield stress	70 MPa	minimum
Number of active couples	71 couples	-
Thermal properties		
Design hot side temperature	230 °C	± 10
Design cold side temperature	30 °C	± 5
Maximum continuous temperature	250 °C	-
Maximum intermittent temperature	400 °C	-
Thermal conductivity at design temperatures	0.024 W/cmK	+ 0.001
Heat flux at design temperatures	9.54 W/sqcm	± 0.5
Electrical properties (as a generator) at design temperatures		
Power at matched load	19 watts	minimum
Load voltage	2.38 volts	± 0.1
Internal resistance	0.3 Ohm	± 0.05
Current	8 Amps	± 1
Open circuit voltage	5.0 volts	± 0.3
Efficiency	4.5 %	minimum

Table 2.1: Physical and electrical properties of the Hi-Z HZ20 thermoelectric module [16].

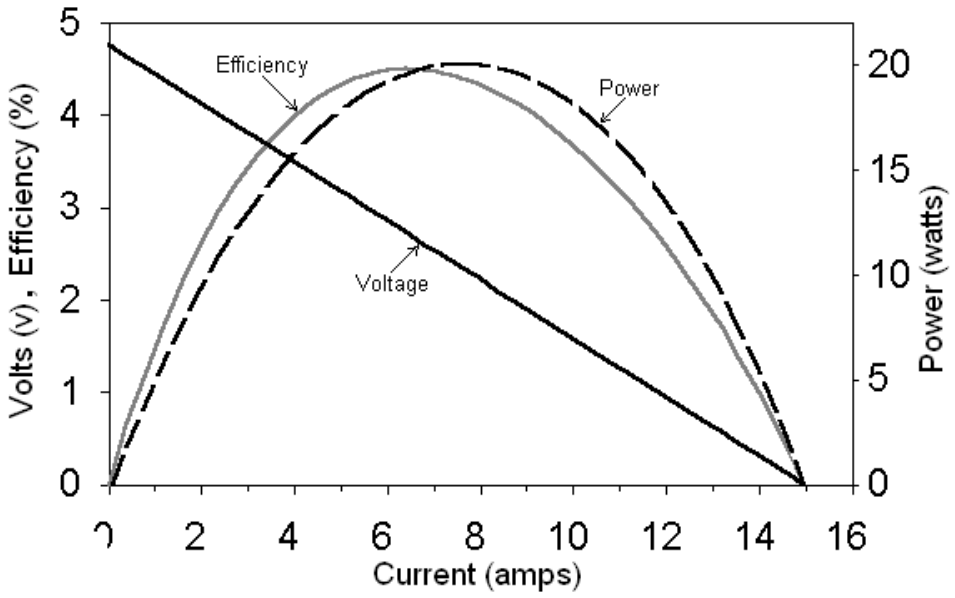

Figure 2.4: Current-voltage curves for a Hi-Z HZ20 thermoelectric module at $T_h = 230^oC$ and $T_c = 30^oC$.

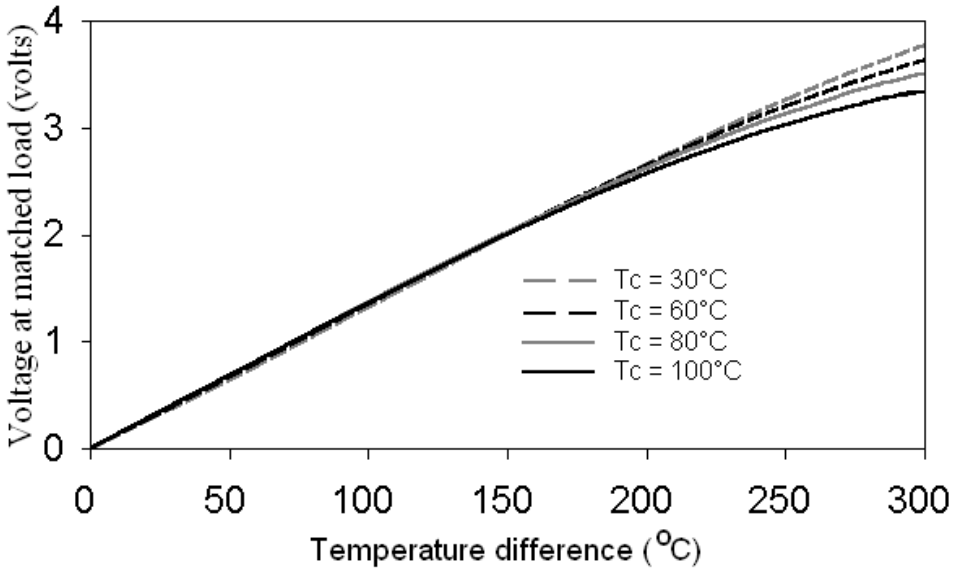

Figure 2.5: Voltage generated by the thermoelectric module at various hot and cold junction temperatures.

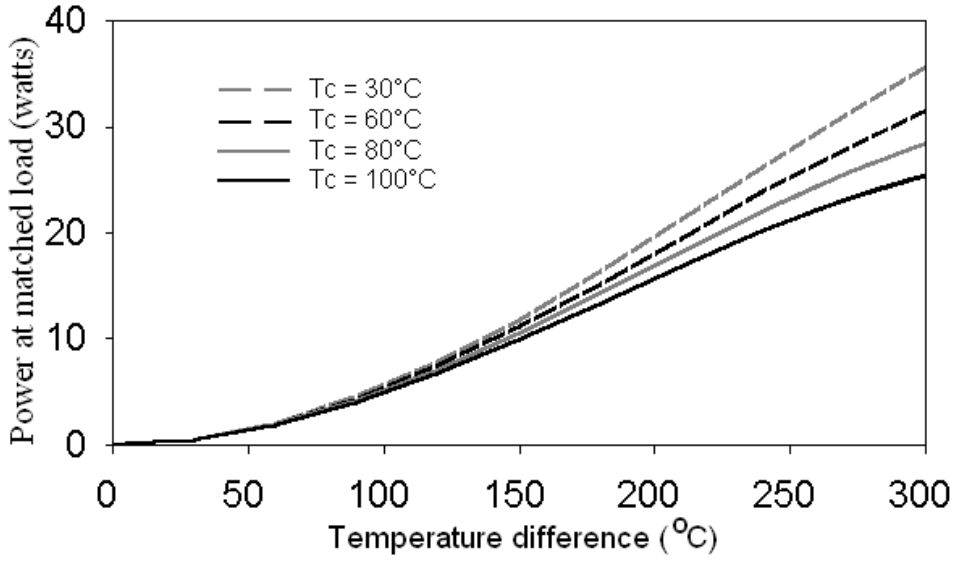

Figure 2.6: Power generated by the thermoelectric module at various hot and cold junction temperatures.

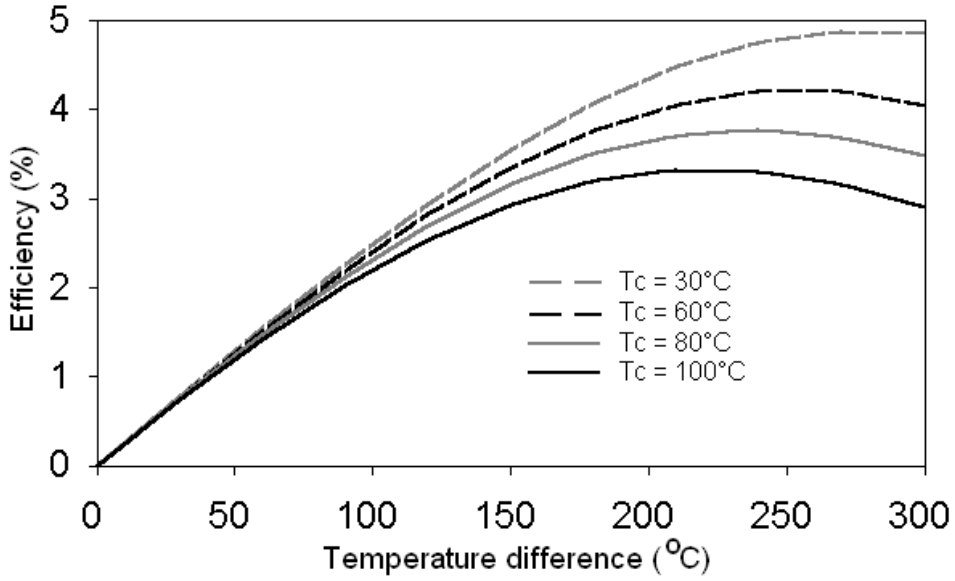

Figure 2.7: Efficiency of the thermoelectric module at various hot and cold junction temperatures.

Variation of voltage, power and efficiency as a function of hot and cold junction temperatures for the HZ20 module are shown in figures (2.5), (2.6), and (2.7) [16]. T_c is the cold junction temperature of the module and the temperature difference on x-axis is between the hot and cold junctions of the module. The curves in figures (2.5), (2.6), and (2.7) are based on the tests conducted by Hi-Z.

Figures (2.5) and (2.6) show that the voltage and power increases as the difference between the hot and cold junction temperatures increases. Also at a given temperature difference, the voltage and power generated by the thermoelectric module is highest for the lowest cold junction temperature. The efficiency of the thermoelectric module also increases with the increase in temperature difference and reaches a maximum at a certain temperature difference and decreases thereafter, as shown in figure (2.7).

2.4 Hi-Z HZ20 Thermoelectric Module Modeling

This section consists of evaluating the three important properties α, R_i, and K of the HZ20 module. A one-dimensional model based on the experimental data obtained from the tests conducted by Hi-Z, has been developed. Given the hot and cold surface temperatures of the module, the model predicts the properties: α, R_i, and K. These three properties can be further used in estimating the voltage and power delivered by the thermoelectric module for the given hot and cold surface temperatures.

2.4.1 Estimation of α

The voltage generated by the thermoelectric module connected to an external load, R_L can be defined as:

$$V = IR_L \tag{2.12}$$

using equation (2.8), equation (2.12) can be redefined as:

$$V = \frac{\alpha \triangle T}{R_i + R_L} R_L \tag{2.13}$$

At matched load ($R_i = R_L$), therefore using equation (2.13) α can be found as:

$$\alpha = \frac{2V}{\triangle T}. \tag{2.14}$$

The data for the voltage in equation (2.14) is obtained from figure (2.5). Thus the variation of the Seebeck coefficient as a function of hot and cold junction temperatures of the module can be evaluated. The Seebeck coefficient thus evaluated at various T_h and T_c is shown in figure (2.8).

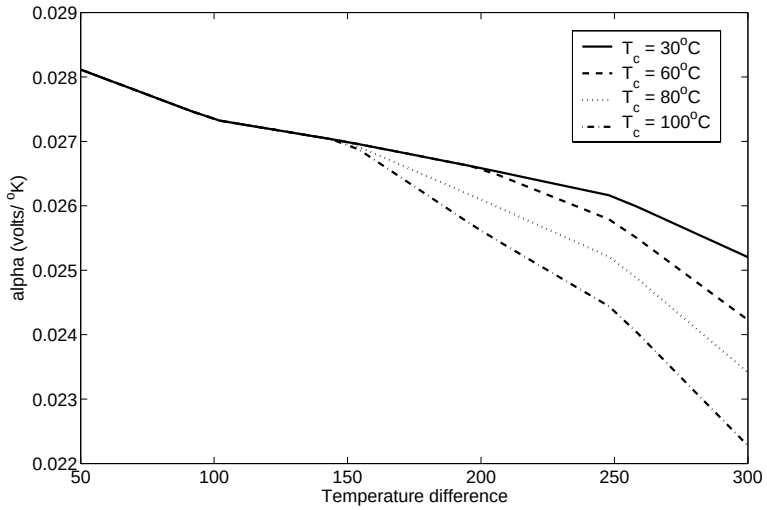

Figure 2.8: α of Hi-Z HZ20 thermoelectric module evaluated at various T_h and T_c using the analysis from section (2.4.1).

2.4.2 Estimation of R_i

Using equations (2.7) and (2.12), R_i at matched load can be found as:

$$R_i \;=\; \frac{V^2}{P}. \tag{2.15}$$

The data for the voltage and power in equation (2.15) are obtained from figures (2.5) and (2.6). Thus the variation of the internal resistance as a function of hot and cold surface temperatures of the module can be evaluated. The internal resistance thus evaluated at various T_h and T_c is shown in figure (2.9).

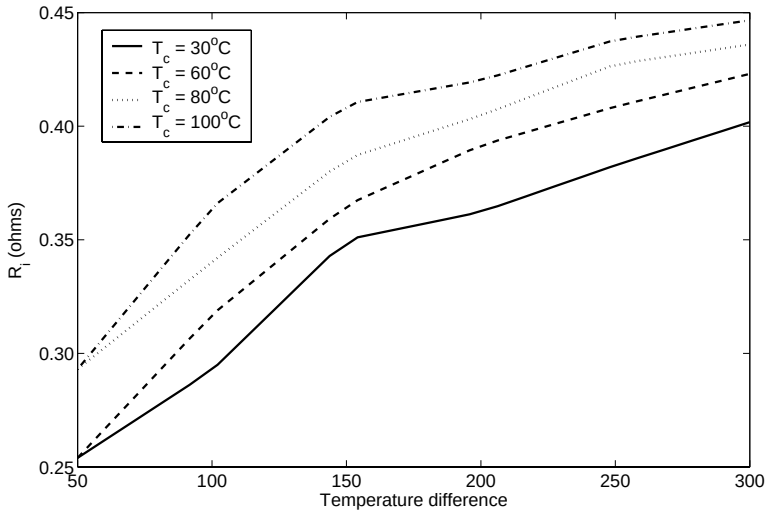

Figure 2.9: R_i of Hi-Z HZ20 thermoelectric module evaluated at various T_h and T_c using the analysis from section (2.4.2).

2.4.3 Estimation of K

The current generated by the thermoelectric module can be defined as:

$$I = \frac{P}{V} \tag{2.16}$$

using equations (2.14), (2.15), and (2.16), equation (2.9) can be redefined as:

$$q_h = K\triangle T + 2P\frac{T_h}{\triangle T} - \frac{P}{2}. \tag{2.17}$$

Using equations (2.6) and (2.17) the thermal conductance of the Hi-Z HZ20 module can be found as:

$$K = \frac{P}{\triangle T}\left(\frac{1}{2} + \frac{1}{\eta_t} - \frac{2}{\eta_c}\right) \tag{2.18}$$

where η_c is the Carnott efficiency defined by the equation (2.19).

$$\eta_c \;=\; \frac{T_h - T_c}{T_h} \tag{2.19}$$

The data for P and η_t in estimating K is obtained from figures (2.6) and (2.7). Thus the variation of the thermal conductance as a function of hot and cold surface temperatures of the module can be evaluated. The thermal conductance thus evaluated at various T_h and T_c is shown in figure (2.10).

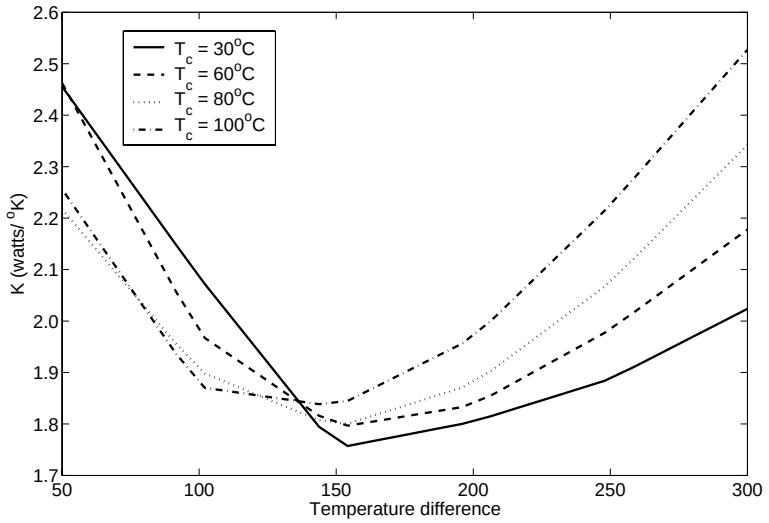

Figure 2.10: K of Hi-Z HZ20 thermoelectric module evaluated at various T_h and T_c using the analysis from section (2.4.3).

2.5 Validation of HZ20 Module Modeling

In this section validation is performed for α, R_i, and K of HZ20 module, that were evaluated based on the analysis discussed in section(2.4). Validation is performed using the thermoelectric material properties data from the literature [17]. The material against which the validation is performed is similar to the thermoelectric material used in the HZ20 module.

The HZ20 module consists of 71 thermocouples, therefore the Seebeck coefficient of a module consisting of 71 couples can be defined as:

$$\alpha_M = 71\alpha_c \tag{2.20}$$

where α_c is the Seebeck coefficient of a single couple. Similarly the internal resistance and the thermal conductance of a module consisting of 71 couples can be defined as:

$$R_{i_M} = 71R_{i_c} \tag{2.21}$$

$$K_M = 71K_c \tag{2.22}$$

where R_{i_c} and K_c are the internal resistance and the thermal conductance of a single couple. α_M, R_{i_M}, and K_M for the HZ20 module are evaluated based on the total voltage, power, and efficiency produced by the 71 couples of a single module. Therefore a multiplication factor of 71 was used while defining α_M, R_{i_M}, and K_M in terms of α_c, R_{i_c}, and K_c.

Each couple in a module is itself a thermoelectric generator consisting of n-type and p-type thermoelectric legs. Therefore α_c, R_{i_c}, and K_c in terms of n-type and p-type thermoelectric material properties can be defined as follows:

The seebeck coefficient for a single couple can be defined as [15]:

$$\alpha_c \;=\; |\alpha_n| + \alpha_p \tag{2.23}$$

where α_n and α_p are seebeck coefficients of the n-type and p-type thermoelectric legs.

The internal resistance for a single couple can be defined as [15]:

$$R_{i_c} \;=\; \rho_n \left(\frac{l_n}{A_n}\right) + \rho_p \left(\frac{l_p}{A_p}\right) \tag{2.24}$$

where ρ, A, and l are the electrical resistivity, cross-sectional area, and length of the thermoelectric legs. And the subscripts n and p represent the n-type and p-type thermoelectric legs.

The thermal conductance of a thermoelectric couple can be defined as [15]:

$$K_c \;=\; \lambda_n \left(\frac{A_n}{l_n}\right) + \lambda_p \left(\frac{A_p}{l_p}\right) \tag{2.25}$$

where λ_n and λ_p are the thermal conductivities of the n-type and p-type thermoelectric legs.

Using equations (2.20 to 2.25), the seebeck coefficient, the internal resistance, and the thermal conductance of a module in terms of α, ρ, and λ for the n-type and p-type thermoelectric legs can defined as follows:

$$\alpha_M \;=\; 71\,[|\alpha_n| + \alpha_p] \tag{2.26}$$

$$R_{i_M} \;=\; 71\left[\rho_n \left(\frac{l_n}{A_n}\right) + \rho_p \left(\frac{l_p}{A_p}\right)\right] \tag{2.27}$$

$$K_M \;=\; 71\left[\lambda_n \left(\frac{A_n}{l_n}\right) + \lambda_p \left(\frac{A_p}{l_p}\right)\right]. \tag{2.28}$$

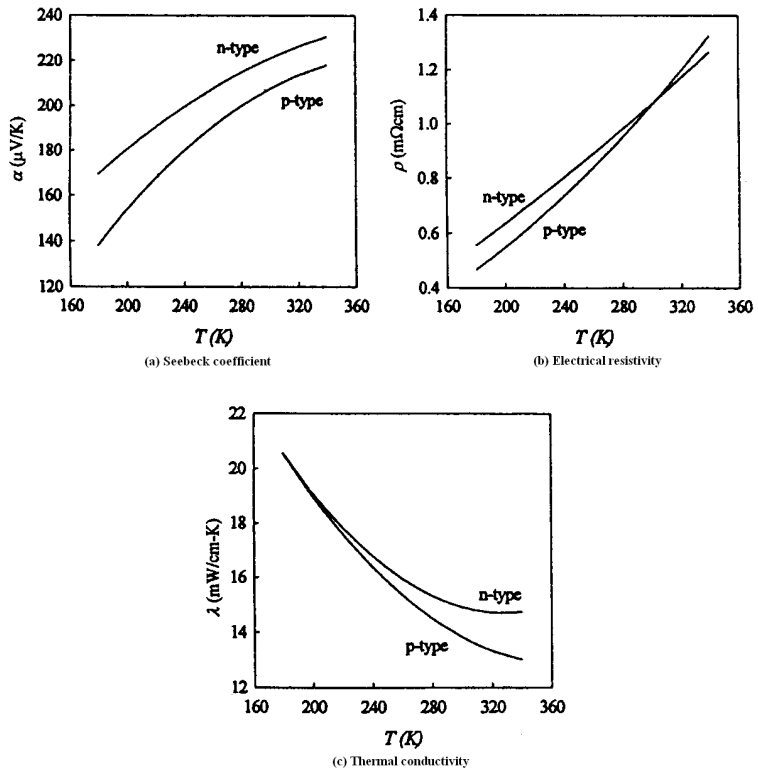

Figure 2.11: The thermoelectric properties of typical melt-grown $Bi_2Te_3 - Sb_2Te_3 - Bi_2Se_3$ alloys. The absolute value of the n-type Seebeck coefficient is plotted [17].

Figure (2.11) shows the thermoelectric properties α, ρ, and λ of a typical melt-grown $Bi_2Te_3 - Sb_2Te_3 - Bi_2Se_3$ alloys for both the n-type and p-type, as a function of temperature. The thermoelectric properties α and λ for both the n-type and p-type at a given T_h and T_c can be calculated using the data from the curves in the figure (2.11) and then averaging these properties over T_h and T_c. The average of a thermoelectric property between two temperatures is defined as [15]:

$$\overline{x} \equiv \left(\frac{1}{\triangle T}\right) \int_{T_c}^{T_h} x(T) dT \tag{2.29}$$

where $\overline{x}$ is the property α or λ averaged over T_h and T_c and $x(T)$ is a function representing the variation of α or λ as a function of temperature. Whereas the thermoelectric property ρ at a given T_h and T_c is calculated using a modified version of the equation (2.29) [15]:

$$\overline{\rho} \;=\; \left(\frac{1}{\overline{\lambda}\triangle T}\right)\int_{T_c}^{T_h}\rho(T)\lambda(T)dT \tag{2.30}$$

where $\overline{\lambda}$ and $\overline{\rho}$ are the properties λ and ρ averaged over T_h and T_c. The reason for using equation (2.30) to calculate $\overline{\rho}$ is that for $I = 0$ it gives the correct R_i, K, and V when used in the constant property equations [15].

Given T_h, T_c, and n-type and p-type thermoelectric properties of a material as a function of temperature, similar to the data shown in figure (2.11), the thermoelectric properties α_M, R_{i_M}, and K_M of a module consisting of 71 couples can be calculated using equations (2.29) and (2.30) and (2.26), (2.27), and (2.28). Thermoelectric module properties calculated in this manner based on the data shown in figure (2.11), at $T_h = 55^oC$ and $T_c = 30^oC$ are listed in table (2.2). In the same table and at the same T_h and T_c the thermoelectric module properties for HZ20 module calculated using the analysis from sections (2.4.1), (2.4.2), and (2.4.3) are also listed.

Thermoelectric Module Property	Hi-Z HZ20 Module Properties based on the analysis from section ( )	Module Properties based on the data from figure ( )
$\alpha_M\,(\frac{volts}{^oK})$	0.0299	0.0311
$R_{i_M}\,(ohms)$	0.2014	0.1272
$K_M\,(\frac{watts}{^oK})$	3.4778	1.8773

Table 2.2: A comparison of the thermoelectric module properties of HZ20 to a module consisting of 71 couples and a thermoelectric material similar to that of HZ20 module.

Comparing the two sets of values in table (2.2), it can be concluded that the calculated thermoelectric module properties of HZ20 based on the analysis from section (2.4), are physically realistic. The difference between the two sets of values can be due to (1) the material composition of the HZ20 module, (2) the exact physical dimensions of the thermoelectric legs, or (3) other parameters that have not been taken into consideration, such as thermal and electrical resistance of the electrical conductors used in the Hi-Z HZ20 module to connect different couples or the solders that are used in connecting the thermoelectric legs to the electrical conductors. The major difference is probably due to the material composition of HZ20 module. Although the Hi-Z HZ20 module consists of Bi_2Te_3, we do not know the exact composition for the material.

This shows that the experimental data and the analysis used in section (2.4) to calculate the thermoelectric properties of HZ20 module is physically resonable. Thus this model can be used reliably to model the TEG system as discussed in a later chapter. Based on the performance characteristics of the HZ20 modules it can be summarized that to maximize the power generated by the TEG, the hot surface temperature of the module should be as high as possible and the cold surface temperature of the module should be as low as possible. Therefore higher hot surface temperature and lower cold surface temperature are the principal governing factors that influence the design of the generator.

Chapter 3

AETEG Design and Experimental Testing

The design of an automotive exhaust TEG is governed by the performance of HZ20 modules and the exhaust and the coolant system characteristics of the test vehicle. This chapter examines various design parameters that were used in finalizing the design and the interface between the TEG and the truck systems. It also discusses the experimental testing performed on the system.

3.1 TEG Design

As discussed in section (2.3.1), for a fixed cold-side surface temperature of the module, the power generated increases with an increase in temperature difference across the module, and for a fixed temperature difference across the module the power generated is highest for the lowest cold side surface temperature. Therefore, for maximum power we need a generator design that maximizes the temperature difference across the module and minimizes the cold side temperature. This does not give maximum

efficiency, but our interest is in maximum power. Therefore to maximize the power production, the hot junction temperature should be as high as possible and the cold junction temperature as low as possible, subject to system and material limitations. The principal factors limiting the possible hot junction temperatures are: (1) the distance between the engine exhaust headers and the exhaust inlet of TEG, (2) the thermal resistance between the hot junctions and the exhaust gas, and (3) the maximum continuous hot junction temperature specified for the HZ-20. The factors limiting reduction of the cold junction temperatures are: (1) the thermal resistance between the cold junctions and the coolant and (2) the coolant inlet temperature.

The design based on these considerations is shown in figure (3.1). The TEG system consists of sixteen HZ-20 modules that are connected in series. Eight modules are arranged on each side of the exhaust heat exchanger, such that the maximum possible energy is extracted from the exhaust. The waste heat is rejected to the test vehicle's engine cooling system by means of two aluminum heat exchangers, one for each set of eight modules. A counter flow arrangement was used to enhance the heat transfer rate and to have a uniform temperature difference between the exhaust and the coolant, along the length of the heat exchanger.

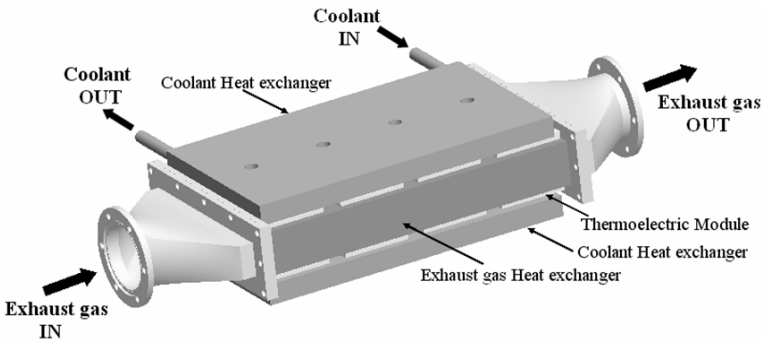

Figure 3.1: A prototype TEG system without its outer casing.

3.2 AETEG System

The above TEG system was connected to the exhaust, coolant, and the electrical systems of the test vehicle 1999 GMC Sierra. The coupling between each of these systems is described below.

3.2.1 Exhaust System

The exhaust gas temperature that the TEG receives is determined by the location of TEG within the exhaust section. As shown in figure (3.2), for the test vehicle, GMC Sierra 1999, the exhaust gas from the engine comes out from the two exhaust headers, and then flows through the right and left catalytic converters. To achieve high exhaust gas temperatures the thermoelectric generator must be located just downstream of the exhaust headers. But there is a concern that if the generator was located upstream of the catalytic converters, it would increase the warming time of the catalytic converters, thus increasing the pollutants discharged ([18], [19]). Added to this there is no space towards the upstream of the catalytic converters to install the generator. Also, in order to achieve the design power the generator would have to be made in two sections, one for each header. For these reasons, the chosen location was after the junction of the exhaust pipes from the two catalytic converters. The location containing the generator is an underbody space bounded by a frame cross beam at the forward end, the muffler at the rear end, the drive shaft on the left and the frame on the right.

3.2.2 Coolant System

Engine coolant was chosen to cool the generator instead of air-cooling because engine coolant is always available and the coolant heat exchangers can be smaller because

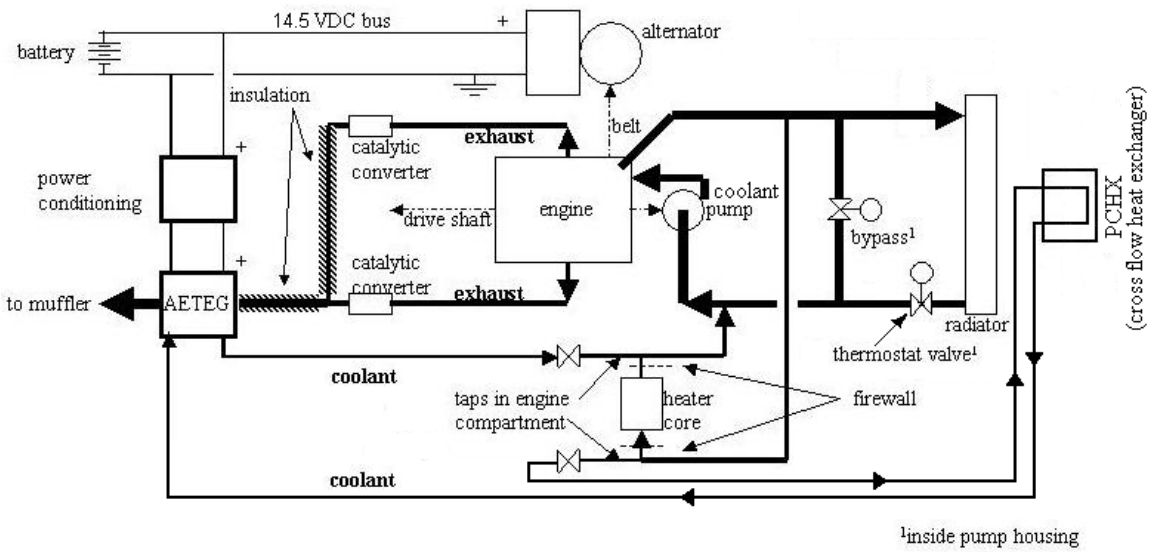

Figure 3.2: An automotive exhaust TEG system schematic.

of the larger heat transfer coefficient available with liquid cooling. However, unlike air-cooling, its use requires additional coolant pumping power. Also, most of the heat removed from the exhaust is delivered first to the engine cooling system and only then is rejected to the atmosphere through the radiator.

The most desirable point to tap into the coolant system is just after the radiator because this is the coldest point in the system. However, the closing of the thermostat valve would then prevent coolant from flowing to the TEG. For this reason, the only option was to take and return coolant from the cabin heater supply and return hoses, respectively. Ironically, the temperature of the coolant supplied to the generator is the highest in the coolant system. This motivated the installation of a pre-cooling heat exchanger (PCHX). The PCHX provided a means to assess the effect of lowering the coolant inlet temperatures. The PCHX was a cross flow heat exchanger located in front of the vehicle and fastened to the bumper.

3.2.3 Electrical System

The power generated by the TEG is supplied to the vehicle electrical bus through the power conditioning unit (PCU). The PCU is essentially a DC-to-DC converter functioning as a buck regulator, matched the generator's output voltage to that of the test truck's DC bus voltage.

Using these system designs as the basis, the modeling was performed for the exhaust, coolant and the TEG systems that are discussed in later chapters.

3.3 Experimental Testing of AETEG system at Delphi Corporation

To use the predictions made by the models reliably, the results from the exhaust, coolant, and the TEG system models need to be validated. The validation was performed against the results from the experimental testing of a prototype automotive exhaust TEG system, installed in a 1999 GMC Sierra pick-up truck. The testing was performed at Delphi, Inc., in Lockport, NY. The following were the objectives of the testing: (1) to observe the effect of the TEG system on the truck systems, (2) to measure the performance of the TEG, and (3) to acquire measurements against which the predictions of different models associated with the TEG system could be compared. This chapter consists of a brief overview of different test configurations conducted under various speeds and conditions and the variables that were measured.

3.3.1 Test Matrix

The testing was performed mainly under 4 different configurations. Configuration (A) corresponds to the baseline testing without the TEG installed. Configuration (B) corresponds to the testing performed with the TEG installed and the PCHX inoperative. Configuration (C) corresponds to the testing with the TEG, exhaust pipes insulation and air flow through the PCHX blocked. The exhaust pipes between the outlet of the catalytic converters and the inlet of TEG were insulated using Thermo-Tec exhaust wrap and aluminium backed high temperature glass fiber insulation. Configuration (D) corresponds to the testing with TEG, exhaust insulation, and PCHX operative.

Configuration (C) was tested to evaluate the effect of exhaust inlet temperature on the performance of TEG, whereas configuration (D) was tested to evaluate the effect of coolant inlet temperature on the performance of TEG.

Under each of these configurations constant speed tests were conducted at 30, 50, and 70 mph. At each constant speed test, runs were made corresponding to the tunnel ambient temperature of 40^oF, 70^oF, and 100^oF. To determine the effect of electrical loading on the performance of the TEG, at a given speed and tunnel ambient temperature 3 different tests were run corresponding to an electrical load of $Base$, $(Base + 25)$, and $(Base + 50)$ $amps$. The base load was about 35 amps including the day time running lights [20]. The resulting test matrix is tabulated in table (3.1).

Configuration	Vehicle speed (mph)	Tunnel ambient temperature (^oF)	Electrical load (amps)
A, B, C, or D	30	40	Base
			Base+25
			Base+50
		70	Base
			Base+25
			Base+50
		100	Base
			Base+25
			Base+50
	50	40	Base
			Base+25
			Base+50
		70	Base
			Base+25
			Base+50
		100	Base
			Base+25
			Base+50
	70	40	Base
			Base+25
			Base+50
		70	Base
			Base+25
			Base+50
		100	Base
			Base+25
			Base+50

Table 3.1: Test matrix showing various configurations of tests conducted at Delphi corporation.

During each of these tests, measurement of several variables were recorded. Some of the important variables that were recorded are: temperature of the exhaust gas, coolant, and thermoelectric module surfaces, the mass flow rates of the exhaust gas and coolant, gauge and differential pressures for the assessment of back pressure and estimation of loss coefficients of various components in the coolant and the exhaust systems, current and voltage measurements for use in power and efficiency calculations of the TEG, and torque, RPM and fuel consumption for calculation of the power of the vehicle and the fuel savings. The variables that were measured and the location of their measurements are shown in figure (3.3).

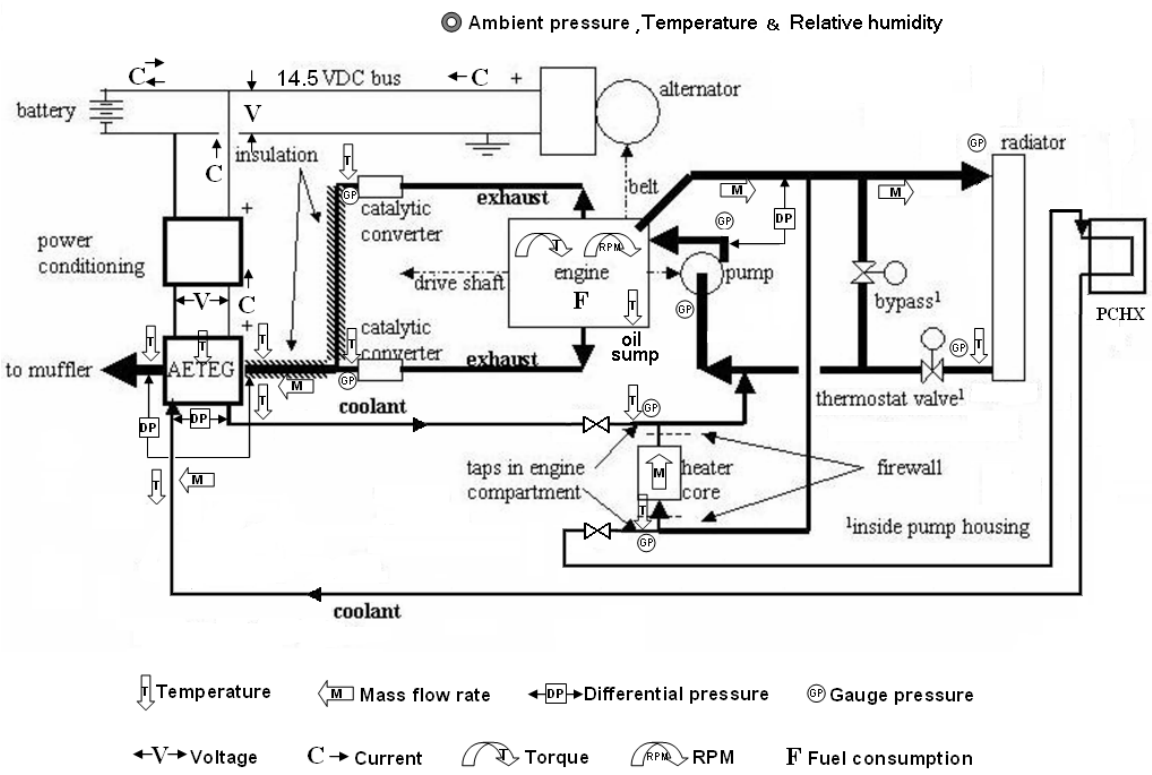

Figure 3.3: Measured variables and the locations at which the measurements were performed during the Delphi testing.

Some of these measurements from the testing are used in validating the predictions made by the exhaust, coolant, and the TEG system models. The validation of these models will be discussed in later chapters.

Chapter 4

Exhaust System Modeling of 1999 GMC Seirra Pickup Truck

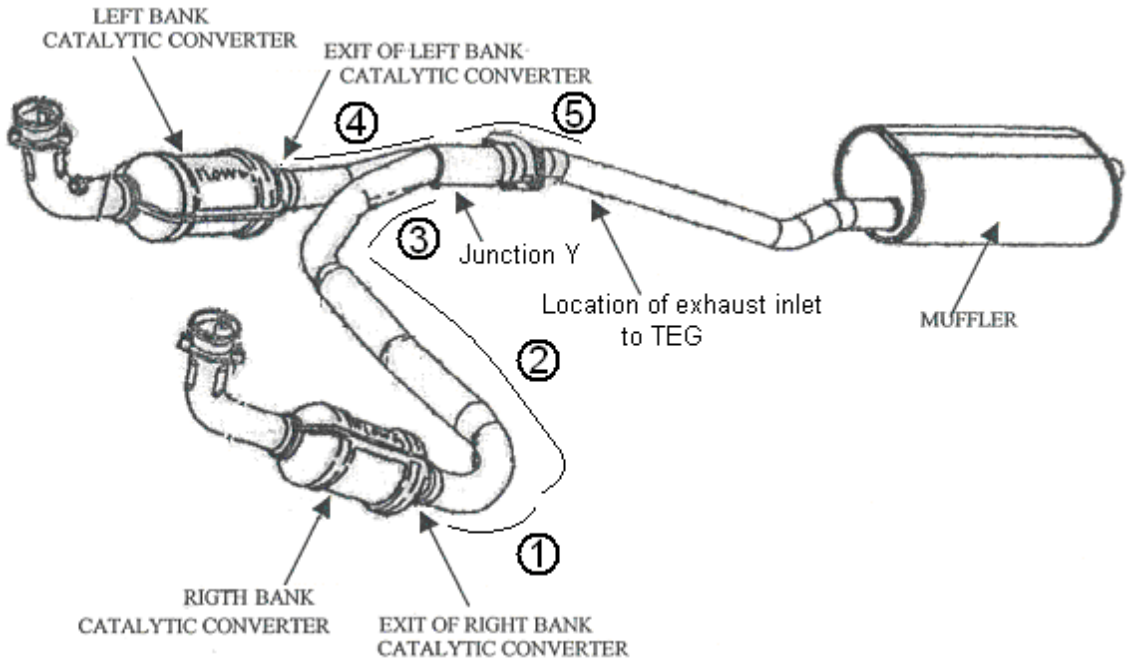

Figure 4.1: Physical layout of the exhaust system of a 1999 GMC Sierra pickup truck.

In this chapter modeling of the exhaust system that estimates the inlet temperature to the TEG system is discussed. Figure (4.1) shows the physical layout of the exhaust system of a 1999 GMC Sierra pickup truck. The exhaust from the engine passes through the two exhaust headers, before it flows through the left and right catalytic converters. The exhaust then continues to flow through the respective exhaust pipes connected to the left and right catalytic converters before mixing at junction Y and finally passes through the muffler and out into the atmosphere.

4.1 Modeling

Given the bulk temperature and mass flow rate of the exhaust at the exit of the left and right catalytic converters, the ambient temperature, and the vehicle velocity, the model predicts the bulk temperature of the exhaust at the inlet to the TEG. The predicted bulk temperature is used as an input variable into the TEG model to predict the power generated by the TEG. The exhaust system model accounts for the heat lost by the exhaust as it flows from the exit of the catalytic converters to the inlet of the TEG. The model also includes the effect of insulating the exhaust pipe which reduces the amount of heat lost by the exhaust before it reaches the inlet of the TEG.

The complete system has been categorized into five sections as shown in figure (4.1). On each section a 1-D energy balance has been performed to predict the variation of bulk temperature of the exhaust along the axial direction of the exhaust pipe. The analysis has been performed under the following assumptions: (1) the exhaust mass flow rate and bulk temperature at the exit of the right and left catalytic converters are equal, (2) the velocity of external air flowing over sections 1, 2, 3, 4, and 5 is equivalent to the vehicle speed, (3) the temperature at junction Y is the

average of the exit temperatures of section 3 and 4. This is justified because the mass flow rates are assumed to be the same and we also assume instantaneous mixing, and (4) the exhaust flow inside the pipe is fully developed.

The energy flow in the axial direction of the exhaust pipe can be defined as:

$$Q = \frac{d}{dx}(\dot{m}c_p T_b) \tag{4.1}$$

where Q is the heat loss transfer rate per unit length, $\dot{m}$ is the exhaust mass flow rate, T_b is the bulk temperature of the exhaust at the inlet of the pipe, and c_p is the specific heat of the exhaust at T_b. The heat conduction in the radial direction through the exhaust pipe can be defined as:

$$Q = -k2\pi r\frac{dT}{dr} \tag{4.2}$$

where k is the thermal conductivity of the exhaust pipe material. The material of the exhaust pipe is assumed to be plain carbon steel, and r and T are the radius and the temperature of the exhaust at a given cross section along the radial direction. The convective flux balance at the inner surface of the exhaust pipe can be defined as:

$$Q = h_i 2\pi r_i(T_b - T_{si}) \tag{4.3}$$

where h_i is the internal convective heat transfer coefficient, r_i is the inner radius of the exhaust pipe, and T_{si} is the inside surface temperature of the exhaust pipe. The convective flux balance at the outer surface of the exhaust pipe can be defined as:

$$Q = h_o 2\pi r_o(T_{so} - T_\infty) \tag{4.4}$$

where h_o is the external convective heat transfer coefficient, r_o is the outer radius of the exhaust pipe, T_{so} is the outside surface temperature of the exhaust pipe, and T_∞ is the ambient temperature of the external fluid flowing over (or parallel to) the exhaust pipe. Solving equations (4.2), (4.3), and (4.4) we can find T_{si}, T_{so}, and Q. Q be expressed as:

$$Q = \frac{2\pi(T_b - T_\infty)}{\frac{1}{h_i ri} + \frac{ln(\frac{r_o}{r_i})}{k} + \frac{1}{h_o ro}}. \tag{4.5}$$

Assuming constant values of C_p, k, h_i, and h_o the solution to equation (4.1), using equations (4.3) and (4.5), can be expressed as:

$$T_b(x) = T_\infty + (T_b|_{x=0} - T_\infty)e^{-Cx} \tag{4.6}$$

where the parameter C is defined by the equation (4.7).

$$C = \frac{\frac{2\pi}{\dot{m}c_p}}{\frac{1}{h_i ri} + \frac{ln(\frac{r_o}{r_i})}{k} + \frac{1}{h_o ro}} \tag{4.7}$$

Thus the variation of the bulk temperature of the exhaust gas along the axial direction of the exhaust pipe can be calculated using equation (4.6).

4.2 Convective Correlations for h_i and h_o to Calculate C in Equation (4.7)

The following section describes the assumptions and the conditions under which the correlations for the inside, h_i, and the outside, h_o, heat transfer coefficients were established.

4.2.1 Evaluation of Internal Convective Heat Transfer Coefficient

The Reynolds number for a flow in a circular tube can be defined as:

$$Re_D = \frac{\rho u_m D_i}{\mu} \tag{4.8}$$

where ρ is the density of the fluid flowing through the tube, u_m is the mean fluid velocity over the tube cross section, D_i is the inside diameter of the tube, and μ is the viscosity of the fluid flowing through the tube. The correlation for the convective heat transfer coefficient inside a circular tube is a function of Re_D. For ($Re_D < 2300$) the flow is laminar, while for ($Re_D > 2300$) the flow is turbulent. For a fully developed internal laminar flow inside a circular tube, the convective correlation [21] is a constant,

$$Nu_D = 4.36 \tag{4.9}$$

where Nu_D is the Nusselt number defined by the equation (4.10),

$$Nu_D = \frac{h_i D_i}{k} \tag{4.10}$$

where k is the thermal conductivity of the fluid. And for a fully developed internal turbulent flow inside a circular tube, the convective correlation is given by [21]:

$$\left.\begin{aligned} Nu_D &= \frac{\frac{f}{8}(Re_D - 1000)Pr}{1+12.7(\frac{f}{8})^{\frac{1}{2}}(Pr^{\frac{2}{3}}-1)} \\ f &= [0.79ln(Re_D)) - 1.64]^{-2} \end{aligned}\right\} \tag{4.11}$$

where Pr is the Prandtl number and f is the friction factor.

4.2.2 Evaluation of External Convective Heat Transfer Coefficient

The correlation for the external heat transfer coefficient is dependent on the ambient flow condition over the exhaust pipe. From figure (4.1), sections 1, 3, 4, and 5 are classified as parallel flow with unheated starting length, figure (4.2(a)), whereas section 2 is classified as a cylinder in cross flow, figure (4.2(b)).

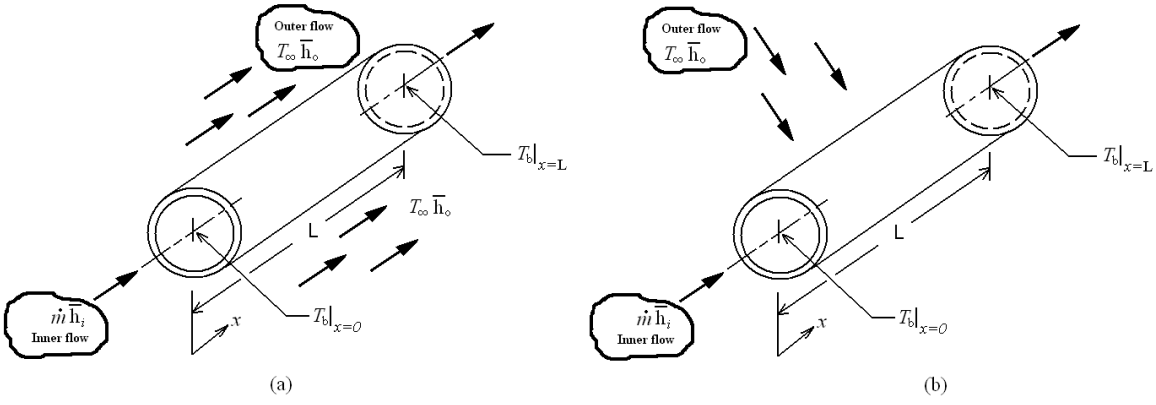

Figure 4.2: Heat transfer between fluid flowing over a pipe and fluid passing through the pipe: (a) pipe in parallel flow and (b) pipe in cross flow.

Convective correlation for a pipe in a parallel flow with unheated starting length

As shown in figure (4.3), we assume the velocity boundary layer development begins at $x = 0$, which corresponds to the vehicle leading edge. The thermal boundary layer development begins at $x = \xi$, the location where the exhaust pipe is exposed to the ambient temperature, which is about half of the vehicle length. Hence there is no heat transfer for $0 \leq x \leq \xi$. For a plate of total length L, with laminar or turbulent flow over the entire surface, the expression for the average Nusselt number of the heated length is [21]:

$$\overline{Nu_o} \;=\; \overline{Nu_o}|_{\xi=0} \left(\frac{L}{L-\xi}\right) \left[1 - \left(\frac{\xi}{L}\right)^{(2p+1)(2p+2)}\right]^{\frac{2p}{2p+1}} \tag{4.12}$$

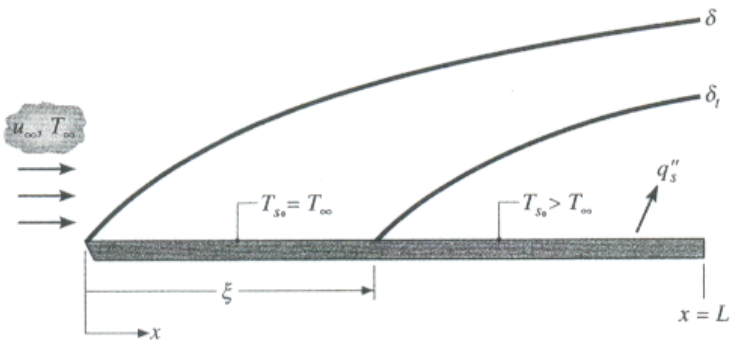

Figure 4.3: Flat plate in parallel flow.

where $p = 1$ for laminar flow and $p = 4$ for turbulent flow. $\overline{Nu_o}|_{\xi=0}$ is the average Nusselt number without the unheated starting length. For laminar flow, ($Re_L < 5 \times 10^5$) the correlation for $\overline{Nu_o}|_{\xi=0}$ can be expressed as [21]:

$$\overline{Nu_o}|_{\xi=0} \;=\; 0.664\,(Re_L)^{\frac{1}{2}}\,(Pr)^{\frac{1}{3}} \tag{4.13}$$

where as for the turbulent flow, ($Re_L >= 5 \times 10^5$) the correlation for $\overline{Nu_o}|_{\xi=0}$ can be expressed as [21]:

$$\overline{Nu_o}|_{\xi=0} \;=\; 0.037\,(Re_L)^{\frac{4}{5}}\,(Pr)^{\frac{1}{3}}\,. \tag{4.14}$$

It has to be noted that L defined in equations (4.13) and (4.14) is different from the L shown in figure (4.2).

Convective correlation for a pipe in a cross flow

The convective correlation for a pipe in cross flow can be expressed as [21]:

$$\overline{Nu_D} \;=\; C\,(Re_D)^m\,(Pr)^{\frac{1}{3}} \tag{4.15}$$

constants C and m are a function of Re_D as listed in table (4.1) [21].

Re_D	C	m
0.4 – 4	0.989	0.330
4 – 40	0.911	0.385
40 – 4000	0.683	0.466
4000 – 40000	0.193	0.618
40000 – 400000	0.027	0.805

Table 4.1: Constants C and m as a function of Reynolds number in equation (4.15) for a pipe in cross flow.

4.3 Adjustment of Model to Fit Experimental Data

In the following section a comparison of the results from the model and the experiment and the modifications that were made to minimize the difference in results between the model and the experiment are discussed. Using the catalytic outlet temperature, exhaust mass flow rate, ambient temperature, and vehicle speed from the experimental data as the input variables to the model, a corresponding value of the exhaust gas temperature drop from the exit of the catalytic converter to the inlet of TEG was predicted and compared to the experimental value.

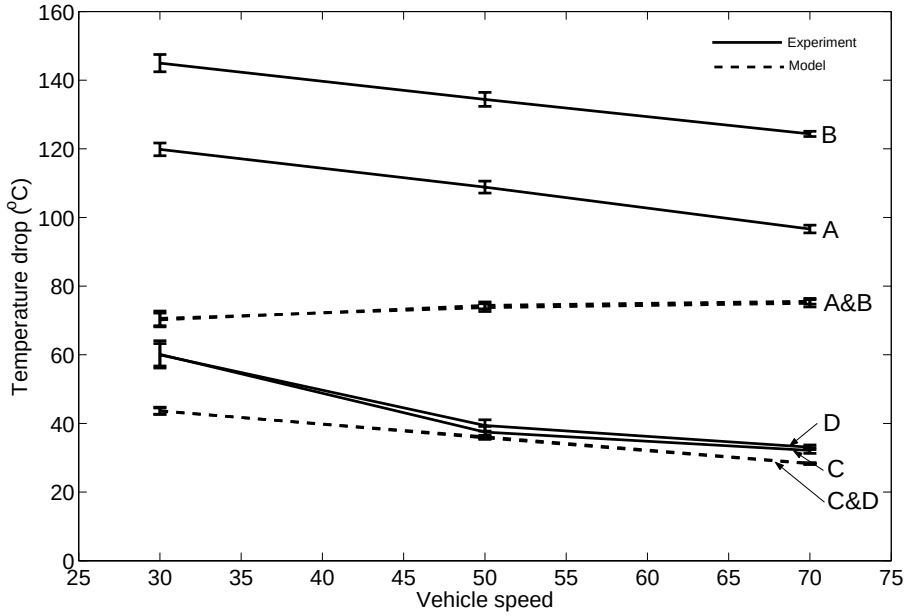

Figure 4.4: Comparison of the results from the model and the experiment for the temperature drop from the outlet of catalytic converter to the inlet of TEG.

Figure (4.4) shows a comparison of the results from the model and the experiment. Comparisons were made for all the four configurations A, B, C, and D. The vertical ranges given for each data point indicate the variability of the temperature drop with the tunnel inlet air condition and the electrical load. The effect of insulation in reducing the amount of heat lost by the exhaust gas before it reaches the inlet of TEG, configurations C and D, was modeled by increasing the thermal resistance to the heat flow to the ambient. This was accomplished by modifying the thermal conductivity of the exhaust pipe material. The thermal conductivity was reduced by 0.00011 times the actual value. This value was chosen to best fit the experimental data corresponding to the configurations C and D.

Comparing the results from the experimental testing, configuration B has a greater temperature drop compared to A, C, and D, A has a greater temperature drop compared to C and D and D has a greater temperature drop compared to C. From equation (4.6) the temperature drop from the outlet of the catalytic converter to the inlet of the TEG can be defined as:

$$T_b|_{x=0} - T_b(x) \;=\; (T_b|_{x=0} - T_\infty) - (T_b|_{x=0} - T_\infty)e^{-Cx} \tag{4.16}$$

where $T_b|_{x=0}$ is the catalytic outlet temperature and $T_b(x)$ is the temperature at the inlet of the TEG. Dividing equation (4.16) by the term $(T_b|_{x=0} - T_\infty)$, the normalized temperature drop can be defined as:

$$\frac{T_b|_{x=0} - T_b(x)}{T_b|_{x=0} - T_\infty} \;=\; 1 - e^{-Cx}. \tag{4.17}$$

Assuming constant values for C_p, k, h_i, and h_o in equation (4.7), the normalized temperature drop in equation (4.17) is a function of $\dot{m}$ and is inversely proportional to it. Therefore lower exhaust mass flow rate will cause a greater temperature drop and vice-versa.

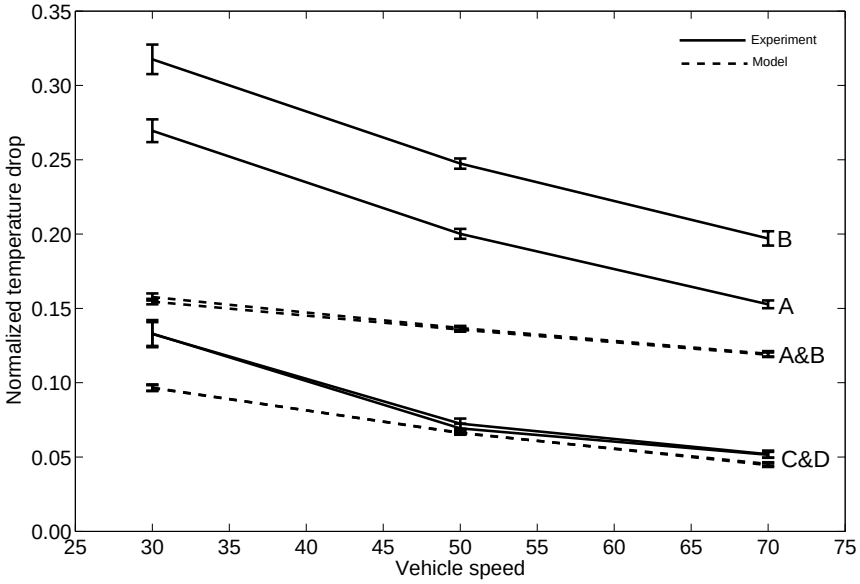

Figure 4.5: Comparison of the results from the model and the experiment for the normalized temperature drop from the outlet of the catalytic converter to the inlet of TEG.

The normalized temperature drop for the test configurations A, B, C, and D, based on the above analysis is shown in figure (4.5). In configuration B the parasitic losses from the TEG exceeded the power generated by the TEG, causing a greater fuel consumption compared to configurations A and therefore highest exhaust mass flow rate and lowest temperature drop in B should have occurred. But, on the contrary the temperature drop in B is greater compared to A. An explanation could not be attributed as to why such a phenomena has occurred.

The mean differences for the temperature drop from the outlet of catalytic converter to the inlet of the TEG between the model and the experiment at various vehicle speeds under different configurations are tabulated in table (4.2) and the maximum differences between the model and the experiment among various tests cases conducted under each configuration are tabulated in table (4.3). A positive sign represents over prediction and a negative sign indicates an under prediction by the model.

Vehicle speed	Configuration A	Configuration B	Configuration C	Configuration D
30 mph	-49.69 ^oC	-74.36 ^oC	-16.41 ^oC	-16.42 ^oC
50 mph	-34.45 ^oC	-60.67 ^oC	-1.69 ^oC	-3.28 ^oC
70 mph	-21.06 ^oC	-49.35 ^oC	-3.86 ^oC	-4.67 ^oC

Table 4.2: Mean difference for the temperature drop from the outlet of catalytic converter to the inlet of TEG between the model and the experiment for each configuration at various vehicle speeds.

Configuration	Maximum temperature difference
A	-50.49 ^oC
B	-76.90 ^oC
C	-21.38 ^oC
D	-20.07 ^oC

Table 4.3: Maximum difference for the temperature drop from the outlet of catalytic converter to the inlet of TEG between the model and the experiment among the various test cases conducted under each configuration.

From figure (4.4) and tables (4.2) and (4.3) there is a big difference in the results between the model and the experiment for configurations (A and B) and these differences for configurational cases (C and D) were lesser when compared to (A and B), because the cases (C and D) have lesser heat losses due to the insulation. These differences between the model and experiment can be due to the incorrect external convective heat transfer coefficient or exhaust mass flow rate and exhaust temperature from the exit of the left and right catalytic converters. The under side body of the vehicle has a complex geometry due to the presence of various components and structural frame of the vehicle, acting as a barrier to the external flow. This could not be accounted into the model due to the complex geometry. As a result the external flow velocity over (or parallel to) the exhaust pipe could have been different than the assumption that it is equal to the velocity of the vehicle. Therefore the variation of the external flow velocity over the exhaust pipe could have caused a difference between the theoretical and experimental external convective heat transfer coefficient. Also, there was a difference in the exhaust mass flow rate and outlet temperature between the left and right catalytic converters contrary to the assumption that they are equal. As a result a different internal convective heat transfer coefficient might have been used in the model.

The variations in the exhaust mass flow rate and outlet temperature between the right and left catalytic converters could not be verified from the experimental testing. The exhaust mass flow rate at the outlet of the left and right catalytic converters was not a measured variable. The exhaust mass flow rate was measured as the sum of intake air flow and fuel consumption. Therefore the best possible assumption was that the total exhaust mass flow rate splits up equally between the two exhaust headers. In comparison to the exhaust mass flow rate, the exhaust temperature at the outlet of the left and right catalytic converter were measured. However, the

temperature sensor at the outlet of the left catalytic converter malfunctioned during some of the test runs. Therefore the exhaust temperature at the outlet of the left catalytic converter was assumed to be equal to the exhaust temperature at the outlet of the right catalytic converter. During the test runs in which the temperature sensor at the outlet of the left catalytic converter functioned, the temperature from that sensor was usually greater than that of the exhaust temperature at the outlet of the right catalytic converter. And the difference between them varied from -12 to 34 ^oC.

The power generated by the TEG at a given engine load and speed is a function of the exhaust inlet temperature into the TEG. Therefore any error associated with the exhaust inlet temperature will cause an inaccurate estimation of fuel usage or other parameters by the AETEG system. Therefore to reduce this error due to the exhaust inlet temperature, the difference between the results from the model and the experiment for the exhaust system model were minimized. This was achieved by making modifications to the internal and external convective heat transfer coefficients. The internal convective heat transfer coefficient was enhanced by 4.6 times the actual theoretical value and the external convective heat transfer coefficient was reduced by 0.67 times the actual theoretical value. These values were chosen to best fit the experimental data. The values were determined by running the exhaust system model using various combinations of the modified internal and external convective heat transfer coefficients, such that the mean differences between the model and the experiment at vehicle speeds of 30, 50, and 70 mph were optimum minimal under all the four test configurations A, B, C, and D.

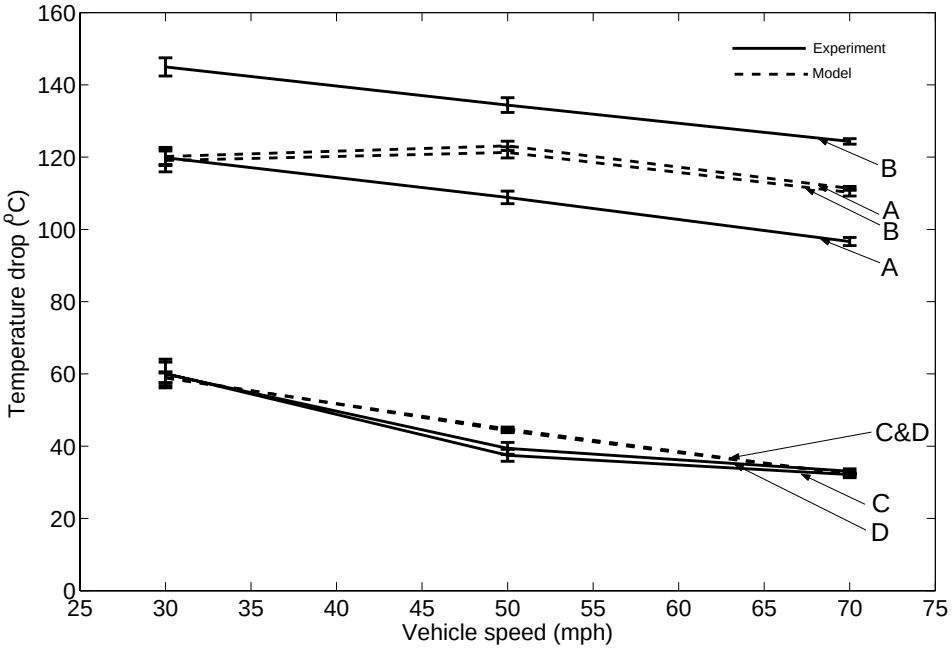

Figure 4.6: Comparison of the results from the model and the experiment for the temperature drop from the outlet of catalytic converter to the inlet of TEG with the modified internal and external convective heat transfer coefficients.

A comparison of the results between the experiment and the model based on the modified convective heat transfer coefficients are shown in figure (4.6). Comparing figures (4.4) and (4.6), the large differences between the model and the experiment in configurations A and B at 30 and 50 mph were minimized to a large extent. Also, the differences that existed in configurations C and D at vehicle speeds of 30 and 70 mph were minimized to near zero. The mean differences between the modified model and the experiment at various vehicle speeds under different configurations are tabulated in table (4.4) and the maximum differences between the modified model and the experiment among various tests cases conducted under each configuration are tabulated in table (4.5). A positive sign represents over prediction and a negative sign indicates an under prediction by the model.

Vehicle speed	Configuration A	Configuration B	Configuration C	Configuration D
30 mph	0.34 ^oC	-25.88 ^oC	-1.02 ^oC	-1.15 ^oC
50 mph	14.27 ^oC	-13.08 ^oC	6.78 ^oC	5.35 ^oC
70 mph	14.71 ^oC	-14.12 ^oC	0.05 ^oC	-0.82 ^oC

Table 4.4: Mean difference for the temperature at the inlet of TEG between the modified model and the experiment for each configuration at various vehicle speeds.

Configuration	Maximum temperature difference
A	15.60 ^oC
B	-29.54 ^oC
C	-8.05 ^oC
D	-6.37 ^oC

Table 4.5: Maximum difference for the temperature at the inlet of TEG between the modified model and the experiment among the various test cases conducted under each configuration.

4.4 Range of Reynolds Number and Heat Transfer Coefficients for the Exhaust System Model

	Internal heat transfer coefficient range							
	Theoretical							
Configuration ->	A		B		C		D	
	Reynolds number	Heat transfer coefficient $W/m^2 C$	Reynolds number	Heat transfer coefficient $W/m^2 C$	Reynolds number	Heat transfer coefficient $W/m^2 C$	Reynolds number	Heat transfer coefficient $W/m^2 C$
Vehicle Speed								
30	4315 to 10061	10.75 to 21.75	4611 to 10402	11.60 to 22.52	4427 to 9784	11.18 to 21.92	4464 to 9806	11.29 to 21.90
50	6957 to 15801	18.08 to 34.09	7111 to 16094	18.43 to 34.56	7011 to 15201	18.44 to 34.15	7032 to 15112	18.49 to 33.90
70	11142 to 25930	28.93 to 54.84	11315 to 25935	29.27 to 54.79	11051 to 24289	29.15 to 53.79	11135 to 24502	29.38 to 54.28
	Modified							
Vehicle Speed								
30	4315 to 10575	48.40 to 98.35	4611 to 10911	52.23 to 101.89	4427 to 9919	51.16 to 100.32	4464 to 9943	51.63 to 100.26
50	6957 to 16464	81.15 to 154.30	7111 to 16754	82.75 to 156.47	7011 to 15304	84.47 to 156.66	7032 to 15216	84.70 to 155.53
70	11142 to 26581	130.52 to 249.57	11315 to 26587	132.11 to 249.36	11051 to 24350	133.85 to 247.17	11135 to 24560	134.89 to 249.42
	External heat transfer coefficient range							
	Theoretical							
Vehicle Speed								
30	23300 to 1468500	30.15 to 51.63	23100 to 1371600	30.07 to 50.12	23200 to 1314700	30.19 to 50.93	23000 to 1327400	30.12 to 50.99
50	33600 to 1985200	43.29 to 68.70	33700 to 1980400	43.33 to 68.67	33500 to 1844500	43.39 to 68.15	33800 to 1855500	43.49 to 68.21
70	40000 to 2388200	53.61 to 85.93	40100 to 2392500	53.65 to 85.99	39800 to 2199900	53.74 to 84.16	40000 to 2204600	53.81 to 84.22
	Modified							
Vehicle Speed								
30	23600 to 1687600	20.20 to 35.14	23400 to 1580000	20.15 to 34.84	23300 to 1371400	20.22 to 34.27	23100 to 1385100	20.18 to 34.31
50	34100 to 2249800	29.00 to 47.73	34200 to 2238900	29.03 to 47.67	33600 to 1880900	29.07 to 45.76	33800 to 1893700	29.14 to 45.80
70	40400 to 2597300	35.92 to 58.97	40400 to 2600100	35.95 to 58.99	39800 to 2217400	36.01 to 56.50	40000 to 2222400	36.05 to 56.54

Table 4.6: Range of Reynolds number and heat transfer coefficients for the exhaust system model.

Table (4.6) shows the range of Reynolds number and the heat transfer coefficients under various configurations and vehicle speeds. Data sets corresponding to the theoretical and modified heat transfer coefficients for both the internal and external flows are listed.

4.5 Sensitivity Studies

Sensitivity studies were performed on the exhaust, coolant, and TEG subsystems. In these studies, sensitivity coefficients of various model output predictions with respect to various model parameters were evaluated. The sensitivity coefficient is defined as the ratio of percent change in the output parameter to the percent change in the model parameter. The results are listed in a tabular form. The columns correspond to the outputs and the rows correspond to the model parameters. In evaluating the

sensitivity coefficients a 10% change in the model parameter was used. Each model parameter was perturbed independently. A positive sensitivity coefficient corresponds to an increase in the magnitude of the output parameter with respect to an increase in the magnitude of the model parameter whereas a negative sensitivity coefficient corresponds to a decrease in the magnitude of the output parameter with respect to an increase in the magnitude of the model parameter. In the following section sensitivity analysis on the exhaust system modeling will be discussed. The sensitivity analysis on the coolant system and the TEG system modeling will be discussed in their respective chapters.

4.5.1 Sensitivity analysis on the Exhaust System

Table (4.7) shows the sensitivity analysis performed on the exhaust system model. Two sets of results were tabulated, corresponding to the exhaust system model based on the theoretical heat transfer coefficients and the modified heat transfer coefficients. The analysis was performed for the case of TEG with an uninsulated exhaust pipes at a vehicle speed of 30 mph, tunnel ambient temperature of 40^oF, and an electrical load of $(Base + 50)$ $amps$. This case also corresponds to the maximum difference between the model and the experiment for the temperature drop along the exhaust pipe. The most important output of the model is the temperature drop. The parameters that have strongest impact on the temperature drop, for the case of exhaust system model based on the theoretical heat transfer coefficients, are: catalytic outlet temperature, internal heat transfer coefficient, and specific heat of the exhaust gas with sensitivity coefficients of (0.678), (0.639), and (-0.828).

However, for the case of exhaust system model based on the modified heat transfer coefficients the parameters that have strongest impact on temperature drop are: catalytic outlet temperature, exhaust mass flow rate, external heat transfer coefficient, and the specific heat of the exhaust gas with sensitivity coefficients of (0.699), (-0.597), (0.570), and (-0.775).

		Model based on theoretical heat transfer coefficients		Model based on modified heat transfer coefficients	
Variable number	**Variable**	Sensititvity coefficient TEG inlet temperature	Sensititvity coefficient Temperature drop	Sensititvity coefficient TEG inlet temperature	Sensititvity coefficient Temperature drop
Input parameters					
1	Catalytic outlet temperature	1.05690	0.678	1.1003	0.6989
2	Exhaust mass flow rate	0.05840	-0.3306	0.1991	-0.5975
3	Ambient air velocity	-0.03310	0.1873	-0.1424	0.4273
4	Ambient temperature	0.00180	-0.0103	0.0038	-0.0113
Heat transfer coefficients					
5	Internal heat transfer coefficient	-0.11300	0.6394	-0.0792	0.2376
6	External heat transfer coefficient	-0.04330	0.2453	-0.1899	0.5699
Exhaust gas properties					
7	Specific heat	0.14630	-0.828	0.2582	-0.775
Thermal resistance					
8	Thermal conductivity Exhaust pipe material	-0.00001	6.67E-05	-3.64E-05	1.09E-04

Table 4.7: Sensitivity studies on the exhaust system.

Chapter 5

Coolant System Modeling

The power generated by the TEG is a function of the coolant mass flow rate into the TEG governed by the flow resistance of the TEG circuit and the system characteristics of the engine coolant system. The system characteristics of the engine coolant system includes the pump characteristics and the flow resistances of various components of the coolant system that are a function of the engine speed. Therefore the coolant mass flow rate into the TEG as a function of engine rpm is determined by the coolant system model. The coolant system model is also used in evaluating the change in performance of the coolant system due to the addition of the TEG circuit. This chapter includes (1) a brief overview about the significance and the description of the engine coolant system, (2) modeling of the coolant system, and (3) the validation of the modeling against the data from the experimental testing.

5.1 Engine Coolant System

In a gasoline fueled internal combustion engine only 20 to 25 % of the total energy contained in the fuel is used to propel the vehicle. The remainder of the available energy in the fuel is rejected as heat, primarily through two mechanisms:

- Heat carried away with the exhaust gas and dumped to the atmosphere is referred to as the "exhaust waste heat". Only a fraction of the heat and pressure in the combustion gas is used to propel the vehicle. The remainder is lost when the exhaust valve opens at the end of the power stroke and the gas is dumped to the atmosphere.

- Heat transfer from the hot combustion gas to the surfaces that contain it. Heat is transferred to the combustion chamber surfaces, valve faces, piston crown, and cylinder walls and also to the exhaust valve, seat, valve guide, and port during the exhaust stroke. This heat is wasted except during cold weather when it is used to warm the passenger compartment. This heat loss is referred to as the "thermal load to the coolant" or the "heat rejection".

The engine operates at stable temperatures only when the heat rejection matches the heat input from the combustion gas. A major objective of the coolant system, irrespective of engine operating and ambient conditions, is to maintain the temperature of the engine within predetermined limits. This requires (1) the coolant temperature rise through the engine, from inlet to outlet, does not exceed 12 to 13 ^{o}F, (2) enough coolant flows through the engine water jackets within the engine to maintain acceptable coolant/metal temperatures and avoid localized boiling, and (3) the temperature of the coolant be controlled within a specific operating range, generally 195 to 205 ^{o}F, with infrequent excursions up to 230 to 245 ^{o}F allowed [22].

5.2 Components and Circuits of an Engine Coolant System

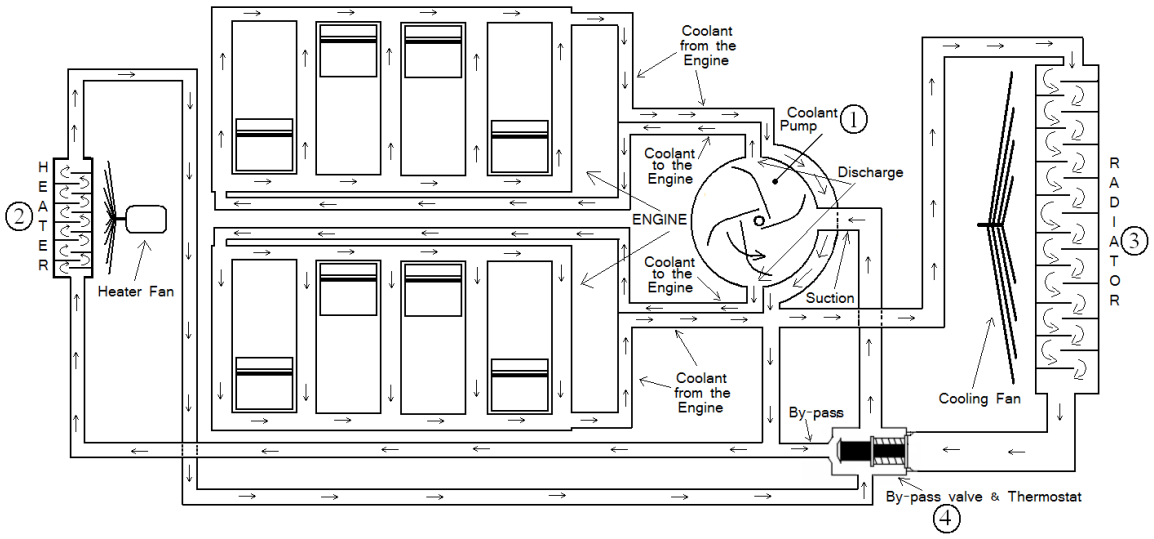

Figure 5.1: Physical layout of the engine coolant system.

In the following, functions and features of different coolant system components and circuits are discussed. Figure(5.1) shows the layout of a typical engine coolant system consisting of (1) Coolant pump, (2) Heater core, (3) Radiator, and (4) By-pass valve and thermostat.

The coolant pump imparts the coolant with the pressure head that drives the coolant through the system. Centrifugal pumps are preferred over positive displacement pumps because automotive water pumps must operate under a wide range of conditions, from high speed operation with low flow rates to producing high coolant flow rates necessary to cool the engine under the most severe conditions [22]. In a centrifugal pump, the fluid enters the pump at the center of the impeller assembly, figure (5.2). The rotation of the impeller accelerates the coolant centrifugally along the blades, converting the mechanical energy driving the pump into coolant velocity

and pressure. They have relatively low efficiencies, in the 20% range, with a few approaching 40%, but avoid excessively high pressure while operating at high speeds with low flow rates [22].

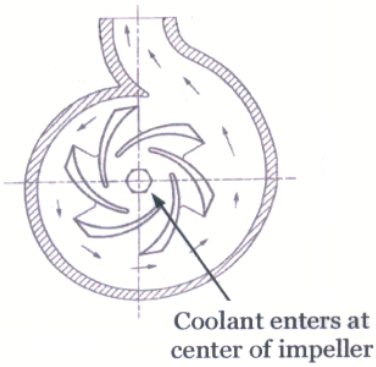

Figure 5.2: Pump casing and impeller.

The heater core is used to warm the passenger compartment of the automobile. It consists of tubes and fins and has the same basic design similar to that of the engine radiator. The thermal output from the heater can be regulated using coolant-side or air-side control strategies.

The radiator consists of a heat exchanger core, designed to dissipate the heat which the coolant has absorbed from the engine to the atmosphere, so that the engine operates at stable temperatures. The coolant flow through the radiator is controlled by the thermostat.

The thermostat is primarily responsible for maintaining the coolant temperature, engine temperature, and heat balance with in the predetermined limits and managing the flow within the system for a wide range of weather conditions and engine speed/load combinations. Figure (5.3) shows a sectional view of a thermostat. The critical element within the thermostat is the wax motor acting as a control element. Wax expands on the order of 13 to 15 % when heated to its melting point temperature [22]. This expansion due to solid to liquid phase change is used to turn heat energy,

contained in the hot coolant from the engine, into mechanical energy, causing the sliding of the stem or piston that displaces the valve off its seat. Once the coolant regains its stable operating temperature, the wax element cools down and solidifies. The piston is displaced back to its initial position by the force of the spring, closing the valve and consequently shutting down the flow through the radiator. Thermostats are designed so that, in its closed position, the valve rests on its seat. Thus avoiding the force of the spring being supported by the wax and reducing the potential for wax leakage. Thermostat waxes are formulated so as to have predetermined temperature set points for opening and closing its valve, governed by factors such as engine operating temperature, flow rates, and radiator capacity.

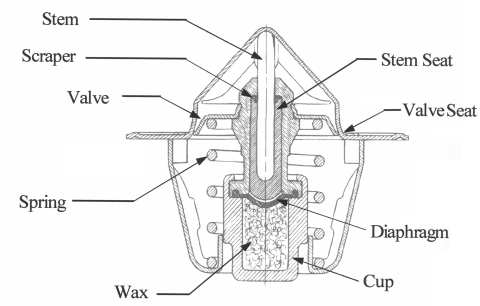

Figure 5.3: Elements of a typical thermostat valve.

A certain amount of coolant flow through the engine water jackets is required to promote proper temperature distribution and avoid hot spots. This is particularly critical with a closed or partially closed thermostat, such as after cold start or driving in very cold weather conditions. This flow is achieved with the thermostat and the by-pass. The by-pass has two variants, fixed or variable. The fixed by-pass circuit merely recirculates coolant and does not produce a temperature change except for heat transfer to and from castings. In some cases the by-pass flow is completely controlled by the heater circuit during which the by-pass avoids major changes in heater flow as thermostat valve opens/closes. This constant heater flow at various engine load

and speed conditions is achieved by a spring loaded by-pass valve that operates independent of the thermostat valve and is controlled by the system pressure [23]. In contrast the variable by-pass uses compound thermostat to shut off the radiator circuit when the coolant is below operating temperature, and progressively open the radiator circuit while it closes the by-pass as the coolant temperature increases and the need for cooling develops.

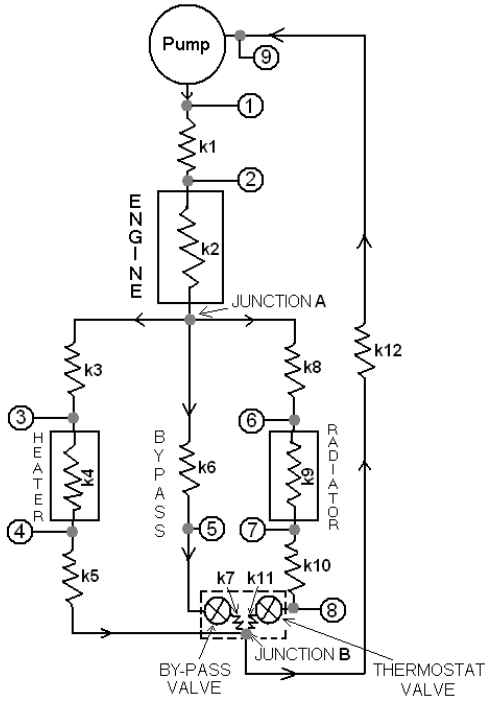

Figure 5.4: Coolant system circuit schematic.

Figure (5.4) shows a schematic of an engine coolant system. All of the flow passes through the pump and the engine, and then branches into three parallel circuits: the heater, the by-pass, and the radiator.

The heater circuit consists of a hose connected from the outlet of the engine water jackets, the heater core, and a return hose located with in the suction side of the pump. The coolant flow rate through the heater circuit is governed by the resistance of its circuit and the pressure differential across its inlet and outlet. The resistance is essentially fixed, defined by the diameter and length of the hoses, fittings, bends and the heater assembly. The flow rate in the heater circuit is usually on the order of 6 gpm [22]. Its maximum is usually (7 to 9) gpm, to avoid noise, liquid erosion and reduced fatigue life [22]. The temperature of the coolant flowing through the heater circuit does not change significantly except during cold weather conditions. In such conditions heat is rejected from the coolant to the air to warm the passenger compartment. Otherwise, the coolant returns to the pump inlet at essentially the same temperature.

The resistance to flow in the by-pass circuit is governed by the depth of the by-pass valve opening which is in turn a function of the overall system pressure [23]. The by-pass flow rates can be substantial for some engines, approaching 50% of the radiator flow even with a full open thermostat [22].

The resistance to flow in the radiator circuit changes with the thermostat valve opening. Below "the start to open" temperature, the flow through the radiator circuit is essentially zero. During normal driving and cold weather conditions, low heat rejection rates suffice to achieve steady operating temperatures. Whereas under more severe driving conditions the thermostat valve opens to its full stroke, minimizing the restriction to the coolant flow.

5.3 Modeling

A one-dimensional coolant system model based on the experimental data provided by the General Motors for a 1999 GMC Sierra has been developed. Given the engine speed of the vehicle the model predicts (1) the pressure drop and the flow rates through different components of the system and (2) the percent change in flow rates through different components of the system and additional coolant pumping power consumed due to the addition of the TEG circuit.

The coolant system model is based on the experimental testing performed by GM. This testing was done to perform a comparative study of the performance characteristics of its new coolant system to the existing base-line system. Wahler was the name given by GM to the new coolant system, therefore we designated the new coolant system as the Wahler coolant system (WCS). The only new variant in the WCS is a modified by-pass valve. Tests corresponding to closed and open thermostat conditions for the WCS and the base-line cases were performed. Therefore a total of four different tests were performed. Data from all the four tests were used in developing the coolant system model in order to verify the repeatability of the measured variables and to derive maximum possible information from the experimental testing. Pressure and flow rate measurements from various locations of the coolant system at different engine speeds were recorded during the tests. Using this data the loss coefficient of various components of the coolant system can be calculated. During these tests pressure and flow rate measurements at some of the locations were not recorded. Therefore the evaluation of the loss coefficients corresponding to the missing data was performed under certain assumptions with the existing data. The methodology and the assumptions adopted in evaluating these loss coefficients will be discussed in the next section.

5.3.1 Loss-coefficient of a Typical Flow System

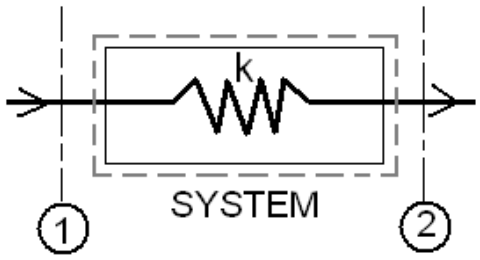

Figure 5.5: Flow through a system from node (1) to node (2), having a loss coefficient k.

Consider a system with a single resistance as shown in figure (5.5). The mechanical energy equation between the nodes (1) and (2) is defined as [24]:

$$p_1 + \frac{1}{2}\rho u_1^2 + \rho g Z_1 \;=\; p_2 + \frac{1}{2}\rho u_2^2 + \rho g Z_2 + h - W_{shaft} \tag{5.1}$$

where p is the pressure at a given node, ρ is the density of the fluid, u is the velocity at a given node, g is the acceleration due to gravity, Z is the elevation of a node above some horizontal reference plane, h is the total head loss, W_{shaft} is the work done on the system by an external device, and the subscripts 1 and 2 correspond to the node-(1) and the node-(2). Assuming nodes (1) and (2) are at the same elevation above some horizontal reference plane and as there is no external work being done on the system ($W_{shaft} = 0$), the total head loss using equation (5.1) can be defined as:

$$h \;=\; \triangle p + \frac{1}{2}\rho \triangle u^2. \tag{5.2}$$

In the experimental testing performed by the GM coolant flow rate was not measured at some of the locations in the coolant system, therefore we assume that the coolant flow inlet and outlet in each of the coolant system components was equally sized. Therefore u is constant throughout the system and the term $(\frac{1}{2}\rho\triangle u^2)$ in equation (5.2) is zero and the total head loss between nodes (1) and (2) using equation (5.2) can be redefined as:

$$h \;=\; \triangle p. \tag{5.3}$$

Therefore the total head loss across the nodes (1) and (2) of the system shown in figure (5.5) is equal to the total pressure drop across the nodes (1) and (2). The functional dependence of the total pressure drop across a system, can be expressed as [24]:

$$\triangle p \;=\; \Phi(L, D, u, \rho, \nu) \tag{5.4}$$

where L is the horizontal length of the system, D is the hydraulic diameter of the system, and ν is the kinematic viscosity. Non-dimensionalizing the different variables in equation (5.4), the resulting expression can be written as:

$$\frac{\triangle p}{\frac{1}{2}\rho u^2} \;=\; \Phi(\frac{Du}{\nu}, \frac{L}{D}, 1, 1, 1) \tag{5.5}$$

where the pressure drop is non-dimensionalized using dynamic pressure. Assuming $\triangle p$ has a linear dependence on $(\frac{L}{D})$, equation (5.5) can be expressed as:

$$\triangle p \;=\; \frac{1}{2}\rho u^2 \frac{L}{D} f(Re) \tag{5.6}$$

where Re is the Reynolds number. The velocity u in equation (5.6) is the ratio of the volumetric flow rate Q through and cross sectional area ($A = \frac{\pi}{4}D^2$) of the system as defined in equation (5.7):

$$u = \frac{Q}{A}. \tag{5.7}$$

From equations (5.6) and (5.7) the $\triangle p$ in equation (5.6) can be redefined as:

$$\triangle p \;=\; \frac{1}{2}\rho\frac{1}{A^2}\frac{L}{D}f(Re)Q^2. \tag{5.8}$$

If the density of the fluid does not vary, the ratio $(\frac{L}{D})$ and the cross-sectional area of the system are constant, then the term $\{\frac{1}{2}\rho\frac{1}{A^2}(\frac{L}{D})\}$ is a constant, say k_1. Let $f(Re) = k_2$, then the product $k_1k_2 = k$ is a function of Reynolds number and equation (5.8) can be expressed as:

$$\triangle p \;=\; kQ^2 \tag{5.9}$$

where, k is a loss coefficient of the system. Given experimental values of the pressure drop and flow rates, the loss coefficient of the system as a function of Reynolds number can be calculated. The Reynolds number for an internal flow is defined as [24]:

$$Re \;=\; \frac{uD}{\nu}. \tag{5.10}$$

From equations (5.7) and (5.10) the product of the terms Re and D can be defined as:

$$ReD \;=\; \frac{Q}{\frac{\pi}{4}\nu}. \tag{5.11}$$

Some of the dimensions of the coolant system components were not known. Therefore the dependency of the loss coefficients on the product of Re and D was adopted contrary to the conventional practice of Re. Also, for a given specific system if D is constant then the variation of the loss coefficient of the system under consideration as a function of the product of Re and D is only an offset on the scale of Re by the product ReD.

5.3.2 Evaluation of Loss Coefficients

The data necessary to evaluate the loss coefficients of various components associated with the engine, heater, by-pass, and radiator circuits are listed in table (5.1). The location of these loss coefficients and the pressure measurements used in evaluating them are shown in figure (5.4).

Estimation of ReD

The kinematic viscosity of a fluid ν is defined as:

$$\nu = \frac{\mu}{\rho}. \tag{5.12}$$

From equations (5.11) and (5.12) ReD can be redefined as:

$$ReD = \frac{\rho Q}{\frac{\pi}{4}\mu}. \tag{5.13}$$

Circuit	Loss coefficient	System description	Measured variables required to evaluate the loss coefficient					
			Flow Q	Measurement performed	Inlet pressure location	Measurement performed	Outlet pressure location	Measurement performed
Engine	k_1	Path from the pump outlet to the engine inlet	Total flow	Yes	(1)	Yes	(2)	Yes
	k_2	Engine water jackets from the engine inlet to junction A	Total flow	Yes	(2)	Yes	Junction A	Yes
Heater	k_3	Path from the junction A to the inlet of the heater core	Heater flow	Yes	Junction A	No	(3)	Yes
	k_4	Heater core	Heater flow	Yes	(3)	Yes	(4)	Yes
	k_5	Return path from the outlet of the heater core to the junction B	Heater flow	Yes	(4)	Yes	Junction B	Yes
By-pass	k_6	Path from the junction A to the inlet of by-pass valve	By-pass flow	No	Junction A	No	(5)	Yes
	k_7	By-pass valve	By-pass flow	No	(5)	Yes	Junction B	No
Radiator	k_8	Path from the junction A to inlet of the radiator	By-pass flow	No	Junction A	No	(6)	Yes
	k_9	Radiator unit	Radiator flow	Yes	(6)	Yes	(7)	Yes
	k_{10}	Return path from the radiator outlet to the inlet of thermostat valve	Radiator flow	Yes	(7)	Yes	(8)	Yes
	k_{11}	Thermostat valve	Radiator flow	Yes	(8)	Yes	Junction B	No
	k_{12}	Path from the junction B to the inlet of the coolant pump	Total flow	Yes	Junction B	No	9	Yes

Table 5.1: Various loss coefficients with the system description and the measured variables necessary to evaluate them.

At a given engine speed S, the temperature of the coolant, T_s and the volumetric flow rate, Q_s through the system at the speed S are obtained from the experimental data provided by the GM. The density, ρ_s and the dynamic viscosity, μ_s corresponding to T_s are obtained from the properties for aqueous Prestone antifreeze coolant solutions. Thus ReD is evaluated using equation (5.13).

For the majority of the elements within the coolant system ,all the four data sets: base-line open thermostat condition (BOTC), WCS open thermostat condition (WOTC), base-line closed thermostat condition (BCTC), and WCS closed thermostat condition (WCTC) were used in relating the variation of loss coefficient and ReD. Once the data pertaining to the evaluation of loss coefficient from the four data sets was established, a power law was defined for the entire data set of the specific system to relate the variation of its loss coefficient with respect to ReD. For the by-pass valve, the loss coefficient has to be defined independently for each of the open and closed thermostat conditions because of the changing geometry. For the complete radiator circuit, the loss coefficient has been defined only for the open thermostat condition as there is essentially no flow through it in the closed thermostat condition, which acts as an infinite resistance. For most of the elements of the coolant system, there were discrepancies in the data set at lower engine speeds giving spikes in the values of loss coefficient. Therefore loss coefficients corresponding to the lower engine speeds were not considered in establishing the power law. Any further references about the location of the loss coefficients or measured variables are with respect to figure (5.4).

k_1 represents the loss coefficient of the path from the pump outlet to the engine inlet. $\triangle p$ and Q required to evaluate k_1 are obtained from the pump outlet pressure-location (1), engine inlet pressure-location (2), and the total flow rate.

$$k_1 = \frac{p_{pumpoutlet} - p_{engineinlet}}{Q^2_{total}} \tag{5.14}$$

The data used in establishing the relationship between k_1 and ReD and the curve fit to the data are shown in figure (5.6).

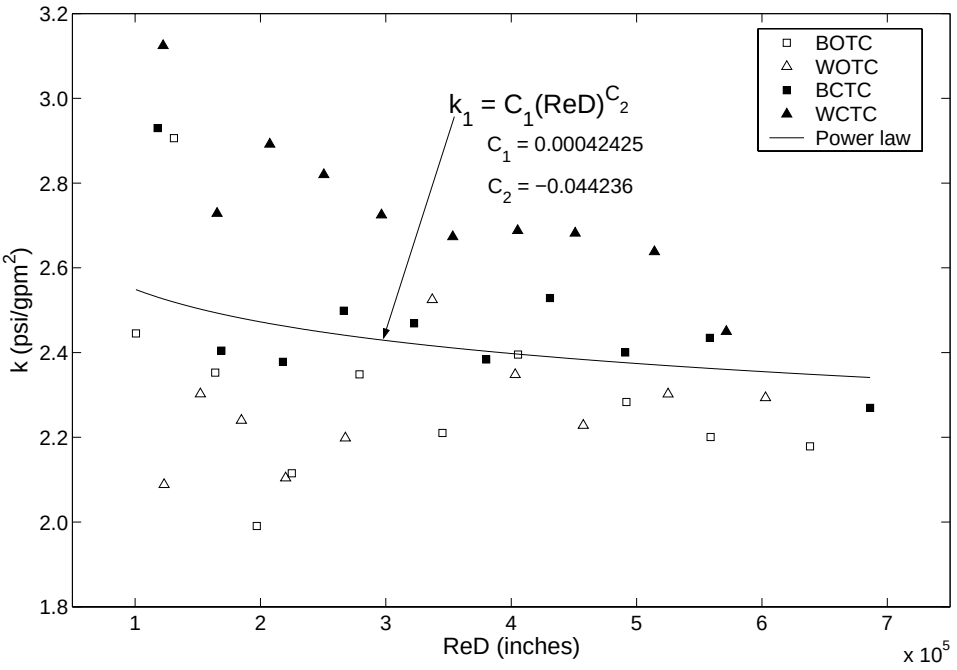

Figure 5.6: Variation of loss coefficient as a function of ReD for path to engine model.

k_2 represents the loss coefficient of the engine. $\triangle p$ and Q required to evaluate k_2 are obtained from the engine inlet pressure-location (2), engine outlet pressure-junction A, and the total flow rate. Engine outlet pressure was not a measured variable in the GM experimental data. Therefore highest system pressure after junction A was used as the engine outlet pressure. The highest system pressure was at the inlet of the by-pass valve-location (5) for the open thermostat condition and the inlet of the radiator-location (6) for closed thermostat condition. The pressure at junction A for the open thermostat condition has been modified using the pressure at location (5) and k_6, as shown in equation (5.15). k_6 has been obtained from the closed thermostat condition data. The evaluation of k_6 will be discussed later.

$$p_{engineoutlet} = k_6 Q^2_{bypass} + p_{location(6)} \tag{5.15}$$

$$k_2 = \frac{p_{engineinlet} - p_{engineoutlet}}{Q^2_{total}} \tag{5.16}$$

The data used in establishing the relationship between k_2 and ReD and the curve fit to the data are shown in figure (5.7).

The loss coefficient k_3 represents the path from the junction A to the inlet of the heater core. $\triangle p$ and Q required to evaluate k_3 are obtained from the pressure at junction A, the heater inlet pressure-location (4), and the heater flow rate. Pressure at junction A is evaluated as discussed in k_2.

$$k_3 = \frac{p_{engineoutlet} - p_{heaterinlet}}{Q^2_{heater}} \tag{5.17}$$

For systems without any moving parts the loss coefficient of the system should decrease with an increase in Reynolds number, whereas k_3 increases with an increase in ReD for closed thermostat data set, shown in figure (5.8). Therefore only open

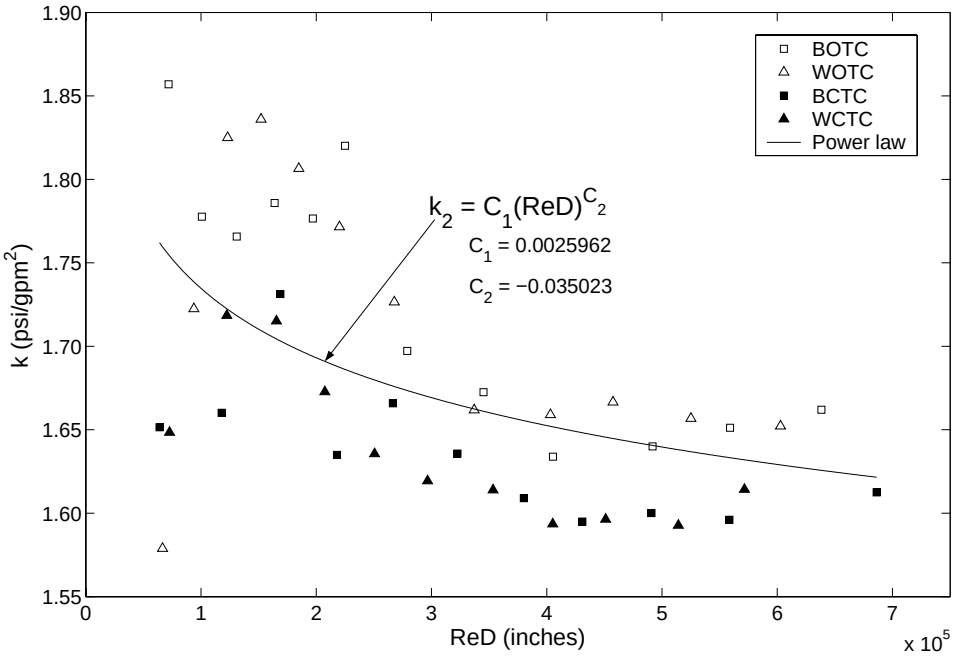

Figure 5.7: Variation of loss coefficient as a function of ReD for engine model.

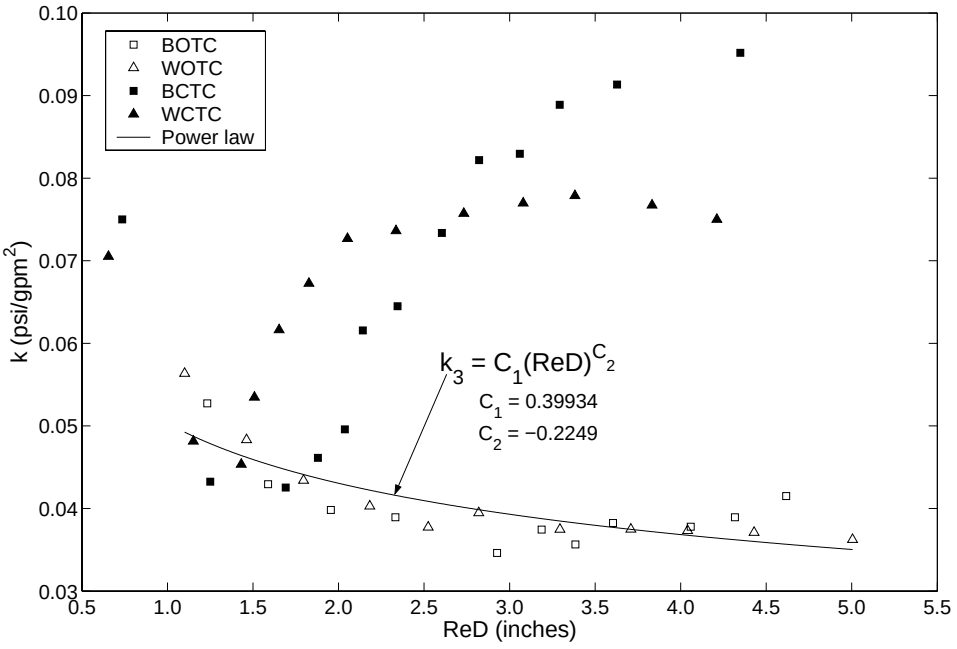

Figure 5.8: Variation of loss coefficient as a function of ReD for path to heater model.

thermostat data set has been used in evaluating k_3 as a function of ReD. The data used in establishing the relationship between k_3 and ReD and the curve fit to the data are shown in figure (5.8). The increase in loss coefficient of k_3 with respect to ReD under closed thermostat condition (CTC) and the uneven spread of the data in open thermostat condition (OTC) is due to the assumption that ($u = constant$) at both the inlet and outlet of the path to heater component was not a good approximation.

k_4 represents the loss coefficient of the heater core. $\triangle p$ and Q required to evaluate k_4 are obtained from the heater inlet pressure-location (3), the heater outlet pressure-location (4), and the heater flow rate.

$$k_4 \;=\; \frac{p_{heaterinlet} - p_{heateroutlet}}{Q^2_{heater}} \tag{5.18}$$

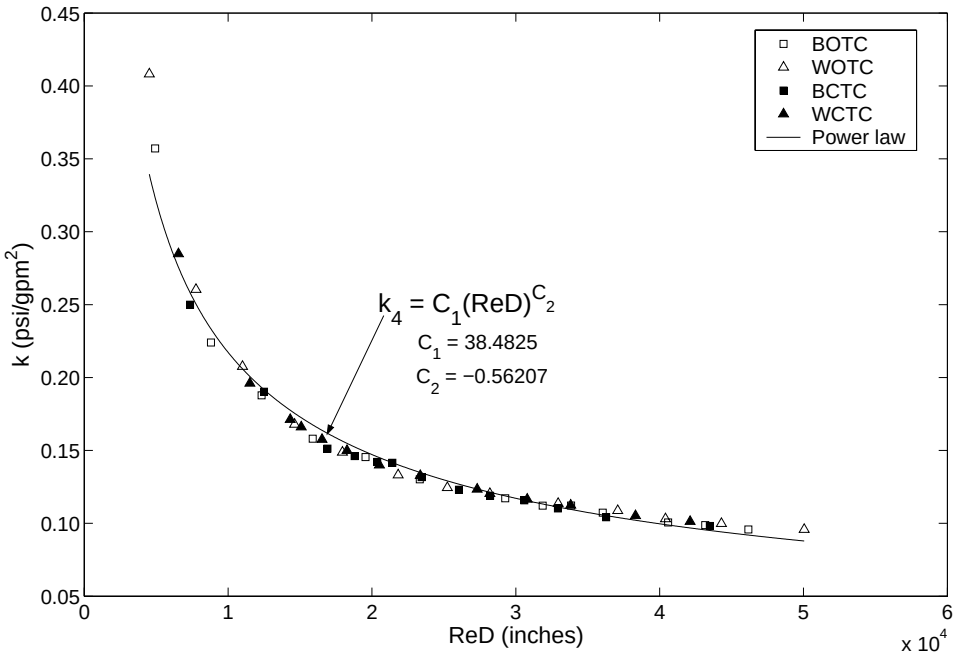

Figure 5.9: Variation of loss coefficient as a function of ReD for heater model.

The data used in establishing the relationship between k_4 and ReD and the curve fit to the data are shown in figure (5.9). The good collapse of the data is because the inlet and outlet velocities of the heater core are equal and therefore the assumption that ($u = constant$) was a good approximation.

k_5 represents the loss coefficient of the return path from the outlet of the heater core to junction B. $\triangle p$ and Q required to evaluate k_5 are obtained from the heater outlet pressure-location (4), the pressure at junction B, and the heater flow rate. Pressure at junction B was not a measured variable. Therefore the pump inlet pressure-location (9) has been used for the pressure at junction B.

$$k_5 = \frac{p_{heateroutlet} - p_{pumpinlet}}{Q^2_{heater}} \tag{5.19}$$

Although junction B and location (9) seem to be far apart in the schematic, figure (1.5), they are in fact quite close in the physical layout of the system, figures (5.1) and (5.10). Figure (5.10) shows the pump housing for the coolant system shown in figure (5.1). The pump housing includes the impeller, the by-pass, the by-pass and the thermostat valves, and the coolant flow passage ways to and from the engine, heater and the radiator. The coolant flow from the two cylinder heads enters into the pump housing. Then if the thermostat is opened it branches into the radiator circuit, the heater circuit, and the by-pass circuit. The return flow from the radiator through the thermostat and the heater combines with the flow from the by-pass at the location of the thermostat and by-pass valves, junction B. The combined flow from the by-pass, heater, and the radiator at junction B flows back to the suction side of the impeller, location (9). Therefore the assumption that pressure at junction B is roughly equivalent to pressure at location (9) is a reasonable approximation.

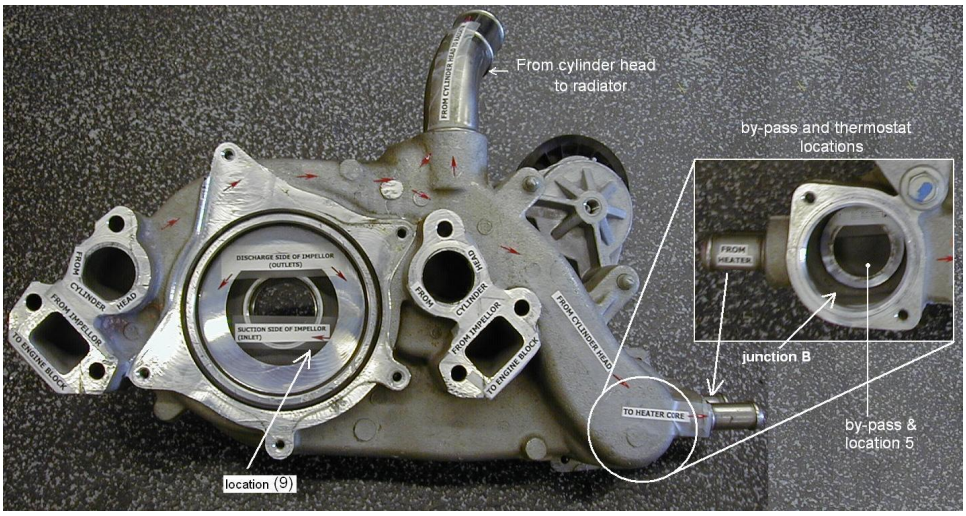

Figure 5.10: Coolant pump housing and location of the by-pass and thermostat valves.

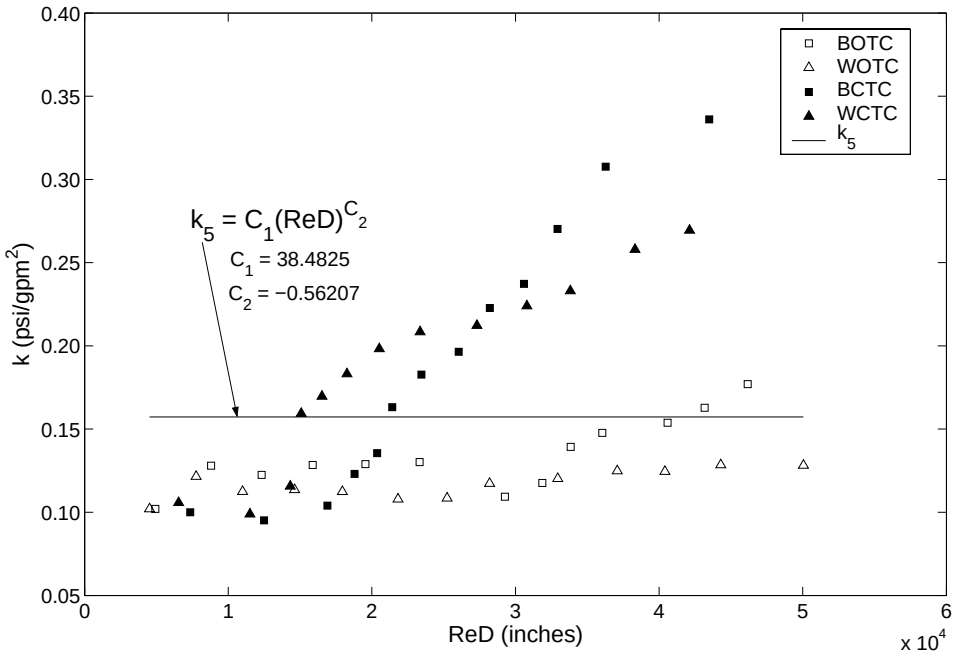

Figure 5.11: Variation of loss coefficient as a function of ReD for path from heater model.

From figure (5.11), for both open thermostat and closed thermostat conditions the trend in the data shows an increase in loss coefficient with respect to an increase in ReD. Therefore a constant value of $k_5 = 0.1573(\frac{psi}{gpm^2})$ was used.

k_6 represents the loss coefficient of the by-pass. $\triangle p$ and Q required to evaluate k_6 are obtained from the pressure at junction A, the by-pass valve inlet pressure-location (5) and the by-pass flow rate. The pressure at junction A and by-pass flow rate are not measured variables. The pressure at junction A is evaluated as discussed in k_2. Estimation of k_6 for OTC is not possible because we are trying to use location (5) as both the higher and lower pressure point. Therefore estimation of k_6 using difference of pressure between location (6) and location (5) from the closed thermostat data set was used for both the open and closed thermostat conditions. The by-pass flow rate has been estimated using equation (5.21).

$$k_6 = \frac{p_{engineoutlet} - p_{bypassinlet}}{Q^2_{bypass}} \tag{5.20}$$

$$Q_{bypass} = Q_{total} - (Q_{heater} + Q_{radiator}) \tag{5.21}$$

The data used in establishing the relationship between k_6 and ReD and the curve fit to the data are shown in figure (5.12). The trend shows an increase in loss coefficient of k_6 corresponding to an increase in ReD, therefore a constant value of $k_6 = 4.2235 \times 10^{-5}(\frac{psi}{gpm^2})$, mean of the closed thermostat data set has been adopted.

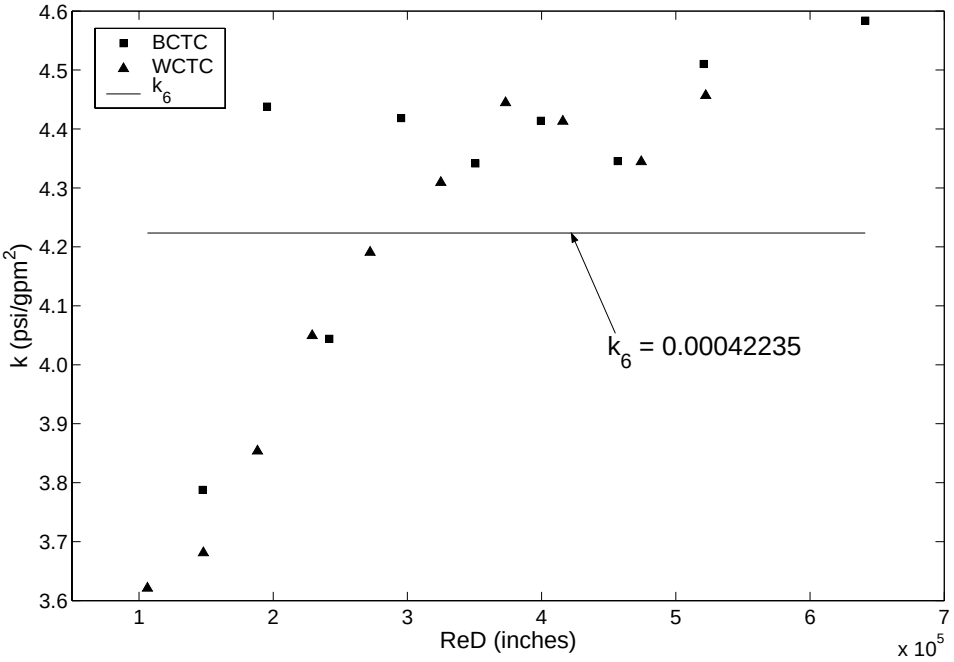

Figure 5.12: Variation of loss coefficient as a function of ReD for by-pass model.

k_7 represents the loss coefficient of the by-pass valve. Due to the functional operation of the by-pass valve, k_7 has to be defined independently for the OTC and the CTC. $\triangle p$ and Q required to evaluate k_7 are obtained from the by-pass valve inlet pressure-location (5), the pressure at junction B, and the by-pass flow rate. Pressure at junction B is not a measured variable and from the discussion of k_5 pressure at junction B is equivalent to pump inlet pressure-location (9). The by-pass flow rate is calculated using equation (5.21).

$$k_7 = \frac{p_{bypassinlet} - p_{pumpinlet}}{Q^2_{bypass}} \tag{5.22}$$

The data used in establishing the relationship between k_7 and ReD and the curve fit to the data for the open and closed thermostat conditions are shown in figures (5.13) and (5.14) respectively.

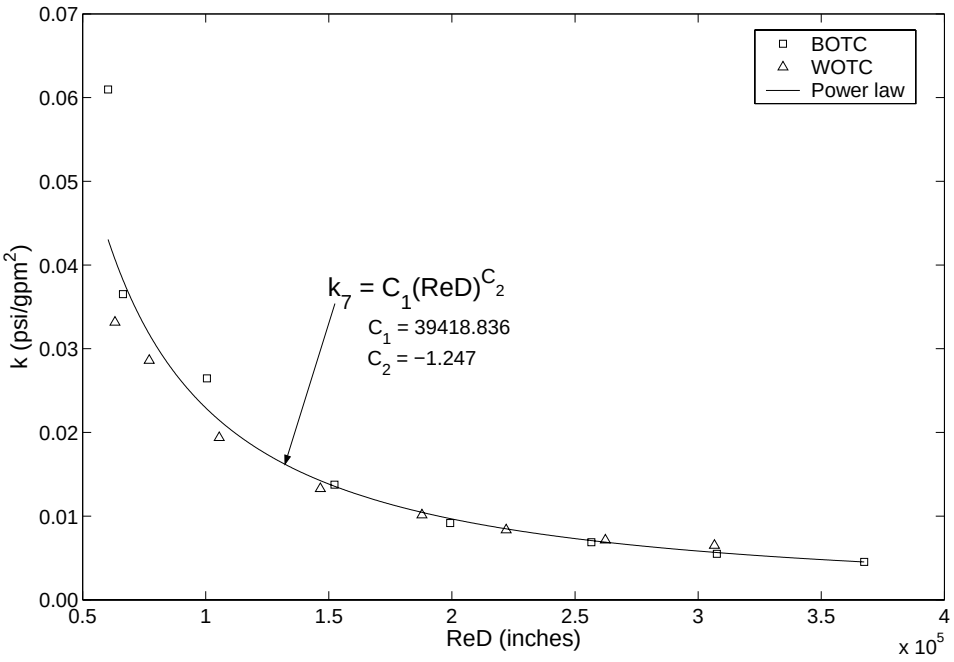

Figure 5.13: Variation of loss coefficient as a function of ReD for by-pass valve model under OTC.

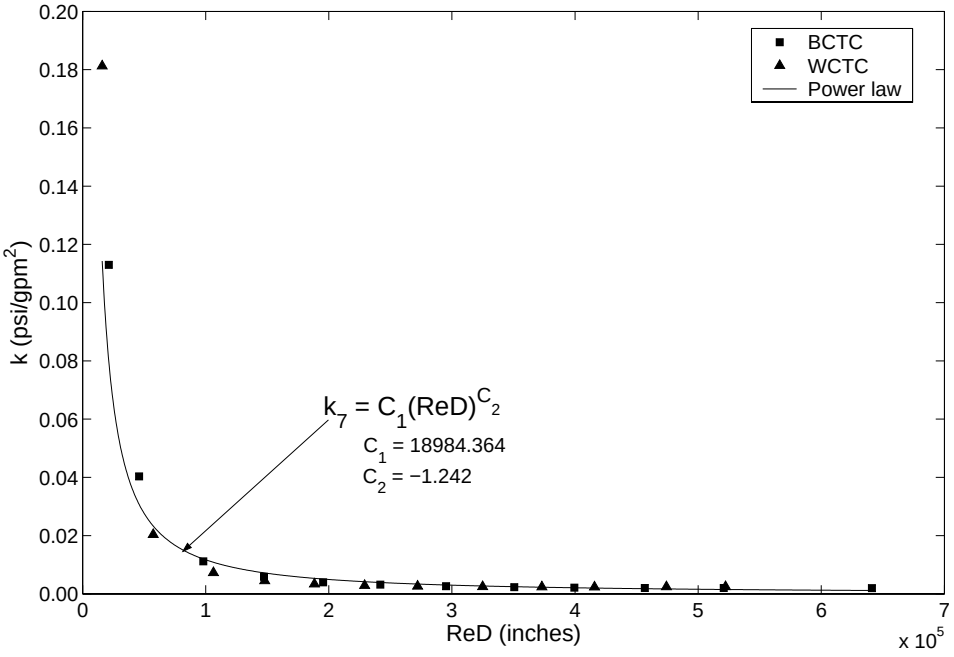

Figure 5.14: Variation of loss coefficient as a function of ReD for by-pass valve model under CTC.

The resistance of the radiator circuit for closed thermostat condition is assumed to be infinite, as there is essentially zero flow during that condition. Therefore the evaluation of k_8, k_9, k_{10}, and k_{11} are performed for open thermostat data set only.

k_8 represents the loss coefficient of the path from junction A to inlet of the radiator. $\triangle p$ and Q required to evaluate k_8 are obtained from the pressure at junction A, the radiator inlet pressure-location (6), and the radiator flow rate. Pressure at junction A is calculated as discussed in k_2.

$$k_8 = \frac{p_{engineoutlet} - p_{radiatorinlet}}{Q^2_{radiator}} \tag{5.23}$$

The data used in establishing the relationship between k_8 and ReD and the curve fit to the data are shown in figure (5.15).

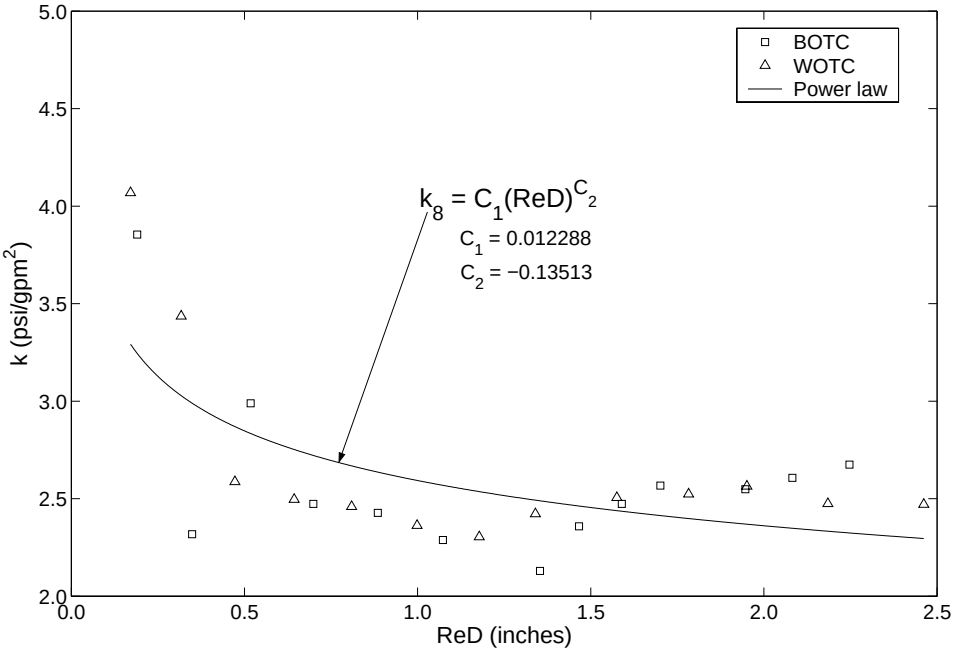

Figure 5.15: Variation of loss coefficient as a function of ReD for path to radiator model.

k_9 represents the loss coefficient of the radiator. $\triangle p$ and Q required to evaluate k_9 are obtained from the radiator inlet pressure-location (6), the radiator outlet pressure-location (7), and the radiator flow rate.

$$k_9 = \frac{p_{radiatorinlet} - p_{radiatoroutlet}}{Q^2_{radiator}} \tag{5.24}$$

The data used in establishing the relationship between k_9 and ReD and the curve fit to the data are shown in figure (5.16).

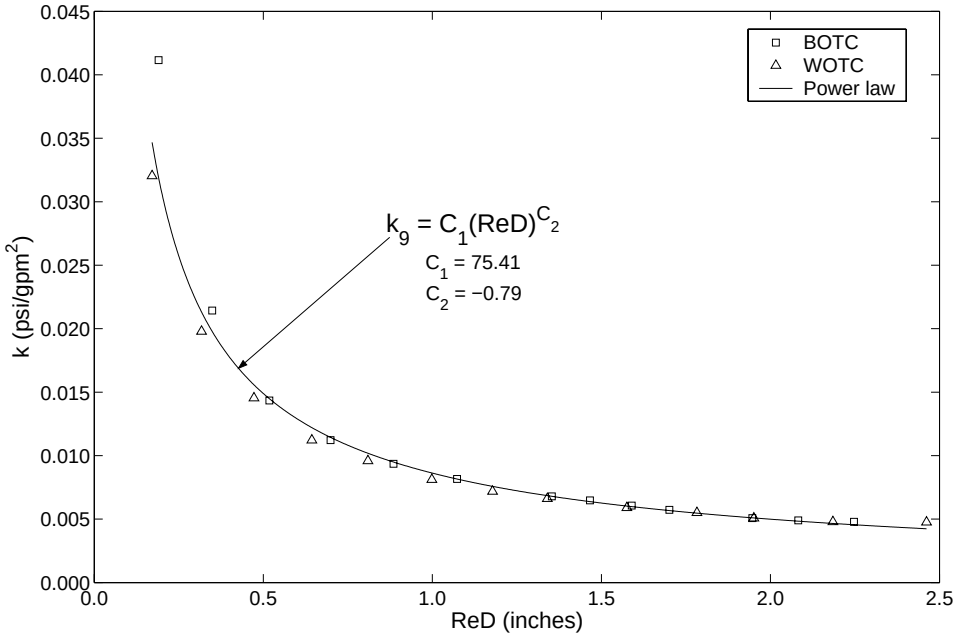

Figure 5.16: Variation of loss coefficient as a function of ReD for radiator model.

k_{10} represents the loss coefficient of the path from the radiator outlet to the inlet of the thermostat valve. $\triangle p$ and Q required to evaluate k_{10} are obtained from the radiator outlet pressure-location (7), the thermostat valve inlet pressure-location (8), and the radiator flow rate.

$$k_{10} = \frac{p_{radiatoroutlet} - p_{thermostatinlet}}{Q^2_{radiator}} \tag{5.25}$$

The data used in establishing the relationship between $k10$ and ReD and the curve fit to the data are shown in figure (5.17). The trend in the plot shows an increase in loss coefficient with respect to an increase in ReD, therefore a constant value of $k_{10} = 8.0615 \times 10^{-4}(\frac{psi}{gpm^2})$ has been adopted.

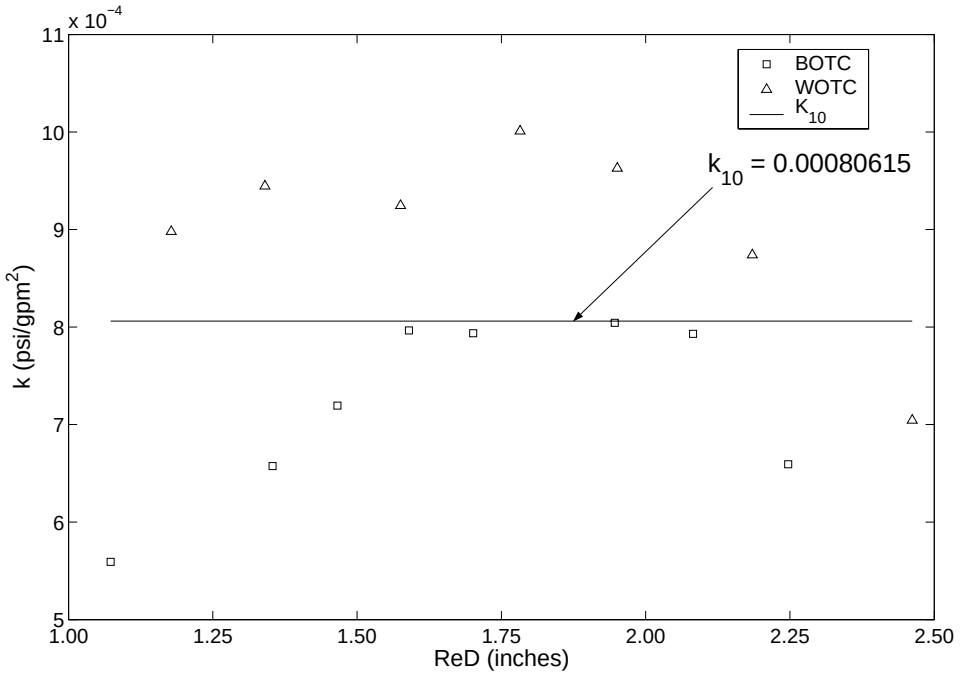

Figure 5.17: Variation of loss coefficient as a function of ReD for path from radiator model.

k_{11} represents the loss coefficient of the thermostat valve. $\triangle p$ and Q required to evaluate k_{11} are obtained from the thermostat valve inlet pressure-location (8), the pressure at junction B, and the radiator flow rate. The pump inlet pressure-location (9) is used as the pressure at junction B as discussed in k_5.

$$k_{11} = \frac{p_{thermostatinlet} - p_{pumpinlet}}{Q^2_{radiator}} \tag{5.26}$$

The data used in establishing the relationship between k_{11} and ReD and the curve fit to the data are shown in figure (5.18). The data in the plot is scattered and the trend shows an increase in loss coefficient with respect to an increase in ReD, therefore a constant value of $k_{11} = 0.0031(\frac{psi}{gpm^2})$ has been adopted.

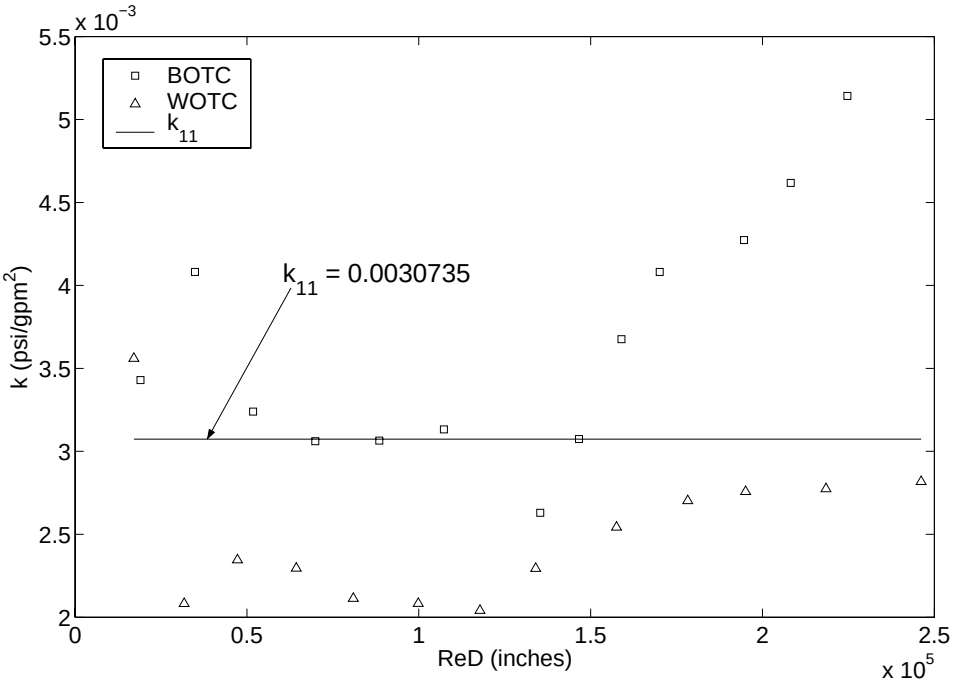

Figure 5.18: Variation of loss coefficient as a function of ReD for thermostat valve model.

k_{12} represents the loss coefficient of the path from junction B to the pump inlet. $\triangle p$ and Q required to evaluate k_{12} are obtained from the pressure at junction B, the pump inlet pressure-location (9), and the total flow rate. Pump inlet pressure-location (9) is used as pressure at junction B as discussed in k_5. Due to location (9) being both the higher and lower pressure points for evaluating $\triangle p$, estimation of k_{12} has been ruled out and assumed to be zero. Also, as discussed in the evaluation of k_7 both the locations, junction B and (9), are located within the pump housing and are not wide apart. Therefore the assumption ($k_{12} = 0$) is a reasonable approximation.

5.4 Coolant System Analysis

A coolant system analysis is performed based on the GM coolant system data and the established loss coefficient models of various coolant system components. The analysis consists of two different configurations: without and with the presence of the TEG circuit. Using the difference of flow rates for each of the coolant system component between the two different configurations, the percent change in flow rates because of the addition of the TEG circuit for that component can also be estimated. Also, the additional coolant pumping power due to the addition of the TEG circuit is calculated using the TEG flow rate and the pressure drop across the TEG circuit.

The following is the procedure to estimate the flow rates through different components of the coolant system for the configuration, without the presence of the TEG circuit. Given the thermostat condition and engine speed of the vehicle, we then iterate to find the flow rates. As a first guess for the iteration we use the corresponding total, heater, and radiator flow rates. The temperature of the coolant and the head generated by the coolant pump at the given engine speed and thermostat condition are obtained from the GM coolant system data. Using these flow rates and coolant

temperature, ReD and the corresponding loss coefficients for different components of the coolant system are calculated. Based on these loss coefficients, the total loss coefficient of the system is calculated using equation (5.27):

$$k_{tot} \;=\; k_{engC} + \{(k_{htrC})^{-\frac{1}{2}} + (k_{bpC})^{-\frac{1}{2}} + (k_{radC})^{-\frac{1}{2}}\}^{-2} \tag{5.27}$$

where k_{engC}, k_{htrC}, k_{bpC}, and k_{radC} are the total loss coefficients of the engine, heater, by-pass, and the radiator circuits respectively and defined by the equations (5.28), (5.29), (5.30), and (5.31).

$$k_{engC} \;=\; k_1 + k_2 \tag{5.28}$$

$$k_{htrC} \;=\; k_3 + k_4 + k_5 \tag{5.29}$$

$$k_{bpC} \;=\; k_6 + k_7 \tag{5.30}$$

$$\left.\begin{array}{l} \textit{Open thermostat condition} \\ k_{radC} \;=\; k_8 + k_9 + k_{10} + k_{11} \\ \textit{Closed thermostat condition} \\ k_{radC} \;=\; \infty \end{array}\right\} \tag{5.31}$$

Using the total loss coefficient and the head generated by the pump, the total flow rate is calculated from the equation (5.32).

$$Q_{tot-new} \;=\; \left(\frac{h_{pump}}{k_{tot}}\right)^{\frac{1}{2}} \tag{5.32}$$

Based on the loss coefficient of the engine circuit, equation (5.27), and the new total flow rate, equation (5.32), the pressure drop across the engine circuit is calculated using equation (5.33).

$$\triangle p_{engC} \;=\; k_{engC} \times Q^2_{tot-new} \tag{5.33}$$

Using the pressure drop across the engine circuit and the head generated by the pump, the head available to the heater, by-pass, and the radiator circuits is calculated from the equation (5.34).

$$h_{AB} \;=\; h_{pump} - \triangle p_{engC} \tag{5.34}$$

Based on the head available and the loss coefficients of the heater, by-pass, and the radiator circuits, the new flow rates through the heater, by-pass, and the radiator are calculated using equations (5.35), (5.36), and (5.37).

$$Q_{htr-new} \;=\; \left(\frac{h_{AB}}{k_{htrC}}\right)^{\frac{1}{2}} \tag{5.35}$$

$$Q_{bp-new} \;=\; \left(\frac{h_{AB}}{k_{bpC}}\right)^{\frac{1}{2}} \tag{5.36}$$

$$Q_{rad-new} \;=\; \left(\frac{h_{AB}}{k_{radC}}\right)^{\frac{1}{2}} \tag{5.37}$$

The above procedure is iterated with the head generated by the pump and the coolant temperature from the GM data remain unchanged through each iteration, while the flow rates through different components are updated with the new flow rates based on the loss coefficients from the previous iteration. The stopping criteria for the above iteration procedure is based on the difference between the flow rates from successive iterations, are below a predetermined tolerance limit.

In estimating the flow rates through different components of the coolant system for the configuration with the presence of TEG circuit, the procedure is almost the same to that of the configuration with out its presence. The only change that is necessary, because of the addition of the TEG circuit in parallel to the heater, by-pass, and the radiator circuits, is that of the estimation of total loss coefficient of the system. The equation (5.27), that is used in estimating the total loss coefficient of

the system for the configuration without the presence of the TEG, is replaced by the equation (5.38), where k_{tegC} is the total loss coefficient of the TEG circuit.

$$k_{tot} \;=\; k_{engC} + \{(k_{tegC})^{-\frac{1}{2}} + (k_{htrC})^{-\frac{1}{2}} + (k_{bpC})^{-\frac{1}{2}} + (k_{radC})^{-\frac{1}{2}}\}^{-2} \tag{5.38}$$

The TEG circuit consists of pre-coolant heat exchanger (PCHX), hoses, T-junctions, elbows and the two coolant heat exchangers. The hoses, T-junctions, and elbows are used in connecting the coolant heat exchangers across the coolant taps of the heater circuit, figure (5.19). The loss coefficient for the PCHX was calculated using the data from the experiments [25], the loss coefficient for the coolant heat exchanger [25] was estimated using correlations from [26] and [27], and the loss coefficients for the hoses, T-junctions, and elbows are calculated using correlations from [27].

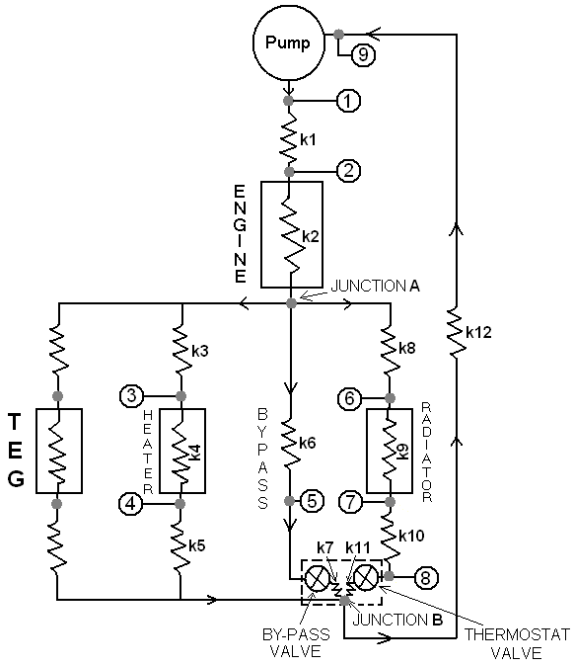

Figure 5.19: Coolant system circuit schematic with TEG circuit.

5.5 Validation of the Coolant System Model

In the following section validation for the total, heater, by-pass, and the radiator flow rates from the model, as a function of engine speed is discussed. A total of four configurations, with and without the presence of TEG under open and closed thermostat conditions were validated against GM coolant system data and AETEG testing at Delphi. For the case of AETEG testing at Delphi, only heater, radiator and TEG flow rates have been measured. Therefore comparison of coolant system model against AETEG testing at Delphi was performed for those specific components only. Also, the data from the Delphi testing was available only up to a maximum engine speed of 2000 rpm.

Figure (5.20) shows the validation for the total flow rate as a function of engine speed for open and closed thermostat conditions with no TEG. The baseline and NCS models are in agreement with the GM data for OTC. For the CTC the model under predicts between (1500 and 4000) rpm and over predicts between (4500 and 5500).

Validation for the heater flow is shown in figure (5.21). The model is in agreement with the GM data for OTC with no TEG where as it under predicts the data from the Delphi testing. For OTC with TEG the model is in agreement with the majority of the data from the Delphi testing. For CTC with no TEG the model is in agreement with the data from the Delphi testing and with GM data up to an engine speed of 2000 rpm, beyond this the model over predicts the GM data. For CTC with and with out the presence of TEG and at engine speeds beyond 5000 rpm the baseline model predictions tend to plateau rather than increasing with the increasing engine speed. The probable reason for the phenomena is due to the functioning of the by-pass valve. The by-pass valve in addition to allowing for the excess flow during the CTC, it also

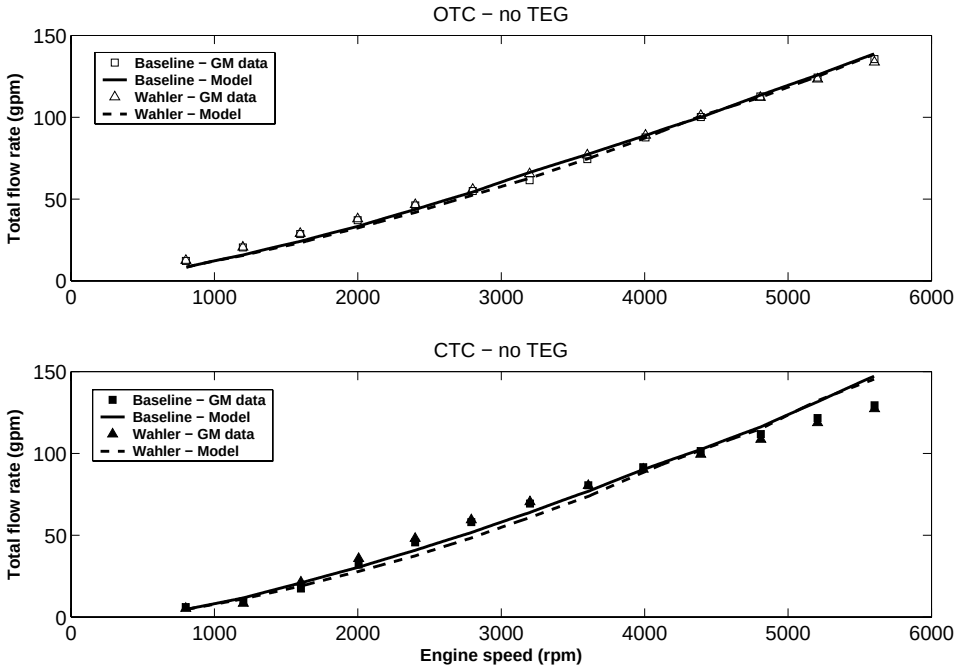

Figure 5.20: Coolant system model validation for the total flow.

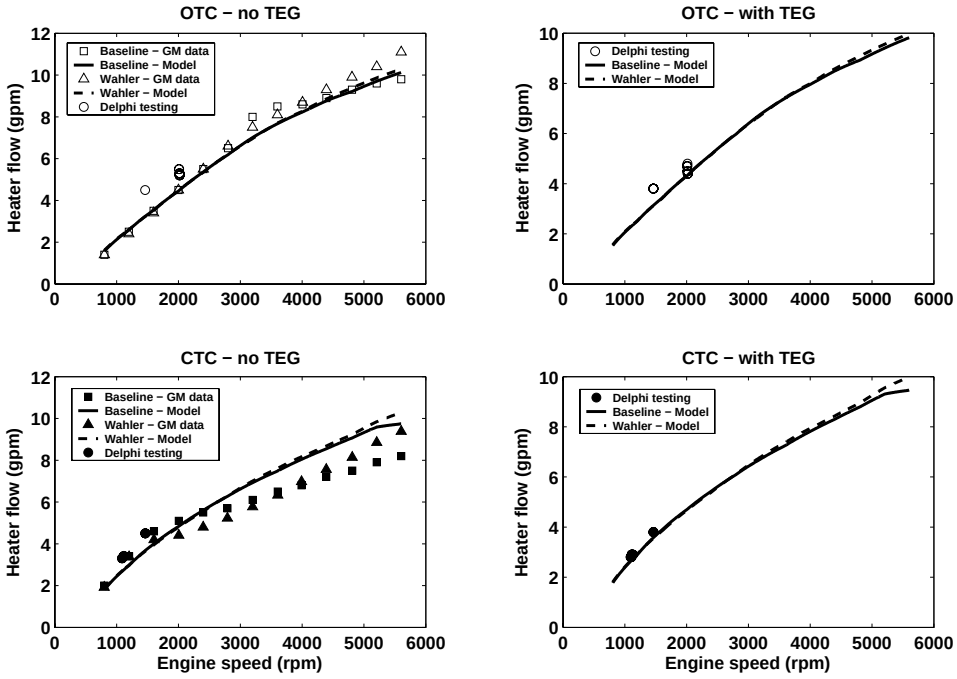

Figure 5.21: Coolant system model validation for the heater flow.

tries to maintain the head available to the heater circuit below a predetermined limit [23]. Thus even with increasing engine speed beyond 5000 rpm although the total available head increases, figure (5.22), the head available to the heater circuit remains constant and therefore the flow also remains constant.

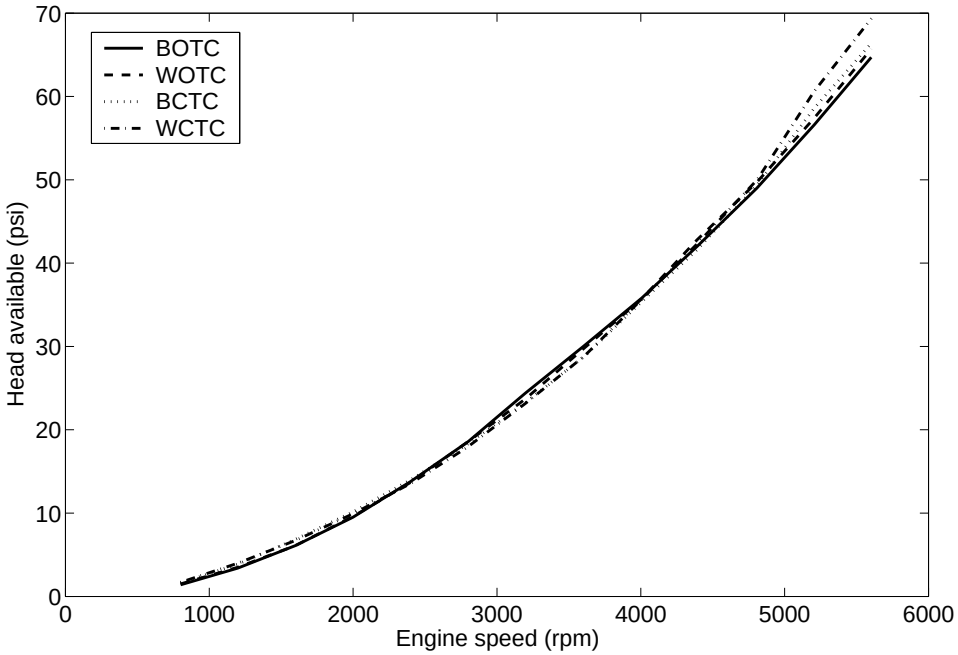

Figure 5.22: Total available head from the GM data.

The by-pass flow validation is shown in figure (5.23). For the OTC with no TEG the model agrees with the GM data, except at lower engine speeds from (900 to 2500) it under predicts and for the configuration CTC with no TEG the model under predicts at engine speeds from (2000 to 4000) rpm and over predicts at engine speeds beyond 4800 rpm.

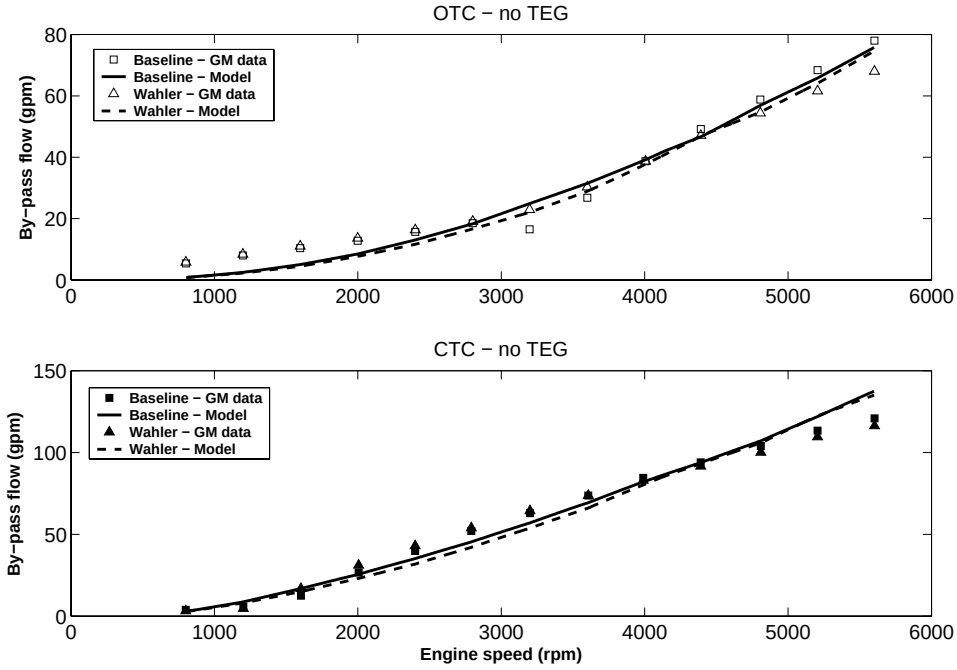

Figure 5.23: Coolant system model validation for the by-pass flow.

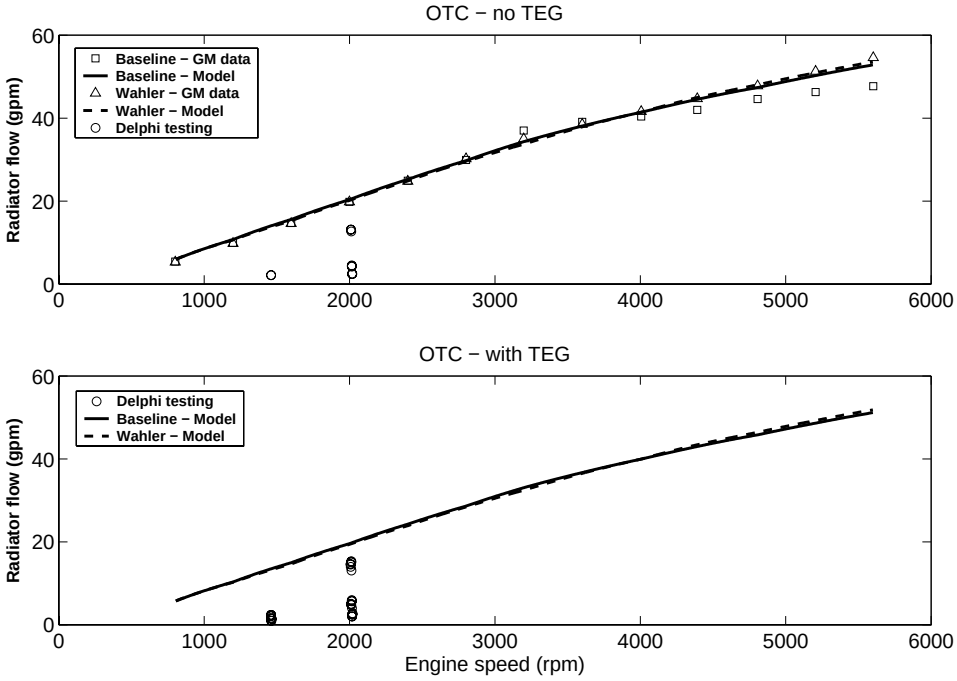

Figure 5.24: Coolant system model validation for the radiator flow.

Figure (5.24) shows the validation for the radiator flow. For the configuration OTC with no TEG the model agrees with the GM data up to engine speed of 4000 rpm, beyond this the model over predicts the data from the baseline case. The results from the Delphi testing shows that the radiator flow is not constant at a given engine speed and ranges from near zero to a value closer to the GM data and that of the model. The variation of the flow rate is due to the functioning of the thermostat valve. The opening and closing of the valve is controlled by the expansion and solidification of the wax, due to the rise and fall in coolant temperature. The heat rejection and rise in coolant temperature is a time dependent process thus the radiator flow is predominantly a function of engine operating time rather than engine speed as shown in figure (5.25). On the contrary results from the GM data show that the radiator flow is a function of engine speed. The GM data was recorded at 100% open thermostat condition [28]. The variation of radiator flow with respect to the engine speed in the GM data is due to the variation of head across the radiator circuit.

The TEG flow validation is shown in figure (5.26). The model over predicts the results from the Delphi testing. This is due to the incorrect loss coefficient of the TEG circuit in the model. Prior to the Delphi testing, the inlet and outlet valves at the location of the coolant taps across the heater circuit have been adjusted such that the TEG coolant circuit receives the optimum flow rate, about 2 to 3.5 gpm, there by reducing the additional load on the coolant pump. The effects of these valves and of their openings have not been accounted into the loss-coefficient of the TEG circuit. Therefore the model predicts higher flow rates compared to the Delphi testing. Based on the results from the Delphi testing, the loss-coefficient of the TEG circuit in the model can be adjusted, such that the model predicts close enough to the results from the Delphi testing.

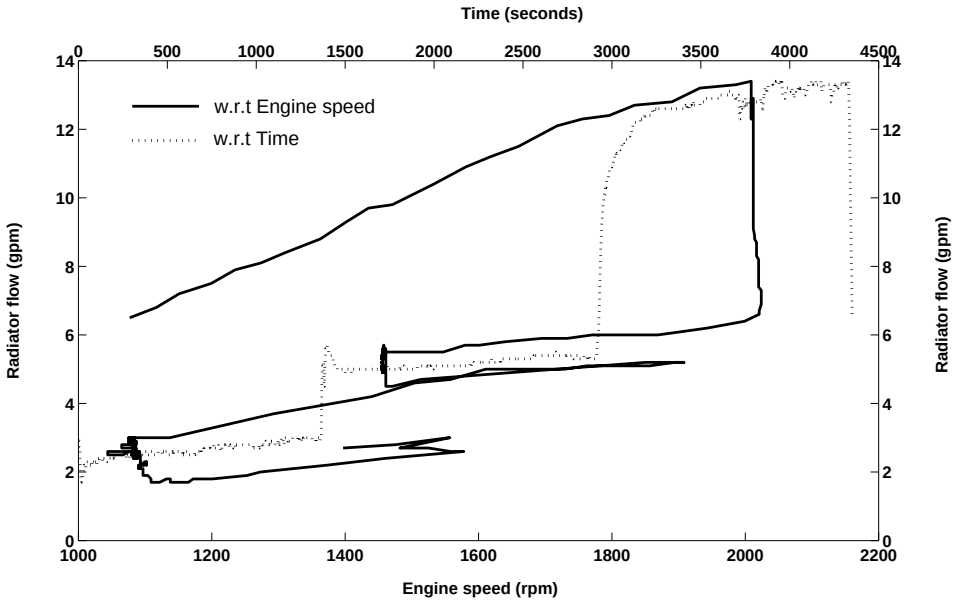

Figure 5.25: Variation of radiator flow rate as a function of engine speed and engine operating time at a tunnel ambient temperature of 100^oF.

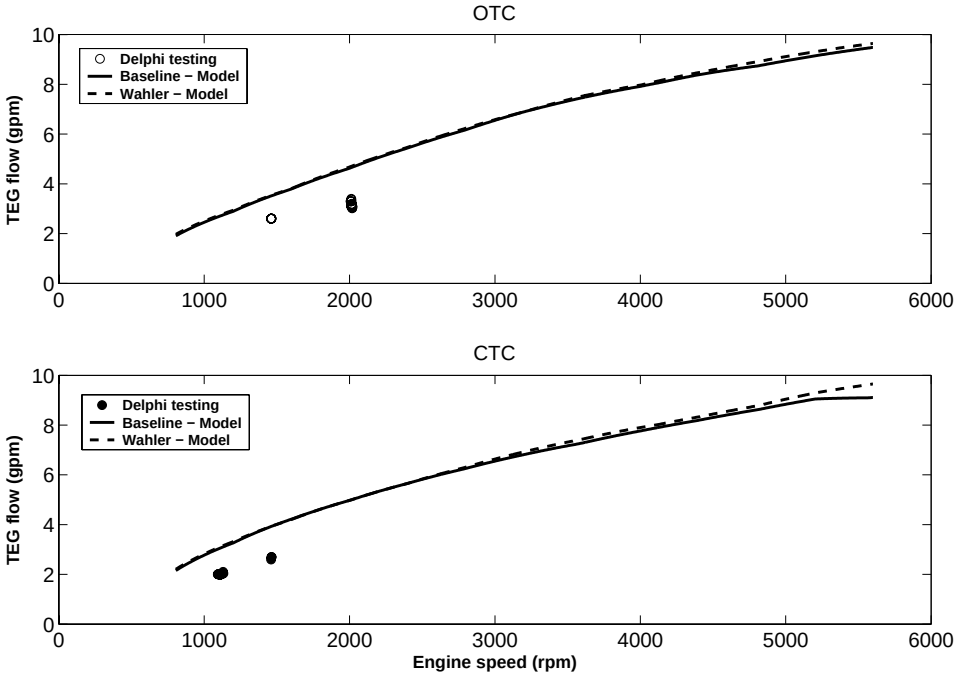

Figure 5.26: Coolant system model validation for the TEG flow.

5.6 Sensitivity Studies on the Coolant System Model

Table (5.2) shows the sensitivity analysis performed on the coolant system model. The analysis was performed corresponding to the flow rates at an engine speed of 2500 *rpm* under baseline open thermostat condition with the TEG circuit. From the results listed in table (5.2), the flow rates through various components of the coolant system are governed by their respective loss coefficients. The total flow rate is predominantly governed by the loss coefficient of the engine, coolant properties: density and viscosity, and coolant temperature with sensitivity coefficients of (-0.183), (0.345), (-0.337), and (0.575). The change in TEG flow rate has a smaller influence on the other components of the coolant system.

The coolant system model predicts the flow rates through different components and the TEG circuit close enough to the GM data and the Delphi testing, except for the flow through the radiator. Based on this model the coolant flow in to the TEG model and the percent change in flow rates and the additional coolant pumping power required because of the addition of the TEG circuit can be estimated reliably.

Variable number	**Variable**	Sensititvity coefficient Total Q	Sensititvity coefficient Heater Q	Sensititvity coefficient Radiator Q	Sensititvity coefficient TEG Q
Input parameters					
Loss coefficients					
1	k_1	-0.02770	-0.01980	-0.02260	-0.01750
2	k_2	-0.18320	-0.13150	-0.15010	-0.11610
3	k_3	-0.00430	-0.06730	0.00260	0.00200
4	k_4	-0.01300	-0.20260	0.00800	0.00610
5	k_5	-0.01540	-0.24110	0.00950	0.00730
6	k_6	-0.00150	0.00079	0.00090	0.00069
7	k_7	-0.07330	0.03880	0.04440	0.03430
8	k_8	-0.03120	0.01670	-0.08780	0.01480
9	k_9	-0.08600	0.04580	-0.24140	0.04040
10	k_{10}	-0.00980	0.00530	-0.02760	0.00460
11	k_{11}	-0.03730	0.01990	-0.10470	0.01760
12	k_{12}				
13	k_{TEG}	-0.03020	0.01620	0.01850	-0.45140
Coolant properties					
14	Density	0.34550	-0.03570	0.09270	-0.15880
15	Viscosity	-0.33700	0.01770	-0.11800	0.14830
16	Coolant temperature	0.57480	-0.07100	0.13450	-0.18580

Table 5.2: Sensitivity analysis on the coolant system.

Chapter 6

TEG System Modeling

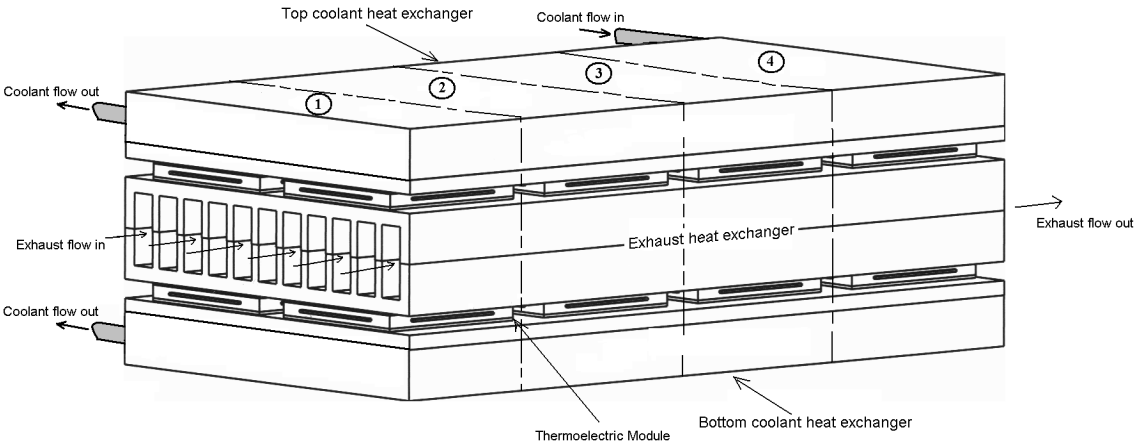

Figure 6.1: Assembled thermoelectric generator.

The following chapter discusses the TEG system modeling and its validation against the results from the Delphi testing. Figure (6.1) shows an assembled thermoelectric generator without the outer casing. As discussed earlier the TEG consists of an exhaust gas heat exchanger, two coolant heat exchangers, and sixteen Hi-Z HZ 20 thermoelectric modules. Electrical power is generated due to the temperature difference across the modules, created by the exhaust gas and the engine coolant. The power generated is supplied to the vehicle electrical bus.

Given exhaust gas inlet temperature and flow rate, coolant inlet temperature and flow rate, and external load resistance, the TEG system model predicts the exhaust gas and coolant outlet temperature, TE module surface temperatures, power generated by the individual modules and the generator, and pressure drop across the exhaust and coolant heat exchangers.

6.1 Modeling

In the following section an analysis of the TEG system is performed. Based on this analysis (1) the temperature distribution along the axial direction of the exhaust and coolant heat exchangers, (2) power generated by the TEG, and (3) the pressure drop across the exhaust and coolant exchangers are estimated.

The TEG system has been modeled under the following assumptions: (1) the exteriors and sides of the heat exchangers and the gaps between the TE modules are perfectly insulated and (2) the material of the heat exchangers provides negligible thermal resistance to heat flowing normal to the plane of the TE modules.

The complete TEG system has been divided into four symmetric sections as shown in figure (6.1). Because of the symmetry, the four modules in section (1) will have the same temperature profile. This is also true for the other three sections. Therefore the temperature distribution has been estimated for a single module in each section and the same temperature profile has been used in estimating the power from the other three modules with in the same section. Thus the temperature distribution along the axial direction of the heat exchangers can be estimated. Using the estimated temperature distribution, the power generated by all the sixteen modules can be calculated using Hi-Z HZ20 thermoelectric module modeling.

6.1.1 Heat Transfer Analysis of a Single TE Module with in the TEG System

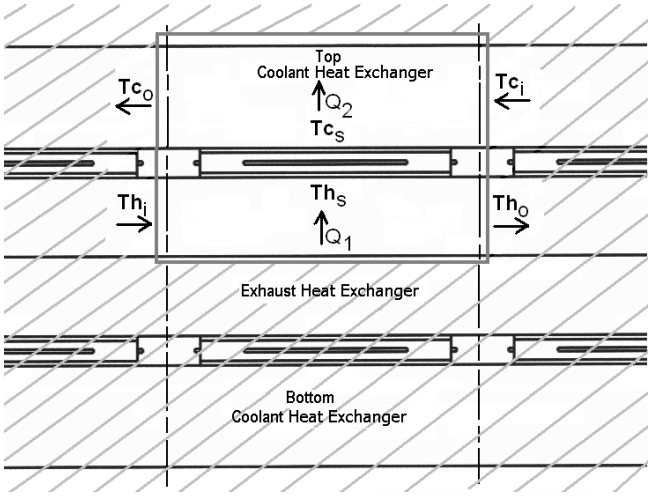

Figure 6.2: Heat transfer for an isolated single TE module of a TEG system.

In the following section the heat transfer analysis of single thermoelectric module is discussed, based on which the complete model of the TEG system was developed. Figure (6.2) shows the heat flow in an isolated thermoelectric module of a TEG system. The equation governing the conservation of exhaust gas energy can be expressed as:

$$Q_1 \;=\; m_h c_{p_h}(T_{h_i} - T_{h_o}) \tag{6.1}$$

where Q_1 is the energy gained from the exhaust, m_h is the mass flow rate of the exhaust gas, c_{p_h} is the specific heat of the exhaust gas, T_{h_i} is the exhaust inlet temperature, and T_{h_o} is the exhaust outlet temperature. The equation governing the convective heat transfer at the hot surface can be expressed as:

$$Q_1 \;=\; h_h A_h \left(\frac{T_{h_i} + T_{h_o}}{2} - T_{h_s} \right) \tag{6.2}$$

where Q_1 is the convective heat transfer at the hot surface, h_h is the heat transfer coefficient on the exhaust side, A_h is the total heat transfer area on the exhaust side, and T_{h_s} is the exhaust side surface temperature of the module. The equation governing the heat input to the thermoelectric module can be expressed as [15]:

$$Q_1 = K\triangle T + \alpha T_{h_s} I - \frac{1}{2} I^2 R_i \tag{6.3}$$

where Q_1 is the heat input to the thermoelectric module. The equation governing the convective heat transfer at the cold surface can be expressed as:

$$Q_2 = h_c A_c \left(T_{c_s} - \frac{T_{c_i} + T_{c_o}}{2} \right) \tag{6.4}$$

where Q_2 is the convective heat transfer at the cold surface, h_c is the heat transfer coefficient on the coolant side, A_c is the total heat transfer area on the coolant side, T_{c_s} is the coolant side surface temperature of the module, T_{c_i} is the coolant inlet temperature, and T_{c_o} is the coolant outlet temperature. The equation governing the conservation of coolant energy can be expressed as:

$$Q_2 = m_c c_{p_c} (T_{c_o} - T_{h_i}) \tag{6.5}$$

where Q_2 is the energy lost to the coolant, m_c is the mass flow rate of the coolant and c_{p_c} is the specific heat of the coolant. The power generated by the thermoelectric module can be expressed as:

$$P = I^2 R_L = \frac{\alpha^2 (T_{h_s} - T_{c_s})^2}{(R_i + R_L)^2} R_L \tag{6.6}$$

where I is defined by the equation (2.8). Using the system of equations (1.1), (1.2), (1.3), (1.4), (1.5), and (1.6), the following four equations in four unknowns, (T_{c_o}, T_{h_s}, T_{c_s}, and T_{h_o}) can be formed:

$$\left.\begin{array}{l} m_h c_{p_h}(T_{h_i} - T_{h_o}) - h_h A_h \left(\frac{T_{h_i}+T_{h_o}}{2} - T_{h_s}\right) \;=\; 0 \\ m_c c_{p_c}(T_{c_o} - T_{h_i}) - h_c A_c \left(T_{c_s} - \frac{T_{c_i}+T_{c_o}}{2}\right) \;=\; 0 \\ h_h A_h \left(\frac{T_{h_i}+T_{h_o}}{2} - T_{h_s}\right) - h_c A_c \left(T_{c_s} - \frac{T_{c_i}+T_{c_o}}{2}\right) - \frac{\alpha^2 (T_{h_s}-T_{c_s})^2}{(R_i+R_L)^2} R_L \;=\; 0 \\ h_h A_h \left(\frac{T_{h_i}+T_{h_o}}{2} - T_{h_s}\right) - K\triangle T - \alpha T_{h_s} I + \frac{1}{2} I^2 R_i \;=\; 0 \end{array}\right\}. \qquad (6.7)$$

Using multi-dimensional Newton-Raphson method the above system, equation set (6.7), can be solved to find the vector of unknowns T_{c_o}, T_{h_s}, T_{c_s}, and T_{h_o}. When the absolute difference of the unknowns between two successive iterations is below a predetermined tolerance limit, the Newton-Raphson iteration is terminated. Extending the heat transfer analysis of a single module system to an n-module system, we will have n-coupled system of equations which are again solved by multi-dimensional Newton-Raphson method. Equation (6.8) defines the multidimensional Newton Raphson method,

$$\overrightarrow{x}^{k+1} \;=\; \overrightarrow{x}^{k} - J\left(\overrightarrow{x}^{k}\right)^{-1} F\left(\overrightarrow{x}^{k}\right) \qquad (6.8)$$

where $\overrightarrow{x}$ is the vector of unknowns, $F(\overrightarrow{x})$ is the function that needs to be solved, $J(\overrightarrow{x})$ is the Jacobian of $F(\overrightarrow{x})$, and k is the iteration counter.

The Seebeck coefficient, internal resistance, and thermal conductivity in equations (6.3) and (6.6) are determined using the Hi-Z HZ20 thermoelectric module modeling.

6.2 Exhaust Heat Exchanger Heat Transfer Coefficient and Pressure Drop Correlations

In the following section, correlations used in modeling the heat transfer and pressure drop for the exhaust heat exchanger are discussed. Figure (6.3) shows the geometry and fin arrangement for one-half of the exhaust gas heat exchanger. The heat transfer coefficient and pressure drop correlations have been obtained from [29]. The authors studied the Colburn factor-j and the average Fanning friction factor-f characteristics of a rectangular offset-strip-fin compact heat exchanger that is almost identical to the exhaust gas heat exchanger used in the TEG system. The Colburn factor is defined as [29]:

$$j = \frac{Nu}{RePr^{\frac{1}{3}}} \tag{6.9}$$

and the average Fanning friction factor is defined as [21]:

$$f = \frac{fr}{4} \tag{6.10}$$

where fr is the (Moody or Darcy) friction factor. They developed correlations for j and f that are single predictive equations representing the data, obtained from the previous studies conducted from the year 1942 to 1987 on offset-strip-fin arrays, from laminar to turbulent flow. Figure (6.4) shows the geometry of the offset-strip-fin array, based on which the correlations were developed. The flow configuration is geometrically described by the fin length, l, height, h, transverse spacing, s, and thickness, t. The offset is usually uniform and equal to the half fin spacing.

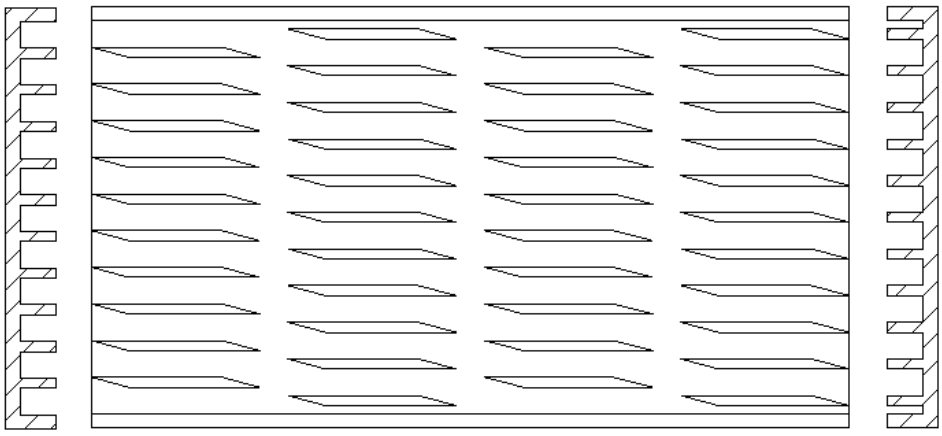

Figure 6.3: One half of the exhaust gas heat exchanger.

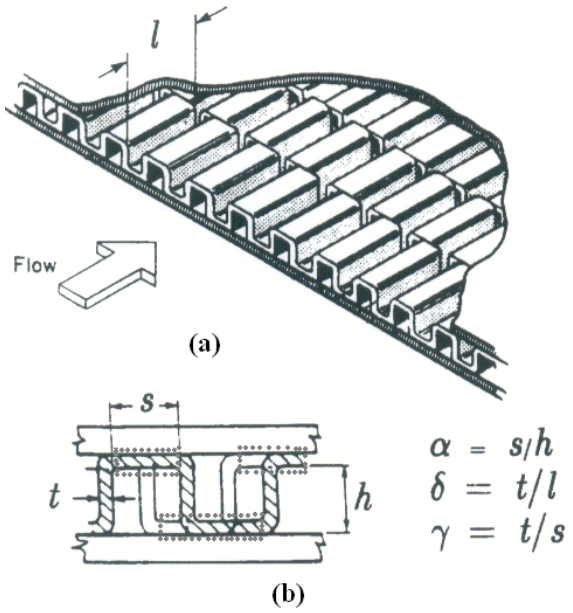

Figure 6.4: Geometry of the offset-strip-fin array, based on which equations (6.11) and (6.12) were developed [29].

The correlation for the colburn factor-j was defined as:

$$\begin{aligned} j &= 0.6522Re^{-0.5403}\alpha^{-0.1541}\delta^{0.1499}\gamma^{-0.0678} \\ &\quad \{1+5.269\times10^{-5}Re^{1.34}\alpha^{0.504}\delta^{0.456}\gamma^{-1.055}\}^{0.1} \end{aligned} \tag{6.11}$$

and the correlation for the fanning friction factor-f was defined as:

$$\begin{aligned} f &= 9.6243Re^{-0.7422}\alpha^{-0.1856}\delta^{0.3053}\gamma^{-0.2659} \\ &\quad \{1+7.669\times10^{-8}Re^{4.429}\alpha^{0.920}\delta^{3.767}\gamma^{0.236}\}^{0.1} \end{aligned} \tag{6.12}$$

where α, δ, and γ are defined as shown in figure (6.4). Equations (6.11) and (6.12) were validated against the experimental data for the offset-strip-fin surfaces listed in table (6.1). The results from the validation for j and f are shown in figures (6.5) and (6.6). From the figures equations (6.11) and (6.12) correlate the experimental data for the eighteen cores of table (6.1) with in $\pm20\%$.

In equations (6.11) and (6.12), the Reynolds number is based on the hydraulic diameter defined as:

$$\left.\begin{aligned} D_h &= \tfrac{4A_c}{\frac{A}{l}} \\ A_c &= sh \\ A &= 2(sl+hl+th)+ts \end{aligned}\right\}. \tag{6.13}$$

For the exhaust heat exchanger of the TEG system, the portion of the fin-strip shown with the dotted line in figure (6.4(b)) does not exist. Therefore the hydraulic diameter was re-defined as:

$$\left.\begin{aligned} D_h &= \tfrac{4A_c}{\frac{A}{l}} \\ A_c &= sh \\ A &= 2(sl+hl+th) \end{aligned}\right\}. \tag{6.14}$$

Reference	*Surface*	D_h*(mm)*	α	δ	γ
Kays and					
London [4]	1/8̊-15.61	2.383	0.244	0.032	0.067
	1/8-19.86	1.542	0.494	0.032	0.086
	1/9-22.68	1.735	0.135	0.036	0.100
	1/9-25.01	1.495	0.184	0.036	0.111
	1/9-24.12	1.209	0.528	0.036	0.107
	1/10-27.03	1.423	0.134	0.040	0.121
	1/10-19.35	1.403	0.672	0.040	0.084
	1/10-19.74	1.219	0.997	0.020	0.041
	3/32-12.22	3.414	0.162	0.043	0.051
	1/2-11.94(D)	2.266	0.711	0.012	0.077
	1/6-12.18(D)	2.636	0.461	0.022	0.051
	1/7-15.75(D)	2.070	0.410	0.028	0.067
	1/8-16.00(D)	1.863	0.477	0.048	0.106
	1/8-19.82(D)	1.539	0.484	0.032	0.086
	1/8-20.06(D)	1.491	0.491	0.032	0.087
London and					
Shah [25]	#501	0.646	1.024	0.020	0.038
Walters [26]	20R/19.43	1.133	1.034	0.060	0.132
	28R/27.20	0.917	0.700	0.060	0.195

Table 6.1: Geometrical parameters for the Database of Offset-strip-fin cores against which equations (6.11) and (6.12) are validated [29].

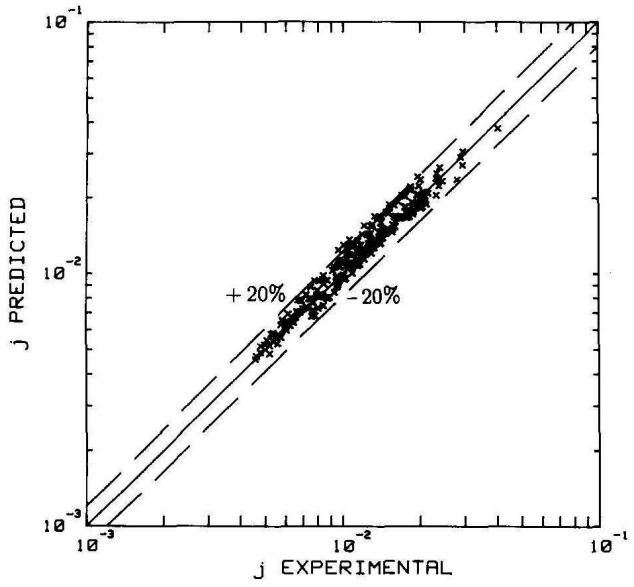

Figure 6.5: Comparison of predictions for j given by equation (6.11) with experimental data for offset strip fin cores listed in table (6.1) [29].

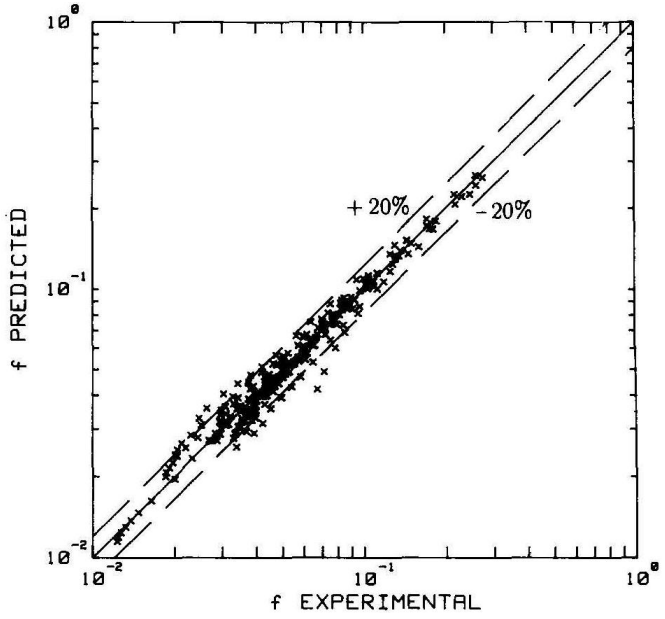

Figure 6.6: Comparison of predictions for f given by equation (6.12) with experimental data for offset strip fin cores listed in table (6.1) [29].

To estimate the additional blow down work due to the back pressure created by the fins of the exhaust heat exchanger, the pressure drop across the exhaust heat exchanger was measured during the testing at Delphi. The sensors used for this measurement were located at the inlet of the inlet transition and the outlet of the outlet transition so these pieces were modeled. The inlet and outlet transition pieces and the location of the pressure sensors are shown in figure (6.7). The inlet transition piece was modeled as a diffuser with splitters and the outlet transition was modeled as a converging transition piece using correlations from [26]. The pressure drop data and the validation of the results from the model against this data will be discussed in the validation section.

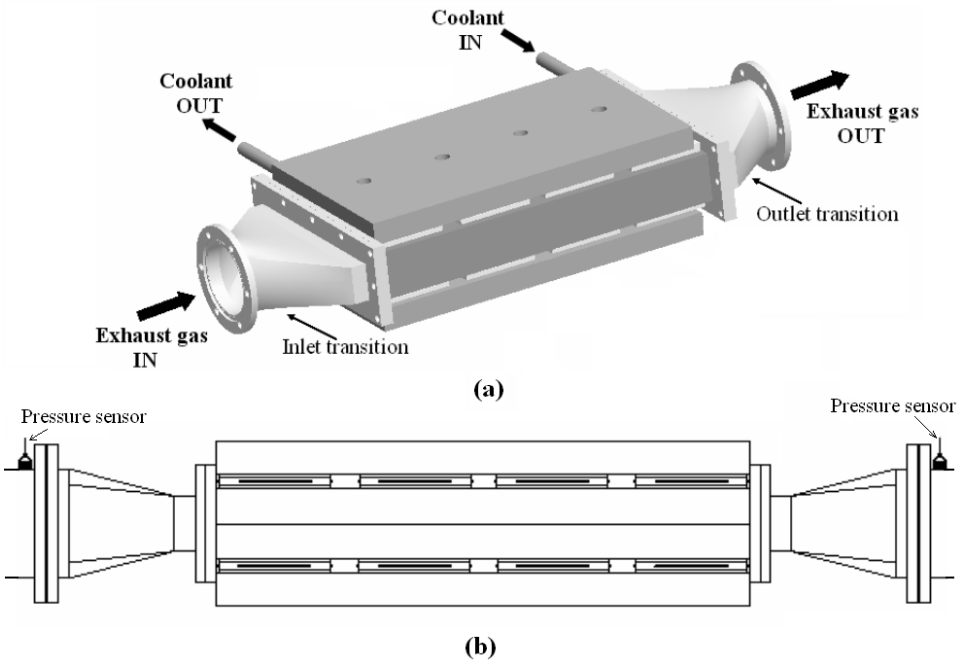

Figure 6.7: (a) Inlet and outlet transition pieces of the exhaust heat exchanger. (b) Location of the pressure sensors used in measuring the pressure drop across the exhaust heat exchanger.

6.3 Coolant Heat Exchanger Heat Transfer Coefficient and Pressure Drop Correlations

In the following section correlations used in modeling the heat transfer and pressure drop for the coolant heat exchanger are discussed. Figure (6.8) shows the top view of the coolant heat exchanger. It contains six rectangular channels of equal cross sectional area, along the axial direction of the heat exchanger. The diverging and converging cross sections, at the inlet and outlet of each rectangular channel, were used to attain uniform flow rate through all the six channels.

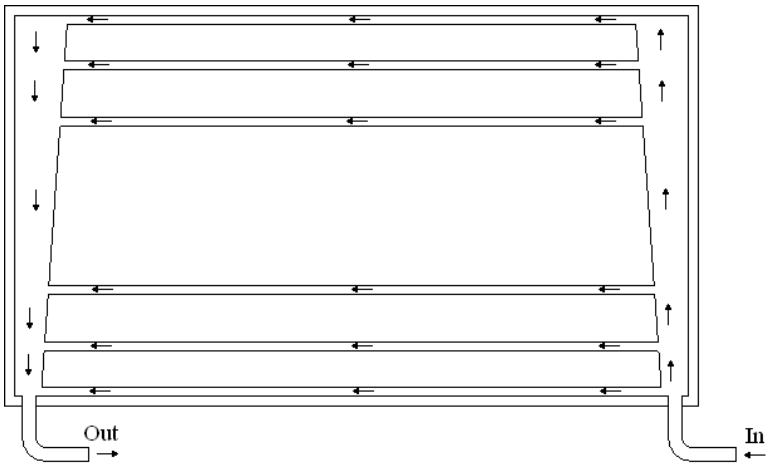

Figure 6.8: Coolant heat exchanger.

As discussed in TEG flow validation, section (5.5), the total flow has been limited to 2 to 3.5 *gpm*. Assuming uniform flow rate through all the 12 rectangular channels of the two coolant heat exchangers, the flow range in each slot varies between 0.1666 to 0.2916 *gpm*. Corresponding to this flow range and the characteristic length of the rectangular channel, the Reynolds number varies between 1300 to 3000. For flow in non-circular ducts the critical Reynolds number for the transition from laminar to turbulent is approximately, 2000 [27]. Therefore the flow through these channels is predominantly within the transition regime.

The heat transfer coefficient for the rectangular channel is defined by the Dittus-Boelter equation [21], equation (6.15) and is valid for ($Re > 10000$).

$$Nu_D = 0.023 Re_D^{0.8} Pr^n \tag{6.15}$$

Where ($n = 0.4$) for heating ($T_s > T_b$) and ($n = 0.3$) for cooling ($T_s < T_b$). T_s and T_b are the wall temperature of the rectangular channel and bulk temperature of the fluid. For the case of the coolant heat exchanger in the TEG system the surface temperature of the rectangular channel is always greater than the bulk temperature of the fluid flowing inside the rectangular channel. Therefore $n = 0.4$ in equation (6.15).

The Dittus-Boelter is predominantly used for estimating the heat transfer coefficient of turbulent flows in circular tubes [21], however it has also been validated against the experimental results for the turbulent flow in rectangular channels [30], figure (6.9) and the validity of the Dittus-Boelter equation for the Reynolds number ranging form $(1300 - 3000)$ will be discussed later in the validation section.

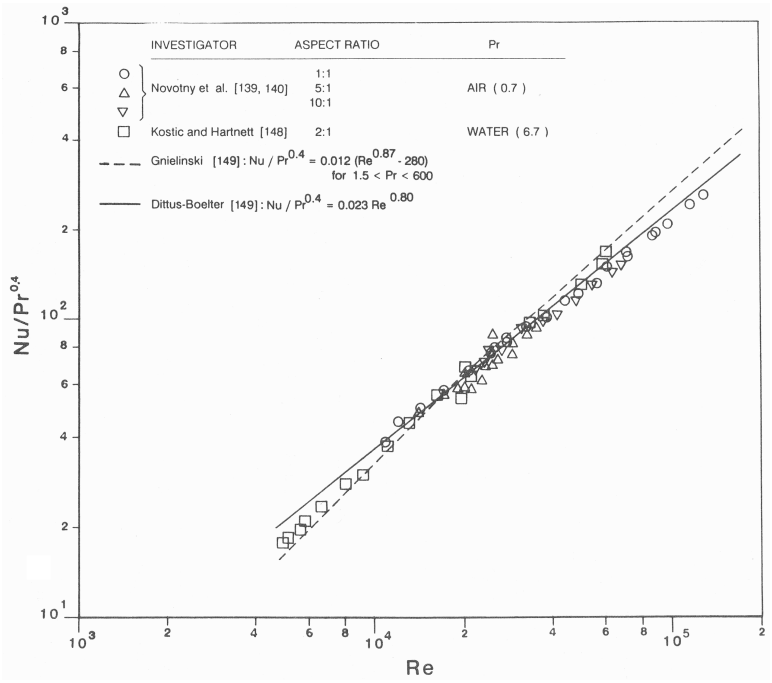

Figure 6.9: Comparison of experimental heat transfer results for turbulent flow of Newtonian fluids in rectangular channels [30].

The pressure drop correlation for the coolant heat exchanger was estimated using correlations from [26] and [27], and is defined by the equation (6.16) [25]. It was modeled as a combination of diffusers, diverging wyes, converging wyes, and converging sections.

$$\triangle p \;=\; 23.743Q^2 + 0.0306Q - 0.0006 \tag{6.16}$$

The units of $\triangle p$ and that of Q in equation (6.16) are in pascal and in gpm. Also, equation (6.16) has been modeled for the coolant flow ranging from 1 to 5 gpm.

In measuring the pressure drop across the coolant heat exchanger, the pressure sensors were located at the common inlet and outlet of the two coolant heat exchangers as shown in figure (6.10). Therefore the total loss coefficient was estimated as a combination of two parallel circuits that consists of T-junctions, elbows, the two coolant heat exchangers, and the tubing necessary to connect them together. The loss coefficients for the T-junctions, elbows and the tubing were estimated using correlations from [27].

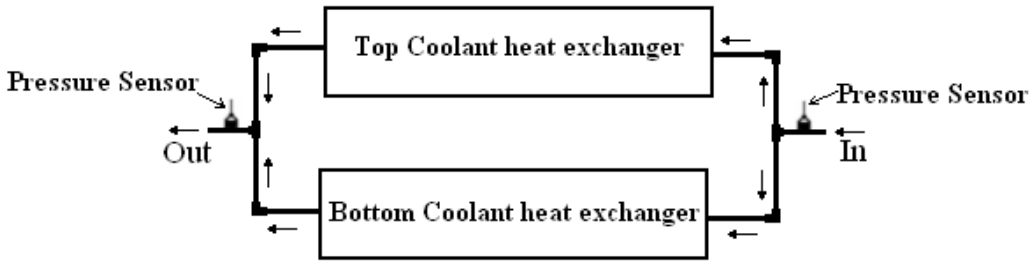

Figure 6.10: Location of the pressure sensors used in measuring the pressure drop across the coolant heat exchanger.

6.4 Range of Reynolds number and Heat Transfer coefficients Based on the Correlations in Sections (6.2) and (6.3) and Flow Conditions from Delphi Experimental Testing

Table (6.2) shows the range of Reynolds number and the heat transfer coefficient for the exhaust and the coolant heat exchangers in the TEG system. The values in the table are based on the equations (6.11) and (6.15). The flow conditions under which the values are calculated are obtained from the Delhi experimental testing.

Configuration ->	B		C		D	
	Reynolds number	Heat transfer coefficient $W/m^2 K$	Reynolds number	Heat transfer coefficient $W/m^2 K$	Reynolds number	Heat transfer coefficient $W/m^2 K$
	Hot side heat transfer coefficient range					
Vehicle Speed						
30	2327 to 2692	43.75 to 48.88	2066 to 2429	44.38 to 50.36	2088 to 2439	44.55 to 50.29
50	3488 to 4020	61.63 to 67.82	3169 to 3638	63.88 to 70.48	3180 to 3628	63.93 to 70.02
70	5387 to 6230	88.48 to 97.58	4931 to 5671	90.61 to 99.57	5193 to 5732	93.58 to 100.27
	Cold side heat transfer coefficient range					
Vehicle Speed						
30	1512 to 1690	1221.3 to 1301.8	1487 to 1656	1211.9 to 1266.6	1298 to 1493	1147.5 to 1215.1
50	1959 to 2203	1503.1 to 1600.8	1934 to 2187	1495.5 to 1572.8	1643 to 1948	1400.5 to 1501.6
70	2307 to 2903	1721.8 to 1937.7	2302 to 3033	1711.7 to 1996.4	1880 to 2440	1568.2 to 1764.1

Table 6.2: Reynolds number and heat transfer coefficient values for the exhaust and coolant heat exchangers in the TEG system.

6.5 Validation

In the following section validation of the results from the TEG system modeling against the results from the Delphi testing will be discussed. A validation for (1) the total power generated by the TEG, (2) outlet temperature of the exhaust gas and the coolant, (3) hot and cold surface temperatures of the thermoelectric modules along the axial direction of the heat exchangers, (4) the total power generated by the TEG based on the experimental surface temperatures and HZ20 model, and (5) pressure drop across the exhaust and coolant heat exchangers were performed.

6.5.1 Validation for the Total Power Generated by TEG

In the following validation for the total power generated by the TEG is discussed. Figure (6.11) shows a comparison of the results from the model and the experiment for the power generated by the TEG. Comparison was made for the configurations B, C, and D. The vertical ranges given for each data point indicate the variability of the power with the tunnel inlet air condition and the electrical load. The model is in good agreement with the experimental results at lower engine speeds, and the difference between them increases with increasing engine speed.

The mean difference between the experiment and the model for each configuration at various vehicle speeds are tabulated in table (6.3) and the maximum difference between the model and the experiment, among various tests cases conducted under each configuration are tabulated in table (6.4). A positive sign represents an over prediction and a negative sign indicates an under prediction by the model.

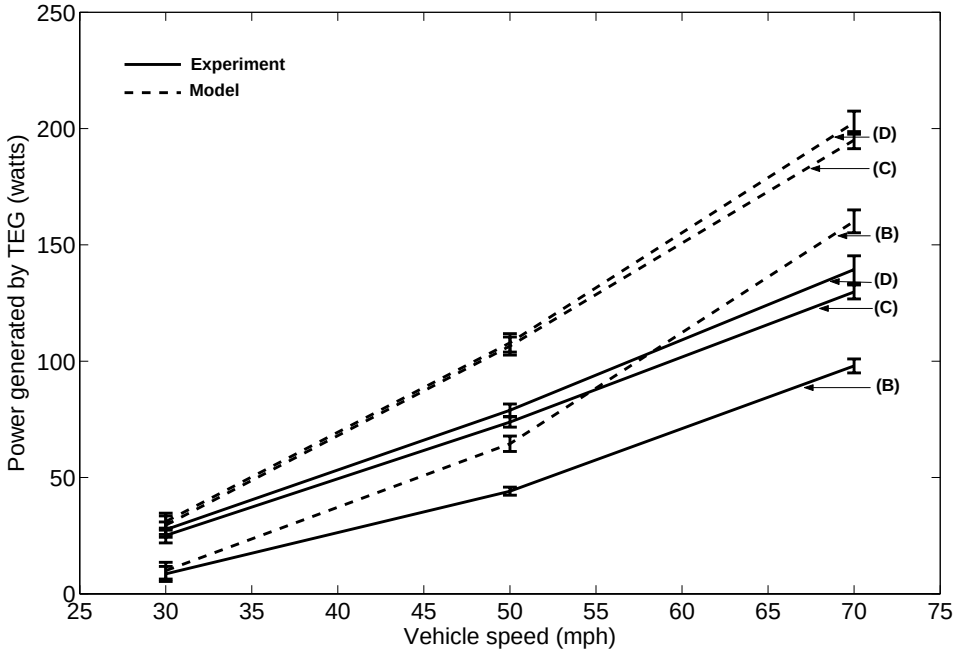

Figure 6.11: Validation for the total power generated by the TEG.

Vehicle speed	Configuration B	Configuration C	Configuration D
30 mph	1.39	4.42	3.44
50 mph	20.37	32.67	28.99
70 mph	62.15	65.28	63.16

Table 6.3: Mean difference between the experiment and the model for the total power generated by the TEG in watts under each configuration at various vehicle speeds.

Configuration	Maximum difference
B	65.66
C	67.27
D	64.56

Table 6.4: Maximum difference between the experiment and the model for the total power generated by the TEG in watts among the various test cases conducted under each configuration.

The deviation of the model from the experiment can be because: (1) in the modeling the exteriors and sides of the heat exchangers and the gaps between the TE modules were assumed to be perfectly insulated, contrary to this there could have been heat losses occurring through the sides and the exteriors and also through the bolts that are used in fastening the heat exchangers, thermoelectric modules, and the outer casing as a single unit and (2) the modeling also assumes uniform flow distribution for the exhaust gas at any given cross section along the axial direction of the heat exchanger. This was probably not the case. Looking at figure (6.8) for the exhaust gas heat exchanger, the wedge shaped edges at the ends of each fin are all unidirectional. This results in higher quantity of mass flow rate accumulating in the lower portion of the geometry. Therefore an unequal distribution of mass flow rate might have occurred. This was verified by running an exhaust heat exchanger model in Fluent. A minimum flow velocity, corresponding to the results from the Delphi testing, simulation was performed. Air was used as the working fluid and the Reynolds Stress Model was used to model the turbulence. The contours of Velocity magnitude from the converged solution is shown in figure (6.12). One can notice that the flow is accumulating in the lower half of the heat exchanger, towards which all the fins are directed, as the fluid flows from the inlet to outlet. This phenomena might have reduced the over all heat transfer coefficient and therefore the modules located in the region, where there is lesser concentration of mass flow rate have lower surface temperatures on the exhaust side.

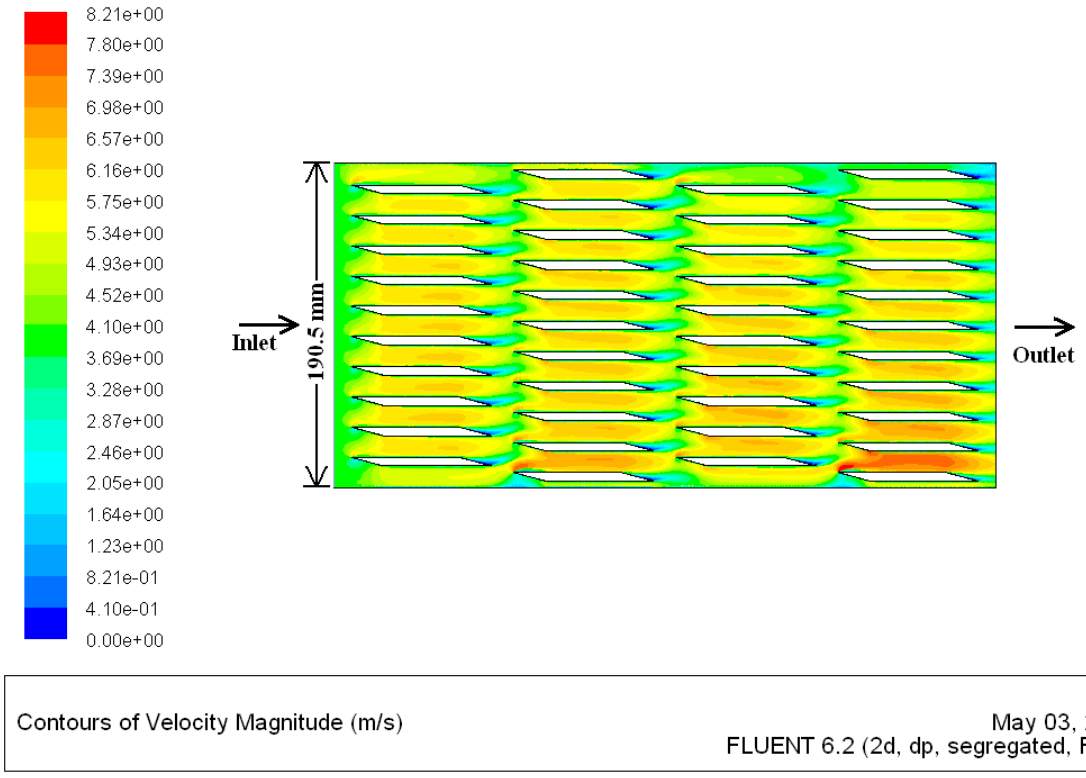

Figure 6.12: Velocity contours for the exhaust heat exchanger with an inlet velocity of $u = 4.0(m/s)$

6.5.2 Validation for Temperature at Various Locations of TEG

Measurement of temperature at various locations of the TEG were recorded during the Delphi testing. The location of these measurements is shown in figure (6.13). ■−represents location of measurements on the exhaust side and •−represents location of measurements on the coolant side. $T1-$is inlet temperature, $T2-$is module surface temperature closer to the inlet, $T3-$is module surface temperature closer to the outlet, and $T4-$is outlet temperature.

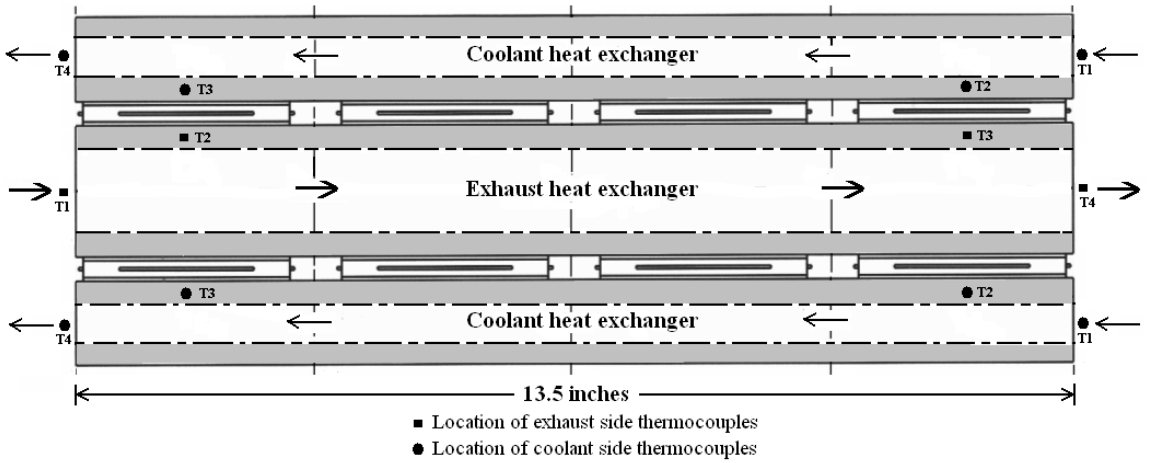

Figure 6.13: Various locations at which temperature measurements in TEG are recorded.

Coolant side module surface temperature was recorded on both the top and bottom coolant heat exchangers. Therefore when validating this variable, the average of the both the measurements was used.

Validation was performed for the (1) bulk temperature of the exhaust gas and the coolant at the outlet and (2) Module surface temperature located on the exhaust and coolant heat exchangers. Figures (6.14), (6.15), and (6.16) show the validation for configurations B, C, and D respectively. The mean temperature difference between the model and the experiment for T2, T3, and T4 on the exhaust side at various vehicle speeds and configurations are tabulated in table (6.5) and table (6.6) corresponds to the coolant side. The maximum difference for T2, T3, and T4 on the exhaust side between the model and the experiment, among various test cases conducted under each configuration are tabulated in table (6.7(a)) and table (6.7(b)) corresponds to the coolant side. A positive sign represents an over prediction and a negative sign indicates an under prediction by the model.

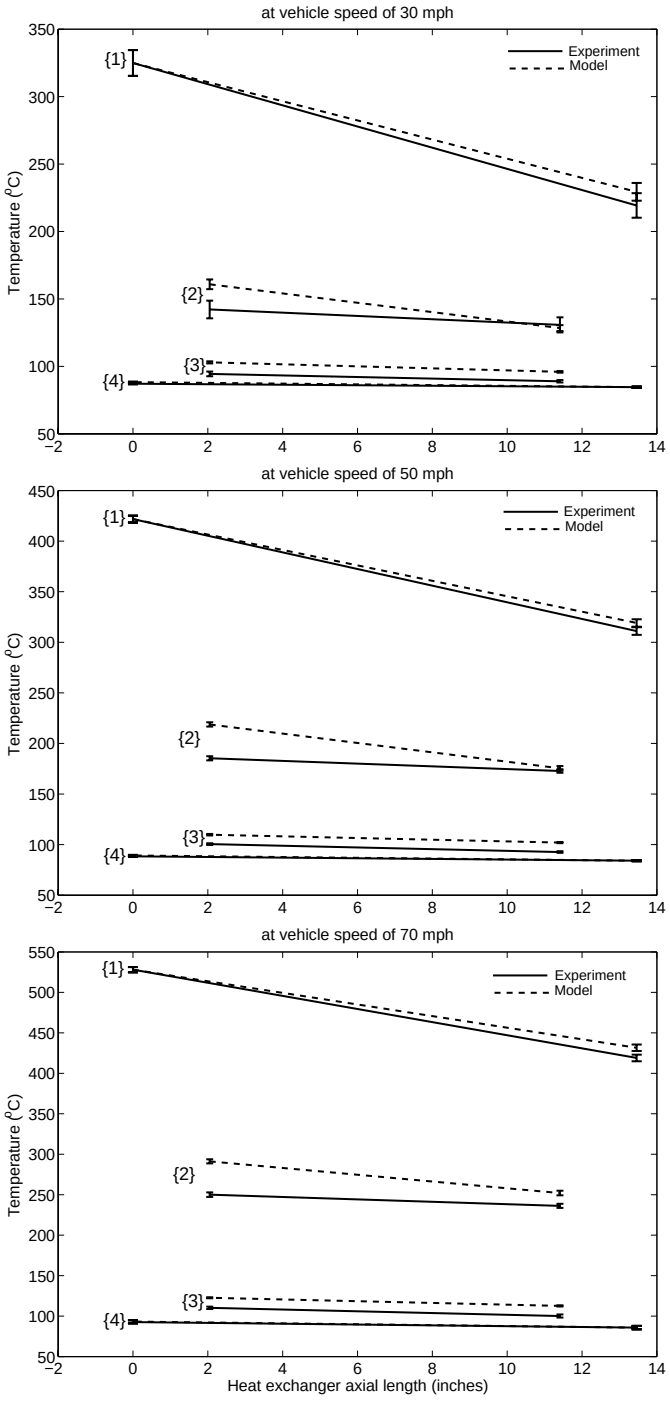

Figure 6.14: Comparison between the model and the experimental data for various temperatures of the TEG in configuration B at different vehicle speeds. {1}-represents the exhaust gas bulk temperatures, {2}-represents the exhaust side surface temperatures of the module, {3}-represents the coolant side surface temperatures of the module, and {4}-represents the coolant bulk temperatures.

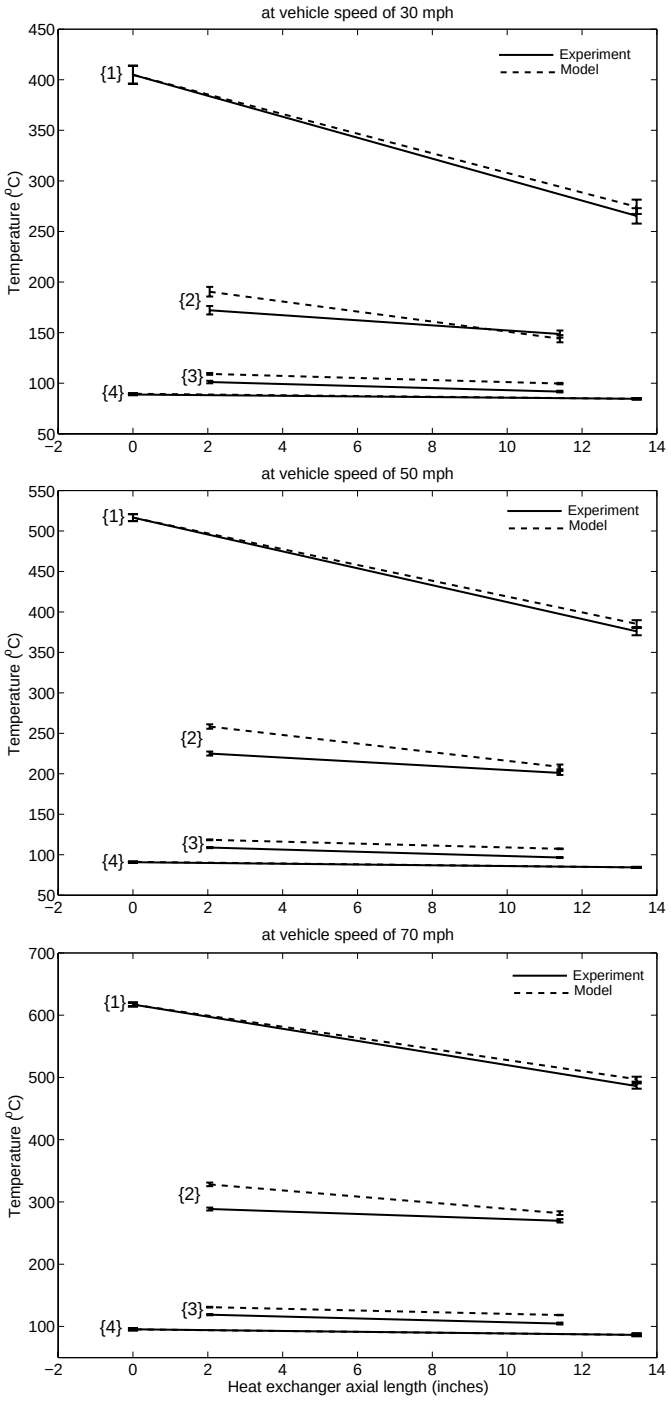

Figure 6.15: Comparison between the model and the experimental data for various temperatures of the TEG in configuration C at different vehicle speeds. {1}-represents the exhaust gas bulk temperatures, {2}-represents the exhaust side surface temperatures of the module, {3}-represents the coolant side surface temperatures of the module, and {4}-represents the coolant bulk temperatures.

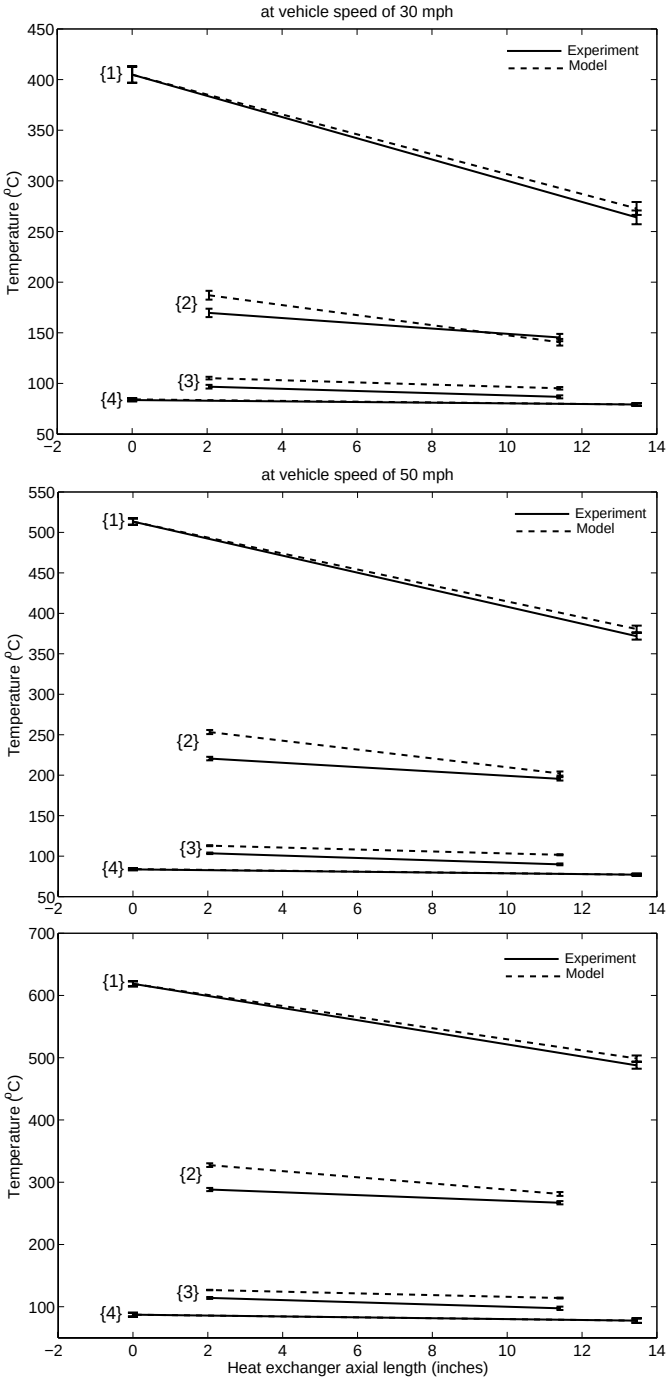

Figure 6.16: Comparison between the model and the experimental data for various temperatures of the TEG in configuration D at different vehicle speeds. {1}-represents the exhaust gas bulk temperatures, {2}-represents the exhaust side surface temperatures of the module, {3}-represents the coolant side surface temperatures of the module, and {4}-represents the coolant bulk temperatures.

Vehicle speed	Configuration B			Configuration C			Configuration D		
	T2	T3	T4	T2	T3	T4	T2	T3	T4
30 mph	18.69	-2.39	10.13	18.29	-4.63	8.96	17.42	-4.67	8.81
50 mph	33.46	2.69	8.00	33.40	7.44	9.21	32.79	6.63	8.78
70 mph	41.15	15.86	12.59	39.49	12.28	11.12	39.21	14.06	11.01

Table 6.5: Mean difference between the experiment and the model for $T2$, $T3$, and $T4$ of exhaust, at various vehicle speeds under each configuration.

Vehicle speed	Configuration B			Configuration C			Configuration D		
	T2	T3	T4	T2	T3	T4	T2	T3	T4
30 mph	6.98	8.54	1.19	7.95	8.03	0.80	8.45	8.45	0.72
50 mph	9.33	9.27	0.85	10.76	9.54	0.44	11.83	9.45	0.44
70 mph	12.49	12.41	0.61	13.65	12.00	-0.15	16.52	12.69	0.02

Table 6.6: Mean difference between the experiment and the model for $T2$, $T3$, and $T4$ of coolant, at various vehicle speeds under each configuration.

Configuration	Temperature	Maximum temperature difference
B	T2	42.15
	T3	17.31
	T4	16.01
C	T2	40.39
	T3	13.59
	T4	11.79
D	T2	40.06
	T3	15.01
	T4	11.57

(a) Exhaust

Configuration	Temperature	Maximum temperature difference
B	T2	13.93
	T3	13.70
	T4	1.884
C	T2	15.99
	T3	14.03
	T4	1.045
D	T2	17.89
	T3	13.72
	T4	0.977

(b) Coolant

Table 6.7: Maximum difference between the experiment and the model for $T1$, $T2$, $T3$, and $T4$ for various test cases conducted under each configuration. (a)Exhaust and (b)Coolant.

From figures (6.14), (6.15), and (6.16) and tables (6.5) and (6.6) we can conclude that the results for the outlet-($T4$) temperature of both the exhaust and the coolant from the modeling are in good agreement with the results from the Delphi testing. Though the differences between the model and the experiment for T4 on the exhaust side are on the order of (8-16)^oC, when compared with the magnitude of T4 these differences are negligible.

The maximum deviation between the experiment and the model can be noticed for T2 and T3 of both the exhaust and the coolant. These deviations can be attributed to the same reasons that are used in justifying the disagreement between the model and the Delphi testing results for the total power generated by the TEG.

As discussed in section (6.3) the heat transfer coefficient for the rectangular channels of the coolant heat exchanger is calculated using Dittus-Boelter equation, equation (6.15) and is valid for ($Re > 10,000$). But the Reynolds number for the flow through these channels is on the order of (1300-3000). However, the use of Dittus-Boelter equation was justified with respect to the comparison of the modeling results against the results from the Delphi testing. Parameters such as (1) the total power generated and (2) the bulk temperature of the fluids and the surface temperatures of the modules along the axial direction of the heat exchangers, based on the Dittus-boelter equation were in good agreement with the results from the Delphi testing compared to the TEG system model results based on other correlations available in both the laminar and the turbulent flow regimes. Though some of the correlations were able to predict the total power generated by TEG better than the Dittus-Boelter equation against the results from the Delphi testing, they were not in good agreement with the bulk and surface temperatures. An appropriate correlation is one that captures the overall system behavior.

6.5.3 Validation for the Total Power Generated by TEG Based on the Experimental Surface Temperatures and the Hi-Z HZ20 Model

In the following validation for the total power generated by the TEG based on the experimental surface temperatures and the Hi-Z HZ20 model is discussed. This analysis was performed to validate the thermoelectric properties based on the HZ20 experimental data obtained by Hi-Z. Figure (6.17) shows a comparison of the results based on the HZ20 model and the experiment for the power generated by the TEG. The model is in good agreement with the experimental results at lower engine speeds, and the difference between them increases with increasing engine speed. The trend is almost similar to the comparison of power shown in figure (6.11). The deviation of the model from the experiment continues to exist. This is caused predominantly by the HZ20 thermoelectric properties, though the possibility of errors in the measurement of surface temperatures or due to the difference in the measurement of surface temperatures caused by the offset in the location of thermocouples from the surface of the module cannot be ruled out.

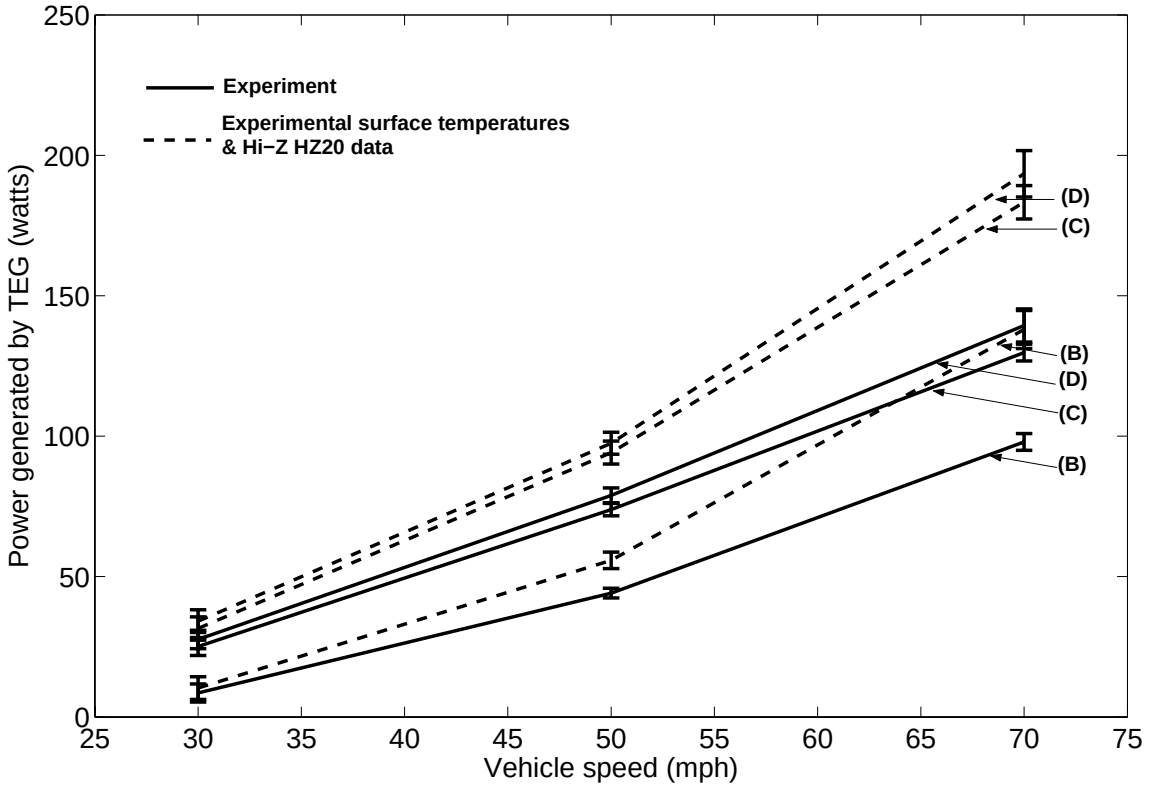

Figure 6.17: A comparison of the power generated by the TEG based on the experimental surface temperatures and the Hi-Z HZ20 model to that of the experimental results.

6.5.4 Validation for the Pressure Drop Across the Exhaust Heat Exchanger

To estimate the additional blow down work due to the back pressure created by the fins of the exhaust heat exchanger, the pressure drop across the exhaust heat exchanger was measured during the testing at Delphi.

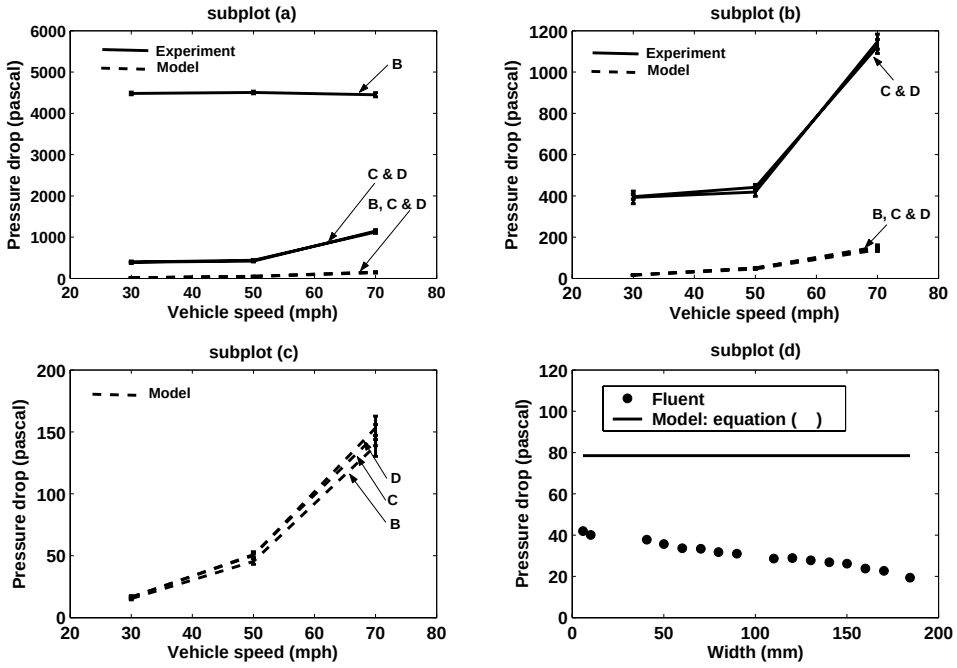

Figure 6.18: Validation of pressure drop across the exhaust heat exchanger

Vehicle speed		Configuration B	Configuration C	Configuration D
30 mph	Experiment	489.2	4324	4317.5
	Model	5398	5194	5216
	Difference	4909	869.9	898.6
50 mph	Experiment	535.4	7354	7330.1
	Model	9109	8786	8821
	Difference	8574	1431.6	1490.5
70 mph	Experiment	1232.3	10631	9973.6
	Model	12990	13687	12528
	Difference	11758	3056.6	2554.7

Table 6.8: Results from the model, experiment and their difference for pressure drop across the exhaust heat exchanger, at various vehicle speeds under each configuration.

Figure (6.18) shows the validation for this measurement. The results from the model, experiment and the difference between the model and the experiment are tabulated in table (6.8). From the results of the Delphi testing shown in figure (6.18 subplot(a)), there is a large change in magnitude between configuration (B) and configurations (C and D). Based on the operating conditions and design of the TEG system, results from all the three configurations should roughly be on the same order of magnitude. But B is almost four times that of either C or D. Therefore B has been ruled out as an experimental error. Yet there still is a huge difference between the model and the experiment, as shown in figure (6.18 subplot(b)). Therefore results from the fluent, section (6.5.1), was used to verify the validity of the model and the experiment. Based on this model, the pressure drop across the exhaust heat exchanger is shown in figure (6.18 subplot(d)). The result from Fluent was compared to the pressure drop that was evaluated using equation (6.12). The difference between the result from equation (6.12) and Fluent model is due to the wedge shaped edges at the ends of the fins. These wedge shaped edges reduce the pressure drop, therefore the fluent model has a lower pressure drop compared to equation (6.12), which does not model such edges. It has to be noted that in subplots (a), (b), and (c) of figure (6.18), the pressure drop is measured across the inlet of inlet transition and outlet of outlet transition, whereas the subplot (d) corresponds to the pressure drop across the exhaust heat exchanger only.

From subplots (c) and (d) of figure (6.18), the $\triangle p$ from the model and Fluent are roughly on the same order of magnitude. Also, the inlet and outlet transition pieces do not account for much of a pressure drop compared to the exhaust heat exchanger. Therefore the results from the Delphi testing might have an experimental error associated with them.

6.5.5 Validation for the Pressure Drop Across the Coolant Heat Exchanger

The validation for the pressure drop across the coolant heat exchanger is shown in figure (6.19).The results from the model, experiment and the difference between the model and the experiment are tabulated in table (6.9).

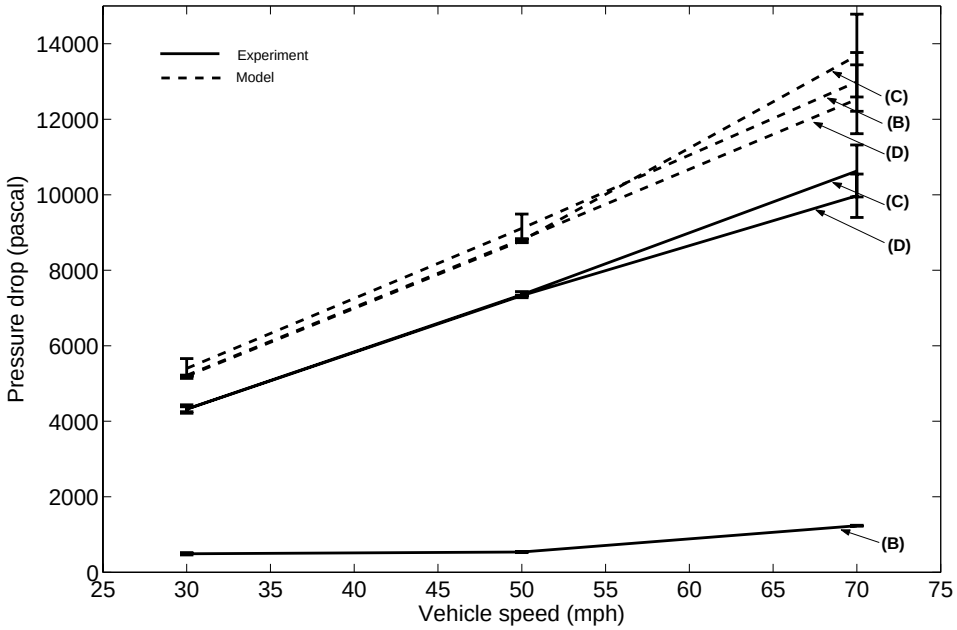

Figure 6.19: Validation of pressure drop across the coolant heat exchanger

From the results of the Delphi testing shown in figure (6.19), there is a large change in magnitude between configuration (B) and configurations (C and D). This may be because of an experimental error associated with configuration B. Therefore validation for configuration B was not considered. The deviation of model from the experimental results can be due to the inaccurate estimation of the loss coefficients of the T-junction, elbow, or coolant heat exchanger. Yet, the results from the modeling for configurations C and D are able to match the trend in the data of Delphi testing.

Vehicle speed		Configuration B	Configuration C	Configuration D
30 mph	Experiment	489.2	4324	4317.5
	Model	5398	5194	5216
	Difference	4909	869.9	898.6
50 mph	Experiment	535.4	7354	7330.1
	Model	9109	8786	8821
	Difference	8574	1431.6	1490.5
70 mph	Experiment	1232.3	10631	9973.6
	Model	12990	13687	12528
	Difference	11758	3056.6	2554.7

Table 6.9: Results from the model, experiment and their difference for pressure drop across the coolant heat exchanger, at various vehicle speeds under each configuration.

6.6 Energy Budget for the TEG Model

The energy budget based on the TEG model for the cases of minimum and maximum power generated during the experimental testing is shown in figures (6.20) and (6.21). A 0.22% energy is extracted from the exhaust stream when the TEG generated the minimum power and 2.82% energy is extracted from the exhaust stream when the TEG generated maximum power. Based on these results the design of the exhaust and coolant heat exchangers needs further improvement to be able to extract more amount of energy from the exhaust.

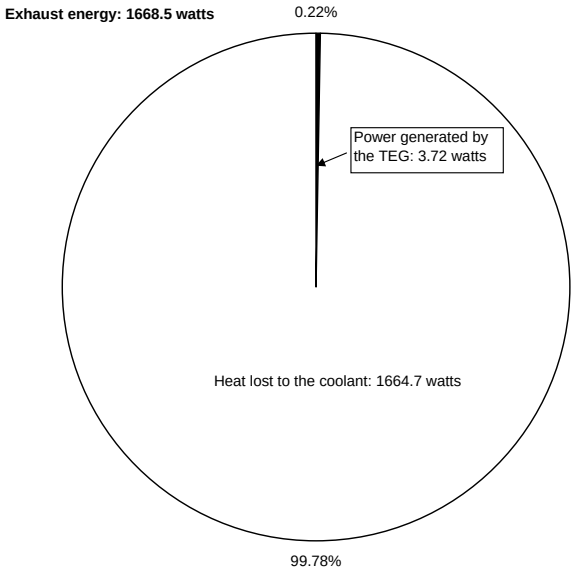

Figure 6.20: Energy budget based on the TEG model for the case of minimum power generated by the TEG.

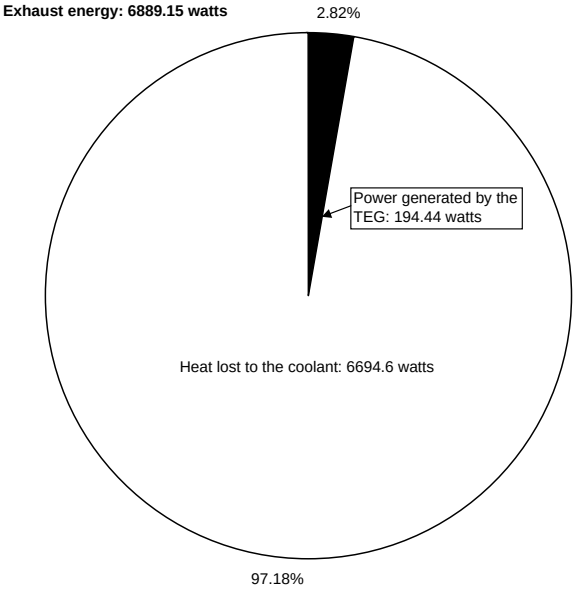

Figure 6.21: Energy budget based on the TEG model for the case of maximum power generated by the TEG.

6.7 Sensitivity Analysis on the TEG System

Table (6.10) shows the sensitivity analysis performed on the TEG system. The analysis was performed for the case of TEG with exhaust insulation and pre-coolant heat exchanger at a vehicle speed of 70 mph, tunnel ambient temperature of 40^oF, and an electrical load of $(Base + 50)$ $amps$. This case also corresponds to the maximum power generated by the TEG during the Delphi experimental testing when engine coolant was used as the heat sink source. The most important output of the model is the TEG power. The parameters that have the strongest impact on the power generated by the TEG are: exhaust inlet temperature, coolant inlet temperature and the HZ20 thermoelectric module properties seebeck coefficient, internal resistance, and thermal conductance with sensitivity coefficients of (1.324), (-1.377), (1.635), (-0.971), and (-0.810). The thermal resistance from the heat exchanger materials and the Al_2O_3 wafers have a negligible effect on both the output parameters: power generated by the TEG and the temperatures. If the exhaust inlet temperature and the coolant inlet temperature are excluded as input parameters, then the HZ20 thermoelectric module properties can cause significant changes in the power generated by the TEG compared to the other model parameters.

Variable number	Variable	Sensititvity coefficient Current	Sensititvity coefficient Voltage	Sensititvity coefficient Power	Sensititvity coefficient Hot junction temperature (inlet side)	Sensititvity coefficient Hot junction temperature (outlet side)	Sensititvity coefficient Exhaust outlet temperature (outlet side)	Sensititvity coefficient Cold junction temperature (inlet side)	Sensititvity coefficient Cold junction temperature (outlet side)	Sensititvity coefficient Coolant outlet temperature (outlet side)
Input parameters										
1	Exhaust inlet temperature	0.64130	0.64130	1.32370	0.57040	0.57790	0.81310	0.18040	0.27730	0.05610
2	Exhaust mass flow rate	0.16500	0.16500	0.33280	0.09130	0.14690	0.08570	0.04450	0.04330	0.01050
3	Coolant inlet temperature	-0.71430	-0.71430	-1.37750	0.24730	0.29010	0.07300	0.68060	0.63940	0.95670
4	Coolant flow rate	0.09930	0.09930	0.19970	-0.02960	-0.02940	-0.00790	-0.06490	-0.07990	-0.02370
5	Current generated by the TEG									
6	Voltage generated by the TEG									
7	Load Resistance	-0.37990	0.58210	0.18000	0.00810	0.01290	0.00300	-0.00290	-0.00260	-0.00070
Hi-Z HZ20 Module										
8	Seebeck coefficient	0.78520	0.78520	1.63490	-0.05100	-0.07240	-0.01740	0.00780	0.00730	0.00190
9	Internal Resisitance	-0.49800	-0.49800	-0.97090	0.01410	0.02180	0.00520	-0.00084	-0.00031	-0.00019
10	Thermal conductance	-0.41200	-0.41200	-0.81000	-0.14520	-0.15880	-0.04220	0.02770	0.04020	0.00840
Heat transfer coefficients										
11	Exhaust side heat transfer coefficient	0.18060	0.18060	0.36450	0.14660	0.12220	-0.06900	0.03770	0.06690	0.01240
12	Coolant side heat transfer coefficient	0.11130	0.11130	0.22380	-0.03150	-0.03470	-0.00880	-0.07780	-0.08480	0.00150
Exhaust gas properties										
13	Density									
14	Viscosity	-0.11150	-0.11150	-0.22180	-0.08720	-0.06910	0.03750	-0.02130	-0.03470	-0.00670
15	Thermal conductivity	0.18130	0.18130	0.36580	0.14710	0.12260	-0.06920	0.03790	0.06710	0.01250
16	Specific heat	0.06290	0.06290	0.12620	0.00940	0.07570	0.12230	0.02250	0.00610	0.00350
17	Prandtl number	0.06240	0.06240	0.12510	0.04890	0.04100	-0.02290	0.01260	0.02210	0.00410
Prestone Anti-freeze coolant properties										
18	Density	0.09930	0.09930	0.19970	-0.02960	-0.0294	-0.0079	-0.0649	-0.07990	-0.02370
19	Viscosity	-0.04700	-0.04700	-0.09390	0.01360	0.01470	0.00370	0.03300	0.03590	-0.00062
20	Thermal conductivity	0.06790	0.06790	0.13620	-0.01940	-0.02130	-0.00540	-0.04770	-0.05200	0.00089
21	Specific heat	0.05500	0.05500	0.11040	-0.01710	-0.01570	-0.00440	-0.03410	-0.04620	-0.02450
Thermal resistance										
22	Thermal conductivity Al2O3 wafers	0.00007	0.00007	0.00014	-0.00001	-0.00001	-0.00001	-0.00004	-0.00004	0.00000
23	Contact resistance	0.00570	0.00570	0.01150	-0.00040	-0.00063	-0.00080	-0.00290	-0.00320	0.00014
24	Thermal conductivity exhaust heat exchanger material	0.00930	0.00930	0.01860	0.00760	0.00580	-0.00340	0.00180	0.00340	0.00061
25	Thermal conductivity coolant heat exchanger material	0.00550	0.00550	0.01090	-0.00160	-0.00170	-0.00044	-0.00370	-0.00430	0.00007

Table 6.10: Sensitivity analysis on the TEG system.

The TEG system model predicts the results from the experiment to a reasonable extent. To use the model for further studies, the deviation of the power generated by the TEG, due to heat lost to the ambient and non-uniform distribution of flow rate has to be fixed. This will also reduce any differences in the temperatures between the model and the experiment. Experiments have to be performed to estimate the pressure drop across the exhaust heat exchanger, so that the reasons for differences between the model and the experiment can be determined. And based on the results from the sensitivity analysis the HZ20 module properties needs to be characterized to gain confidence in the data provided by Hi-Z.

Chapter 7

Conclusions and Future Studies

In this thesis, the exhaust, the coolant, and the TEG subsystem models of the complete AETEG system were developed and have been validated against the results from the experimental testing of the prototype AETEG performed at Delphi.

As discussed in section (4.3) the exhaust system model was in good agreement with the results from the Delphi testing. However, this was achieved only after modifications were made to the internal and external heat transfer coefficients such that the model results fit the experimental data. The differences between the model and the experiment that continue to exist, after the modifications to the heat transfer coefficients, would not make much of a difference in the power generated by the TEG.

From the results shown in section (5.5) the coolant system model predicts the flow rates through various components of the coolant system and through the TEG marginally close to the experimental data from the Delphi testing and the GM coolant system data, except for the radiator flow corresponding to the results from the Delphi testing. The variation of the flow through the radiator is due to the gradual expansion or contraction of the wax element in the thermostat valve. The expansion or contraction of the wax element is due to the rise or fall in temperature of the

engine coolant. The change in engine coolant temperature is governed by the heat transfer from the engine to the coolant, the coolant to the passenger compartment (if the heater is ON), and the coolant to the ambient in the radiator. To be able to estimate the radiator flow precisely, the coolant system model must estimate these heat transfer processes. To develop such models is complex and beyond the scope of this work. However, the use of coolant system model consisting of an incomplete radiator model did not significantly effect the estimation of flow rates through the remaining components of the coolant system.

The TEG system model developed in chapter (6) consisted of determining (1) the power generated by the TEG, (2) exhaust and coolant outlet temperatures, (3) hot and cold side surface temperatures of the thermoelectric modules along the length of the heat exchangers, and (4) the pressure drop across the exhaust and coolant heat exchangers. The difference in (1) the power generated by the TEG, (2) outlet temperatures of the exhaust and the coolant, and (3) surface temperatures of the HZ20 thermoelectric modules between the model and the experimental testing have been attributed to the heat lost to the ambient and the concentration of exhaust mass flow rate towards one half of the exhaust heat exchanger. Further should be done to verify these conclusions.

There is a big difference between the model and the experimental results for the pressure drop across the exhaust heat exchanger. Therefore experiments should be performed to estimate the pressure drop so that the reasons for the difference between the experiment and the model can be determined. The predictions of the model for the pressure drop across the coolant heat exchanger for configurations C and D are reasonable. The differences that are present can be corrected by recalculating the loss coefficients of the coolant heat exchanger, the T-junction, and the elbow.

The three subsystem models can be used reliably to develop a complete AETEG system model. The methodology that will be used in developing the complete AETEG system model will be discussed briefly in the next following section. We should emphasize that the TEG system modeling is the most important component, because the exhaust and the coolant system models developed in the current work are specific to the 1999 GMC Sierra pick-up truck and the application of the TEG is not just limited to this vehicle. The current prototype TEG can be used in many waste heat recovery applications.

7.1 The AETEG System Model and ADVISOR

As discussed previously the AETEG system model can be categorized into (1) the exhaust system model, (2) the coolant system model, (3) the TEG system model, and (4) the vehicle system model. Given the catalytic outlet temperature and exhaust mass flow rate as the inputs, the exhaust system model estimates the inlet temperature into the TEG. Given the engine *rpm* as an input, the coolant system model estimates the coolant flow rate into the TEG. Given the exhaust inlet temperature estimated by the exhaust system model, coolant flow rate into the TEG estimated by the coolant system model, and the exhaust mass flow rate and the coolant inlet temperature estimated by the vehicle system model as the inputs, the TEG system model estimates the power generated by the TEG and other additional variables such as temperatures and pressure drop. The input variables catalytic outlet temperature and exhaust mass flow rate for the exhaust system model and engine *rpm* for the coolant system model are also obtained from the vehicle system model. The data flow across each of these subsystems is shown in figure (7.1).

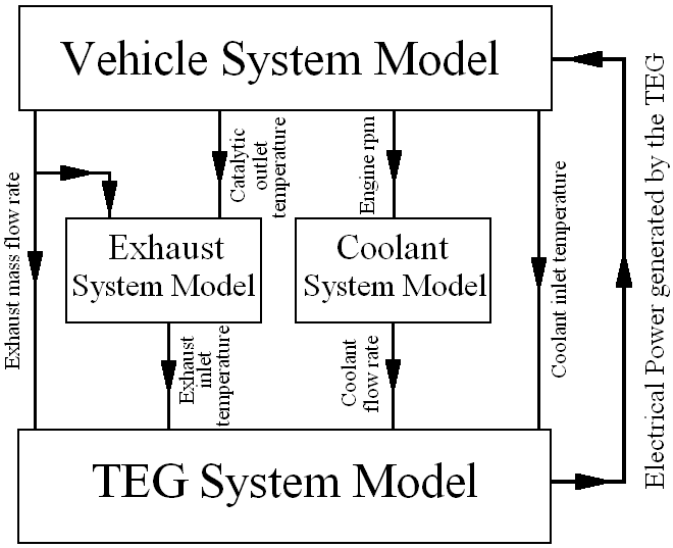

Figure 7.1: Data flow across the AETEG subsystem models.

The subsystem models (1) the exhaust, (2) the coolant, and (3) the TEG will be integrated into the vehicle system model present in the library of a vehicle system analysis tool known as *ADVISOR*.

7.1.1 ADVISOR

"ADVISOR, NRELs *AD*vanced *V*eh*I*cle *S*imulat*OR*, is a set of model, data, and script text files for use with Matlab and Simulink. It is designed for rapid analysis of the performance and fuel economy of conventional, electric, and hybrid vehicles. ADVISOR also provides a backbone for the detailed simulation and analysis of user defined drivetrain components [31]."

Some of the benefits from using ADVISOR can be listed as follows:

- Estimate the fuel economy of vehicles that have not yet been built.
- Learn about how conventional, hybrid, or electric vehicles use (and lose) energy throughout their drivetrains.

- Estimate the change in the fuel economy, tail pipe emissions and performance of the vehicles due to the addition of new subsystems and/or modifications and improvements performed on the existing subsystems. A good example is the use of TEG in an automobile.

7.2 Future Studies

The immediate future studies is to develop a model of the test vehicle: 1999 GMC Sierra used in the Delphi testing. The vehicle library of the *ADVISOR* does not contain a model that matches the performance characteristics of the 1999 GMC Sierra. Therefore changes will be made to the existing conventional sports utility vehicle available in the vehicle library of the *ADVISOR*. Emphasis will be given to develop an engine map based on the data supplied by the GM and from the data of the experimental testing at Delphi, so that at a given engine load and vehicle speed the *ADVISOR* can estimate the (1) fuel usage, (2) catalytic outlet temperature, and (3) exhaust mass flow rate. This is necessary in order to have a complete AETEG system model that can be used reliably for studying various parametric and system optimization studies associated with the use of TEG in an automobile.

Studies will also be performed to evaluate the performance of the use of TEG in a *Series Hybrid Transit Bus* present in the vehicle library of the *ADVISOR*. It was observed that the exhaust mass flow rate from the *Series Hybrid Transit Bus* is almost twice that of a conventional automobile. Therefore we intend to perform the studies by using at least two TEGs that are thermally parallel and electrically in parallel. We also intend to continue with the engine coolant as the heat sink of the TEG.

Performance studies on the use of TEG in a natural gas engine used for the distributed power generation will also be accomplished. The engine we intend to use in this study will be John Deere 8.1 L and 186 kW compressed natural gas spark ignition engine. As this will be a stationary application of the TEG, city water will be adopted as the source for the heat sink in the TEG. The low inlet temperature of the city water, in comparison to the engine coolant, will cause the TEG to produce higher electrical power output.

All of the above studies will be performed using the Hi-Z HZ20 thermoelectric modules. These studies will be repeated by replacing the HZ20 modules with Hi-Zs *quantum well* thermoelectrics. The efficiency of the quantum well thermoelectrics is on the order of 3 to 4 times that of the the material being used in the HZ20 module [32]. Therefore higher power generation by the TEG and greater fuel savings can be anticipated.

Bibliography

[1] Bob Davis and Bhushan Bahree. Over a Barrel. 15 May, 2005 <http://www.wsjclassroomedition.com/archive/03may/ECON_oil.htm>.

[2] 30 Years of Global Warming. 15 May, 2005 <http://www.undoit.org/what_is_gb_30years.cfm>.

[3] Light Truck Average Fuel Economy Standards:Model Years 2005-2007. 15 May, 2005 <http://www.nhtsa.dot.gov/cars/rules/rulings/CAFE05-07/Index.html>

[4] Francis Stabler. Automotive Applications for High Efficiency Thermoelectrics. High Efficiency Thermoelectric Workshop, San Diego, California. March, 2002.

[5] BOSCH Automotive Electrics and Electronics. Robert Bosch GmbH, 1999.

[6] Richard H. Bauer. Auxiliary Electric Power for an Autombile Through the Utilization of a Thermoelctric Generator: A Critical Examination. M of ME Thesis, Department of Mechanical Engineering, Clarkson College of Technology. 1963.

[7] Anthony Joseph Tomarchio. A Feasibility Study of Replacing an Electrical Generator of a Standard American Automobile with a Thermoelectric Generator. M of ME Thesis, Department of Mechanical Engineering, Clarkson College of Technology. 1964.

[8] Ulrich Birkholz, Erwin Groß, Ulrich Stöhrer, and Karsten Voss. Conversion of Waste Exhaust Heat in Automobile Using FeSi2 Thermoelements. Proc. 7th International Conference on Thermoelectric Energy Conversion. Arlington, USA. 1988.

[9] John C. Bass, Norbert B. Elsner, and Ralph Slone. Design Study and Experience with Thermoelectric Generators for Diesel Engines. Proc. Automotive Technology Development Contractors Coordination Meeting. Dearborn, USA. 1990.

[10] J. C. Bass, N. B. Elsner, and F. A. Leavitt. Performance of the 1kW Thermoelectric Generator. Proc. American Institute of Physiscs Conference, 1995.

[11] Ikoma, K., et al. Thermoelectric Module and Generator for Gasoline Engine Vehicle. Proc. 17th International Conference on Thermoelectrics. Nagoya, Japan, 1998.

[12] Douglas Crane, Greg Jackson, and David Holloway. Towards Optimization of Automotive Waste Heat Recovery Using Thermoelectrics. SAE 2001 World Congress, Detroit, MI. March, 2001.

[13] Jorge Vazquez, Miguel A. Sanz-Bobi, Rafael Palacios and Antonio Arenas. State of the Art of Thermoelectric Generators Based on Heat Recovered from the Exhaust Gases of Automobiles. Proceedings of the 7th European Workshop on Thermoelectrics. Pamplona, SPAIN. Oct, 2002.

[14] Robert R. Heikes and Roland W. Ure, Jr. Thermoelectricity: Science and Engineering. Interscience Publishers, 1961.

[15] Stanley W. Angrist. Direct Enrgy Conversion. Allyn and Bacon Inc., 1971.

[16] HZ20 Thermoelectric Module. 15 May 2005 <http://www.hi-z.com/websit04.htm>.

[17] G. S. Nolas, J. Sharp, and H. J. Goldsmid. Thermoelectrics Basic Principles and New Materials Developments. Springer, 2001.

[18] J. Vazquez, M. A. Sanz-Bobi, R. Palacios, and A. Arenas. State of the Art Thermoelectric Generators Based on Heat Recovered from the Exhaust Gases of Automobiles. Proceedings of the 7th European Workshhop on Thermoelectrics, Paper:17. Pamplona, Spain. October, 2002.

[19] Francis Stabler. General Motors Corporation, personal communication, 2001.

[20] E. F. Thacher. AETEG Prototype: System Test Report, July, 2005.

[21] Frank P. Incropera and David P. DeWitt. Introduction to Heat Transfer, John Wiley & Sons, 2002.

[22] C. A. Mesa. The Engine Cooling System, Technology Transfer Systems, Inc., 2003.

[23] C. J. Richter. Delphi Corporation. Personal communication, January, 2004.

[24] Alexander J. Smits. A Physical Introduction to Fluid Mechanics. John Wiley & Sons, Inc. 2000.

[25] E. F. Thacher. Thermoelectric Power from Vehicle Exhaust: Phase 2A, Progress Report 9, Reporting Period: 12/16/03- 1/15/04.

[26] I. E. Idelchik. Handbook of Hydraulic Resistance. Hemisphere Publishing Corporation, 1986.

[27] Frank M. White. Fluid Mechanics. McGraw-Hill, 2003.

[28] 1999 GMC Sierra Coolant System Data, General Motors, 2002.

[29] Raj M. Manglik and Arthur E. Bergles. Heat Transfer and Pressure Drop Correlations for the Rectangular Offset Strip Fin Compact Heat Exchanger Experimental Thermal and Fluid Science., 10:171-180, 1995.

[30] James P. Hartnett and Milivoje Kostic. Heat Transfer in Rectangular Ducts, Adv. Heat Transfer 19, 338, Academic Press, Inc., 1989.

[31] Aaron Brooker, et al. ADVISOR Documentation. National Renewable Energy Laboratory. 2002.

[32] Aleksandr S. Kushch, John C. Bass, Saeid Ghamaty and Norbert B.Elsner. Thermoelectric Development at Hi-Z Technology. 7th Diesel Engine Emissions Reduction Workshop. August, 2001.